UNIVERSITY OF BIRMINGHAM

HOLOGRAPHIC LASER ABLATION FOR NANOPATTERNING

By

Bader Ahmad AlQattan

A thesis submitted to
The University of Birmingham
for the degree of

DOCTOR OF PHILOSOPHY

School of Engineering
Department of Mechanical Engineering
The University of Birmingham
January- 2019

Abstract

Current lithography methods to produce nanophotonic devices for optical applications are costly and time consuming. Holographic direct laser interference patterning has helped to establish a strategy to rapidly create 1/2D nanopatterns from a variety of materials. A 640 nm × 640 nm pattern structure of Au-Ti was accomplished by controlling the distances between the laser source, the recording medium, and the object. This metal structure has a limitation in regard to thickness to develop better and efficient light diffraction intensity. Later, the Denisyuk reflection mode method was used on the films (about 1 μm) of four ink-based dye colours (black, red, blue, and brown) to fabricate low-cost and efficient nanopatterns. The dyes have the same structural nano spacing (840 nm), but they produced different diffraction in response to monochromatic and broadband light. The recording mediums have different light absorption ranges and the black has the highest absorption. After that, we focused on contact lenses which are universal low-cost biomedical devices with possible applications as quantitative analytical devices for point-of-care diagnostics. Incorporating nanoscale features into commercial contact lenses as low-cost biosensors is considered a challenge. As the black dye has a high optical absorption, it was deposited over a contact lens to produce optical nanostructures on the surface, via holographic laser ablation for sensing ocular diseases. The holographic nanostructures showed a great response to sensing a change of Na^+ ions (±47 mmol L^{-1}) in a human tear, to diagnose the severity of a dry eye condition at the early stages. Likewise, this advantage of the black dye's absorption can be used to produce economical optical strain sensors for civil engineering, aerospace and human interface applications. A holographic interference patterning mode was used to produce nanostructures on a commercial adhesive tape to fabricate a surface compatible, lightweight and cost effective strain sensor for rapid response to cracks, deflections or tears of 5 με.

Acknowledgements

I would like to express my sincere gratitude to my research supervisor, **Dr Haider Butt** for his generous guidance, constant feedback and support during my PhD study. Without his generous constructive advice and valuable efforts, this research and the resulting thesis could not possibly have been produced. He has certainly influenced my future career and life.

I would also like to thank our collaborator **Dr Ali K Yetisen** for his support. I am very grateful for his generous feedback during my PhD study. A very special thank you to **Dr Aydin Sabouri** for his great guidance and help in my first steps of my PhD.

I am especially grateful to **Dr Muhammad Umair Hassan** for his invaluable advice. I would also like to thank our collaborator, **Dr David Benton** for his precise advice and significant insight.

Very special thanks go to my colleague Magdalena Bajgrowicz-Cieslak for her contribution towards improving my project. I also would like to thank my colleagues and my friends, Dr Sunan Deng, Mohamed Elsherif, Ijaz Rashid, Tawfiq Alqurashi, Yousef Alqurashi, Muhammad Waqas Khalid, and Rajib Ahmed.

This thesis was partly proofread for conventions of language, spelling and grammar by Janet's Proofreading Service.

Most of all, I would like to thank my family, my wife, my kids and my brother Abdullah for their support throughout my graduate study journey.

Table of Contents

Abstract ii
Table of Contents iv
List of Figures viii
List of Tables xiii
Abbreviations xiv
Nomenclature xvi
List of Equations xix
List of Publications xxi
1.1-Introduction 1
1.2-Aim and objectives 3
1.2.1-Aim 3
1.2.2-Objectives 3
1.3-Thesis structure 5
Chapter 2: LITERATURE REVIEW 7
2.1-Introduction 7
2.2-Photonic applications 7
2.2.1-Grating history 8
2.2.2-Varied line space (VLS) 9
2.2.3-Modern lithography 9
2.2.3.1-Nano-printing through optical lithography 9
2.2.3.2-Moulding with UV-curing nano-imprint lithography 10
2.2.3.3-Stamping hot embossing nano-imprint 10
2.2.3.4-Electron/ion beam lithography 11
2.2.3.5-Direct writing by nano/femtosecond laser 12
2.2.3.6-Laser nano- patterning 12
2.2.3.7-Single-beam interference 13
2.2.3.8-Lithography systems' comparison 14
2.3.1-Electromagnetic waves and holographic DLIP 15
2.3.2-Laser interference 16
2.3.3-Light propagation 18
2.3.4-The law of transmission, reflection and refraction 18

2.3.5-Refraction through an aspherical surface 19
2.3.6-Light and diffraction grating 19
2.3.7-Light dispersion grating 21
2.4-Colour material and film efficiency 21
2.4.1-Colour material 21
2.4.2-Material efficiency 23
2.5-Biosensor contact lenses 24
2.5.1-Selecting contact lens 25
2.5.2-Nanostructure on contact lens and hydrophobicity measurement 26
2.6-Nanostructure for sensing and imaging 27
2.6.1-Strain sensors 27
2.6.2-Fresnel zone plate lens and distorting patterning fabrication methods 29
2.6.3-Quadruple wave 29
Chapter 3: HOLOGRAPHIC DIRECT PULSED LASER WRITING OF TWO-DIMENSIONAL NANOSTRUCTURES 31
3.1-Abstract 32
3.2-Introduction 32
3.3-The mechanism of surface grating 33
3.4-Results and discuss 34
3.4.1-Fabrication technique 34
3.4.2-Computational modelling of the focused beam interference 37
3.4.3-Diffraction grating and 2D patterns fabrication 38
3.4.4-Optical characterization of the gratings 41
3.5-Conclusion 46
Chapter 4: LASER NANOPATTERNING OF COLORED INK THIN FILMS FOR PHOTONIC DEVICES 47
4.1-Abstract 48
4.2-Introduction 48
4.3-Materials and methods 50
4.3.1-Preparation of the ink recording media 50
4.3.2-Fabrication of the diffraction gratings in ink 51
4.3.3-Spectroscopic measurements of the ink gratings 51
4.3.4-Angle-resolved measurements of the gratings 51
4.4-Results and discussion 52
4.4.1-Holographic fabrication of 1D nanostructures 52

4.4.2-Optical characterization of the gratings 56
4.4.3-Spectrum rainbow diffraction measurement 62
4.5-Applications of the ink-based gratings 65
4.6-Conclusions 67
Chapter 5: DIRECT LASER WRITING OF NANOPHOTONIC STRUCTURES ON CONTACT LENSES 68
5.2-Introduction 69
5.3-Materials and methods 71
5.3.1-Preparation of the recording media on contact lenses 71
5.3.2-Fabrication of diffraction gratings on contact lenses 72
5.3.3-Spectroscopic measurements of the ink gratings 73
5.3.4-Angle-resolved measurements of the gratings 73
5.4-Results and discussion 73
5.4.1-Holographic fabrication of nanostructures on contact lenses 73
5.4.2-SEM structure images, light transmission and polarization on contact lenses 77
5.4.3-Fabrication of 2D nanostructures on contact lenses 82
5.4.4-Spectrum rainbow diffraction measurement 83
5.5-Fabrication of different nanostructures on contact lenses 86
5.6-Nanostructures on contact lenses for optical sensing 88
5.8-Conclusions 91
Chapter 6: CURVE PHOTONIC STRUCTURES FOR SENSNIG 93
6.1-Abstract 94
6.2-Introduction 94
6.3-Materials and methods 96
6.3.1-Preparation of the recording media of the sensing tape 96
6.3.2-Fabrication of diffraction gratings on glass on adhesive tape 97
6.3.3-Spectroscopic measurements of the ink gratings 97
6.3.4-Angle-resolved measurements of the gratings 98
6.4-Results and discussion 98
6.4.1-Holographic fabrication of Fresnel zone plate and distorted nanostructures 98
6.4.2-Optical characterization of the structure 103
6.4.3- Focusing analysis 107
6.4.4-Spectrum rainbow diffraction measurement 109
6.5- Applications of the curved nanopatterning structure 112

6.5.1- 1D/2D curved nanopatterning structure 112
6.5.2- Elongation sensing, imaging and holographic logo 115
6.5.3-Imaging and holographic logo 115
6.6-Conclusion 118
Chapter 7: SUMMARY AND FUTURE WORK 119
7.1-Introduction 119
7.2-Summary 120
7.3-Future work 124
References: 126
Appendix 136
2S- Literature review 136
3S-HOLOGRAPHIC DIRECT PULSED LASER WRITING OF TWO 138
DIMENSIONAL NANOSTRUCTURES 138
Repeatability 140
4S-LASER NANOPATTERNING OF COLOURDED INK THIN FILMS FOR 141
PHOTONIC DEVICES 141
5S-DIRECT LASER WRITING OF NANOPHOTONIC STRUCTURES ON CONTACT LNESES 143
6S- CURVE PHOTONIC STRUCTURES FOR SENSENIG 145

List of Figures

Figure 2.1: Electric and magnetic waves' relation 16
Figure 2.2: Laser light interference in DLIP Denisyuk reflection mode 17
Figure 2.3: Reflection and transmission through different mediums 19
Figure 2.4: Holographic grating on diffracted incident light of a grating structure by (a) reflection, (b) transmission 20
Figure 2.5: The thickness of sinusoidal grating structure influences the diffracted order 23
Figure 3.1: Fabrication of 1/2D patterns through nanosecond laser light interference in holographic DLIP Denisyuk reflection mode. (a) Nd:YAG laser beam (3.5 ns) propagates through a converging lens and reflected back from a plane mirror to ablate the localized regions of the recording medium (metal film). 36
Figure 3.2: FEM modelling of the focused beam interference(a) Computational geometry for the focused laser beam interference and its 2D intensity distribution. (b) Normalized intensity profile plotted for the focused laser light interference at planes of 30° and 45°, respectively. (c-d) Focused beam interference spacing as a function of distance between mirror and the observation plane (*d*) and tilt angle (θ). Inset shows normalized intensity profiles as a function of arc lengths. (e) Grating spacing as a function of wavelength. 38
Figure 3.3: Microscopy images of the Au-Ti surface gratings fabricated by holographic DLIP. (a) Grating with periodicities of 7.7 μm, (b) 3.28 μm, and (c) 960 nm. The effect of changing (d) tilted and modelling angles, (e) mirror-sample distance, and (f) laser beam-sample distance on grating periodicity. (g) The effect of changing energy on grating bar width. Microscopy images of 25nm Au sample produced with (h) energy of 90mJ and periodicity of 1.4μm and with (i) energy of 330mJ and periodicity of 1.3 μm. (j) The effect of altering number of pulses on grating periodicity. Optical microscopy images of grating made with 330mJ energy at (k) 3 and (l) 4 Hz. (scale bar = 5 μm) 40
Figure 3.4: 2D Au square arrays fabricated by holographic DLIP.Arrays of 25 nm thick (a) squares (640 nm × 640 nm) and (b) parallelograms (2.4 μm × 1.8 μm). Arrays of 40 nm thick (c) elongated squares (2.98 μm × 3.04 μm) and (d) parallelograms (5.8 μm × 950 nm). (scale bar = 10 μm) 41
Figure 3.5: Diffraction of monochromatic light λ = 650 nm from 2D nanopattern arrays. Light diffraction from (a) squares (640 nm × 640 nm), (b) rectangles (2.4 μm × 1.8 μm) (c) rectangles (parallelograms) (5.8 μm × 950 nm)), and (d) squares (2.98 μm × 3.04 μm),. Angle-resolved measurements of diffraction intensity for the diffraction patterns shown in (a-d) respectively. (scale bar = 10 μm) 42
Figure 3.6: Angle-resolved measurements of the diffraction pettering fabricated *via* holographic DLIP. (a) The spectroscopy system contains a white light beam that passes through a 2D metal film sample on a motorized stage. (b) Transmission spectra of 25 nm thick elongated-rectangular array (2.4 μm × 1.8 μm) x axis and (c) y axis. Transmission spectra of square array (640 nm × 640 nm) (d) x axis and (e) y axis. 45
Figure 4.1: Fabrication of 1D patterns through nanosecond DLIP in holographic Denisyuk reflection mode.(a) Nd:YAG laser beam (532 nm, 3.5 ns) was directed to a dielectric mirror and passed through a dye-based ink medium and reflected back from a plane mirror to ablate a localized region of the recording medium. Four dye-based ink mediums are (b) black, (c) red, (d) blue, and (e) brown. The light transmission measurement for each medium added on each colour. (scale bar = 200 μm) 52
Figure 4.2: Optical microscopy images of 1D surface grating nanostructures fabricated on 915 nm thickness dyes by holographic DLIP. Gratings having periodicities of 840 nm in (a) black, (b) red, (c)

blue, and (d) brown inks. The light transmission graphs of each ink were integrated for normalization. (scale bar = 10 μm.) 55
Figure 4.3:SEM grating image of (a) black, (b) blue gratings. The light transmission graphs of each ink were integrated for normalization. (SEM scale bar=1 μm) 56
Figure 4.4: Diffraction from nanostructures upon illumination from three onochromatic light sources (405 nm, 532 nm and 635 nm) on patterned ink gratings (Λ = 840 nm) (a-c) Black, (d-f) red, (g-i) blue, and (j-l) brown inks.(scale bar=5 cm) 58
Figure 4.5: Diffraction intensity of the zero and first order from three monochromatic lights (405 nm, 532 nm and 635 nm) on four patterned ink gratings: (a) black; (b) red; (c) blue; (d) brown ink gratings; black ink gratings at different thicknesses in (e) transmission; (f) diffraction modes spin-coating effect; (g) thickness; (h) light absorption. 61
Figure 4.6: Angle-resolved measurements of the diffraction gratings fabricated *via* holographic DLIP. (a) The spectroscopy system contained the diffraction of a broadband light beam that passed through a 1D ink sample on a motorized stage to measure the rainbow pattern. The rainbow grating diffraction pattern of (b) black, (c) red, (d) blue, and (e) brown inks. Rainbow pattern length from the grating diffraction of (f) black, (g) red, (h) blue, and (i) brown light diffraction. Spectroscopy measurements of (j) black, (k) red, (l) blue, and (m) brown dye-based inks. (scale bare =5 cm) 64
Figure 4.7: Hydrophobic properties and applications of dye-based ink gratings. (a1) black, (a2) red, (a3) blue, and (a4) brown ink wavelength filters. (b) Hydrophobicity measurements on the dye-based inks. (c) The nanopatterned gratings in array form. (d-e) hydrophobicity contact angle change. (f1-f2) Blue ink based 1D grating personal security signature. (g1-g2) Black ink-based surface grating University of Birmingham logo. (scale bar=5 mm) 66
Figure 5.1: Fabrication of 1D nanopatterns on a contact lens through nanosecond DLIP in holographic Denisyuk reflection mode. (a) Nd:YAG laser beam (1064 nm, 3.5 ns) was guided by a mirror and passed through a dyed contact lens and reflected back from a plane mirror to ablate localized regions in the recording medium. (b) Fabricated ink-based holographic nanostructures on contact lenses (scale bar=5 mm). Schematics of (c) 1D and (d) 2D nanostructures. (e) Optical microscopy image of 1D nanostructure surface. The inset shows the SEM image of the surface topography (scale bar=5 μm). (f) Contact lens geometry and thickness distribution. (g) An optical image of a contact lens cross section in ambient humidity conditions (scale bar=100 μm). (h) Contact lens thickness change in ambient humidity, fully-hydrated condition in DI water, and hydrated condition in artificial tear. 75
Figure 5.2: Electron microscopy and spectroscopy analyses of the nanopatterned (a-c) SEM images of 1D nanostructures on the contact lens with increasing magnification (scale bar=5 μm). Scale bar for (c) is 2 μm. The optical transmission spectra for commercial contact lens in three conditions: (d) plain lens, (e) black dye coated the lens, (f) and nanopatterned lens at different moisture conditions. Effect of incident light polarization on transmission in (g) fully-hydrated plain lens, (h) dyed lens in ambient humidity, and (i) nanopatterned lens in ambient humidity. 78
Figure 5.3: 1D surface grating nanostructures fabricated by holographic DLIP.Simulation and experimental diffraction results for gratings with a periodicity of Λ=925 nm on the contact lens surfaces in ambient humidity, fully-hydrated and artificial tear conditions. (a1) Simulated and (a2) experimental diffraction results for 450 nm wavelength at different humidity conditions. (b1) Simulated and (b2) experimental diffraction changes at 532 nm. (c1) Simulated and (c2) experimental diffraction for 635 nm. Scale bar=5 cm. 80
Figure 5.4: Optical characterization of 2D surface grating nanostructures (925 nm × 925 nm) fabricated by holographic DLIP on the contact lens. (a) An optical microscopy image of the 2D grating. (b) Angle-resolve measurements of diffraction readouts in transmission mode upon illumination with three monochromatic beams: (c-d) 450 nm, (e-f) 532 nm, and (g-h) 635 nm. (scale bar=5 cm) 84

Figure 5.5: Angle-resolve measurements of the 1D and 2D diffraction patterns from the contact lens. (a) The spectroscopic measurement of the rainbow diffraction of 1D nanostructure over the contact lens in transmission mode using a broadband light. Scale bar=5 mm. (b) Broadband white light angular measurements for 1D and 2D gratings along the x-axis. Scale bar=5 mm. (c) Holographic contact lens on an eye model. (d) 2D rainbow diffraction of the holographic contact lens on spherical screen. (scale bar=1 cm) 85
Figure 5.6: Optical microscopy images of 2D nanostructures with different geometries on contact lenses. (a1) 1.3 μm × 1.3 μm, (2a) 1.7 μm × 1.5 μm, (a3) 0.9 μm × 2.4 μm, and (a4) 0.9 μm × 2.7 μm. Scale bars = 5 μm. (b1-4) Diffraction of monochromatic light (450 nm) *via* 2D patterned arrays. Scale bar=1.0 cm. (c1-4) Rainbow diffraction from 2D patterned arrays, scale bar=1.0 cm. (d1-4) Contact angle measurements of 2D nanostructures on contact lenses. (scale bars = 1.0 mm) 88
Figure 5.7: Light transmission spectra as a function of Na^+ ion concentrations(a) Dye coated lens and (b) nanograting on contact lens. (c1-c4) Ellipsometry, refractive index, and grating diffractive angle measurements of Na^+ ion concentrations (Table S5.3). (d) Diffraction measurements on the nanopatterned contact lens at different Na^+ ion concentrations. Scale bar=5 cm. (e-h) Different designs (rings/patches) of holographic nanostructures fabricated on contact lenses. Each image demonstrates the diffraction colours observed at various angles. (scale bar=5 mm) 90

Figure 6.1: Fabrication of Fresnel lens and distorted nonpatterns of nanosecond DLIP in holographic Denisyuk reflection mode: (a) Nd:YAG laser beam (1064 nm, 3.5 ns) was guided by a dielectric mirror and passed to a set of mirrors through black dye on a glass slide reflected back from (b1), the centre of the concave mirror (centre pulse (Cp)); (b2) Fresnel zone plate representation; (b3) optical image of the fabricated Fresnel lens plate. The second set of mirrors: (c1) exposure from the side of the concave mirror (side pulse (Sp)); (c2) displacement structure representation; and (c3) optical displacement structure. (scale bar = 100 μm) 100
Figure 6.2: Optical microscopy images showing surface grating nanostructures fabricated by holographic DLIP reflection from the centre and the side of a concave mirror. The effect of changing the laser amplitude due to the reflection and samples' tilted angle on the structures' spacing (the smallest regen R1 - the largest regen R2 periodicities): (c1) 00 (0 μm-12.1 μm); (s1) 00 (5.6 μm-9 μm); (c2) 50 (4.9 μm-7.1μm); (s2) 50 (3.39 μm-3.44 μm); (c3) 250 (1.16 μm-1.23 μm); (s3) 250 (1.12 μm-1.17 μm). Tilted angle effect on structures' spacing of (d4) Cp, Sp and theoretical; (c4) transmission on Cp structures ;(s4) transmission on Sp structure; scale bar = 5 μm. 103
Figure 6.3: Experimental diffraction from nanostructures of varying periodicities produced at tilted angle of $50 - 350$, via central pulse (c1); and side pulse (s1). Diffraction from 00 samples with (c2) symmetric Fzp circles and (s2) asymmetric curve structures. Red laser illumination on a 50 (c3) centre structure; (s3) side structure. Diffraction results for 450 nm, 532nm, and 635 nm wavelengths with 250 tilt angle sample (c4) centre pulse; (s4) side pulse; scale bar = 5 cm. 105
Figure 6.4: Changing distance of the measured diffraction patterns from 250tilted angle samples (a-b) central pulse structure and side pulse structure; (c) two pulse structure comparison. Changing screen distance for a centre pulse 50 sample ; (d) image of diffraction at different distances. Red laser illumination for 50 tilted angle sample (e) graph for changing distance and resultant diffraction intensity; (f) left side of diffraction points; and (g) right side diffraction points; scale bar = 5 cm. 108
Figure 6.5: Angle-resolved measurements of fabricated patterning structure by holographic DLIP: (a) the spectroscopy system to analyse a white light diffracted beam through a sample on a motorized stage to measure the rainbow pattern. The rainbow structure diffraction pattern for (b) centre pulse samples

produced at 0° to 35°; (c) side pulse samples at 0° to 35°. Lift and right rainbow diffraction of 25° structure: (d) centre pulse patterning, and (e) side pulse patterning; scale bar = 1 cm. 111
Figure 6.6: Holographic 1D (0.9 μm) nanopatterning structure via measurements diffractive angle of pH concentrations (a)5.0, (b)5.5, (c)6.0, (d) 6.9, (e) 7.4, (f)7.8, (g)8.2.(scale bar=5 cm) 113
Figure 6.7: Fabrication of 1D and 2D curved nanopatterns using holographic DLIP. The larger and smaller structure periodicity were (a) 1D (0.88 μm-0.90 μm); (b) 2D (0.90 μm-0.88 μm x 0.88 μm x 0.9 μm); (c) transmission analysis; scale bar = 5μm. Contact angle measurements of (d) plain tape; (e) 1D structure; (f) 2D structure; scale bar = 1 mm; laser illumination of (g) 450 nm; (h) 532 nm; (i) 635 nm). Rainbow diffraction of (j) 2D pattern sample; visible colour analysis of (k) a 1D pattern sample using room light. (scale bar = 1 cm) 114
Figure 6.8: Curved nanostructure on a tape for elongation measurement and applications (a) stretching set-up; mechanical measurements of tape, (b) elastic and plastic deformation, (c) Young's modulus; curved nanopatterning on tape, (d) stretching diffraction measurement; imaging by white source nanostructure, (e) Fresnel lens, (f) grating displacement, (g) centre pulse at 50; imaging with monochromatic light through 50centre pulse structure:(h) 450nm, (i) 532nm, (j) 635nm); holographic curved nano surface grating of (k-m) BHAM logo; scale bar = 1 cm. 117

Figure 7.1: Fabricated 1D surface grating nanostructures on contact lens by holographic DLIP to measure curvature change. Red laser illumination (a) curve change; (b) diffraction angle; scale bar = 5cm..... 125
Figure 7.2: Holographic nanostructure on rice sheet. (scale bar = 5μm)..... 125

Figure 2S.1: Example of direct laser interference patterning by two laser beams (a) schematic diagram of interference principle, (b) experimental set up. 136
Figure 2S.2: Two harmonic Electric waves move in parallel to form superposition waves. 136
Figure 2S.3:Two harmonic Electric waves move in opposite each other to form superposition waves. 137
Figure 3S.4: Laser spot size as a function of (h) distance variations. Inset size (diameters): s1 = 7.3 mm, s2 = 7.6 mm, s3 = 8.2 mm, and s4 = 9.1 mm. 138
Figure 3S.5: Microscopy images of the Au 25nm thickness surface gratings fabricated by holographic DLIP. (a, b, d) Examples of changing the laser energy on the Au film. (c) The plot for the change of energy effect in the Au film. The graph shows that the effect of laser energy after 330mJ on Au film which increase the removal rate and affect the material quality.(scale bar =5 μm)..... 138
Figure 3S.6:Microscopy images of 2D arrays with different thicknesses fabricated by holographic DLIP. (a) Arrays of 25 nm thick rectangle (0.969 μm ×4.76 μm) and (b) Arrays of 40 nm thick square (1.14μm × 1.14 μm), (c) Arrays of Au 25 nm thick squares (1.36 μm × 1.36μm) and (d) Arrays of 5 nm thick square (1.58 μm × 1.528 nm). (scale bar = 10 μm)..... 139
Figure 3S.7:SEM images for 25 nm thick Au surface grating with spacing of (a) 2.4 μm × 1.8 μm and (b) 2.4 μm. Alicona images for (c) 2.4 μm × 1.8 μm and (d) 1.8 μm periodic sample. The scale bars are (a)8μm, (b) 5μm, and (c-d) 12 μm, respectively. 139
Figure 3S.8:Microscopy images of (a-b) 19 nm Au surface gratings fabricated by holographic DLIP with energy of 150 mJ. (c-d) 25 nm Au surface grating with energy of 330 mJ with spacing of 1.37 μm. (scale bar =5 μm) 140

Figure 4S.9:Nanostructure diffraction from three monochromatic lights of (405 nm, 532 nm and 635 nm) on black ink grating (0.84 nm) (a-c) Nd:YAG laser beam wavelength 532 nm (d-f) Nd:YAG laser beam wavelength 1064 nm. 141
Figure 4S.10:Angle-resolved measurements of the diffraction gratings fabricated *via* holographic DLIP for the first order of the black dye-based inks. 142
Figure 4S.11:Transmission through 0-order (a) glass, (b) black ink, (c) red ink, (d) blue ink and (e) brown dye-based inks. 142
Figure 5S.12: Black ink gratings at different thicknesses in (a) transmission, (b) diffraction modes. 143
Figure 6S.13: Optical microscopy images showed surface grating nanostructures fabricated by holographic DLIP reflection from the centre of concave mirror. The of changing the laser amplitude due reflection and samples tilted angle on structures spacing (c1) 00 , (c2) 50, (c3) 100 ,(c4) 150 , (c5) 200, (c6) 250 , (c7) 300, (c8) 350 . (scale bar = 5 μm)..... 145
Figure 6S.14: Optical microscopy images showed surface grating nanostructures fabricated by holographic DLIP reflection from the side of concave mirror. The of changing the laser amplitude due reflection and samples tilted angle on structures spacing (s1) 00 , (s2) 50, (s3) 100 ,(s4) 150 , (s5) 200, (s6) 250 , (s7) 300, (s8) 350 . (scale bar = 5 μm)..... 145
Figure 6S.15: Experimental diffraction at central pulse on concave mirror with samples tilted angle of (c1) 50 − 350 (c2) Fresnel lens at 00, (c3) 50, (c4) 100 ,(c5) 150 , (c6) 200, (c7) 250 , (c8) 300, (c9) 350 .(scale bar=5 cm)..... 146
Figure 6S.16: Experimental diffraction off side pulse on concave mirror with samples tilted angle of (s1), 50 − 350 (s2) Grating displacement lens at 00, (s3) 50, (s4) 100 ,(s5) 150 , (6s) 200, (s7) 250 , (s8) 300, (s9) 350 .(scale bar=5 cm)..... 146
Figure 6S.17: 2D patterning structures produced by holographic DLIP reflection on the side of concave mirror and they are generated by three pulses. Optical microscopy images of 2D nanostructures with different geometries and the 635nm illumination diffraction (a1) 1.7 μm × 1.7 μm, , (1b) 1.2μm × 1.2 μm, , (c1) 1.84μm × 4.5 μm.(a2-c2) Diffraction of monochromatic light (635 nm) *via* 2D patterned arrays. (scale bar = 5 μm)..... 147

List of Tables

Table 2.1: Comparison among lithography techniques' equipment 14
Table 2.2: Grating efficiency range 24
Table 2.3: Contact lens roughness and water content comparison [100]. 26
Table 2.4: Contact angle range 27
Table 4.1: Diffraction from ink based gratings using three laser beams (405 nm, 532 nm, 635 nm) and comparison with the theoretical values. C: Colour, L: Laser, Exp S: Experimental secondary laser, Exp P: Experimental primary laser, Ther.: Theoretical values calculated with Eq. 4.6. 59
Table 5.1: Diffraction from contact lens gratings using three laser beams (450 nm, 532 nm, 635 nm) and comparison to the theoretical values. Exp: Experimental diffraction angle, Theo: Theoretical diffraction angle values. amb-hum:ambient humidity, full-hyd:fully-hydrated, and hyd-tear: hydrated with tear. 81
Table 6.1: Periodicity measurement black dyes based on the changing exposure angle; C: pulse on the centre; S: side pulse; R1: smallest regen grating; R2: largest regen grating; Theo: theoretical spacing. 102
Table 6.2: Diffraction angle measurement on glass black dyes, based on the changing angle of beam exposure $(50 - 350)$ of the samples, and comparison between experimental and theoretical results at centre pulses and side pulses. 106
Table S5.1: Properties of the contact lenses. 144
Table S5.2:Dissolved NaCl in DI water at different concentrations and ellipsometry equivalent reading of refractive index values. 144

Abbreviations

BPLC	Blue phase liquid crystal
Cp	Centre pulse
1D	One dimension
2D	Two dimensions
3D	Three dimensions
DI	Deionized water
DLIP	Direct laser interference patterning
EBL	Electron beam lithography
FEM	Finite element method
FIB	Focused ion beam
Fzp	Fresnel zone plate
Gd	Grating displacement
GTD	Geometrical theory for diffraction
NP	Nanoparticles
RGB	Red, green, blue

SEM	Scanning electronic microscope
SNP	Silver nanoplate
Sp	Side pulse
UV	Ultra violet

Nomenclature

A	Axis plane
c	Speed light
E	Electric field
E_x	Electric field at x-axis
E_y	Electric field at y-axis
E_z	Electric field at z-axis
E_I	Incident laser wave
E_R	Reflection laser wave
f	Reflection focal point
f_o	Designation focal point
f_z	Fresnel lens focal point
f_{img}	Imaging focal point
f_{lens}	Lens focal point
H	Magnetic field
H_x	Magnetic field at x-axis
H_y	Magnetic field at y-axis
H_z	Magnetic field at z-axis
h	Height
h_c	Grating thickness
I	Intensity
I_o	Maximum intensity
I_0	Intensity of zero order

I_1	Intensity of first order
I_{eff}	Intensity efficiency
k	Propagation number
K	Magnitude of grating vector
k_0	Wave vectors of vacuum
k_1	Wave vectors of the phase constant substrate
n_o	refractive index
n_i	Incident medium refractive index
n_t	Transmission medium refractive index
m	Diffraction order
$m_{ambient}$	Lens mass in ambient humidity
$m_{hydrated}$	Lens mass in fully-hydrated condition
Q′	Absorption parameter
q_w	Mass of fully-hydrated condition
r	Radius of structure
r_c	Rradius of the concave mirror
r_i	Internal radius
r_o	External radius
t	Time (period)
v_i	Incident velocity
v_t	Transmission velocity
W	Diffracting defocused power
x	Node point
Y	Total waves of laser interference

Y_I	Incident laser wave (reference)
Y_R	Reflected laser wave (object)
z	Periodic function
z_{max}	Maximum depth
α	Diffraction angle
μ	Modulation efficiency
Θ	Exposure angle
θ_i	Incident angle
θ_t	Transmission angle
Λ	Grating spacing
δ	Phase difference represented
λ	Wavelength
ε	Wave phase
Φ	Arbitrary phase constant
v	Frequency
ω	Angular velocity

List of Equations

$n_o = \frac{C_{vacuum}}{C_{material}}$ *(Eq. 2.1)*

$E = E_I + E_R$ *(Eq. 2.2)*

$\frac{\sin\theta_i}{\sin\theta_t} = \frac{v_i}{v_t}$ *(Eq. 2.3)*

$n_i \sin\theta_i = n_t \sin\theta_t$ *(Eq. 2.4)*

$\mu = h/\Lambda$ *(Eq. 2.5)*

$\frac{1}{f} = [1-n](\frac{1}{r_i} - \frac{1}{r_o} + \frac{(1-n)d}{r_i r_o n})$ *(Eq. 3.1)*

$E_x = -2A_x [sin(\frac{\omega z}{v_1})] e^{-i(\omega t - \frac{\pi}{2})}$ *(Eq. 3.2)*

$E_y = -2A_y [sin(\frac{\omega z}{v_1})] e^{-i(\omega t - \frac{\pi}{2})}$ *(Eq. 3.3)*

$E_z = H_z = 0$ *(Eq. 3.4)*

$H_x = -2A_y\ n_1 [\ cos(\frac{\omega z}{v_1})] e^{-i(\omega t)}$ *(Eq. 3.5)*

$H_y = 2A_x\ n_1 [\ cos(\frac{\omega z}{v_1})] e^{-i(\omega t)}$ *(Eq. 3.6)*

$E_I = E_{01}\ sin(kx + \omega t + \varepsilon_I)$ *(Eq. 4.1)*

$E_R = E_{0R}\ sin(kx + \omega t + \varepsilon_R)$ *(Eq. 4.2)*

$E = E_I + E_R$ *(Eq. 4.3)*

$I = I_o \cos(\frac{2\pi\Lambda}{\lambda})$ *(Eq. 4.4)*

$\Lambda = \frac{\lambda}{2sin(\Theta)}$ *(Eq. 4.5)*

$\Lambda = \frac{\lambda m}{sin(\alpha)}$ *(Eq. 4.6)*

$Q' = 2\pi\lambda h_c / n_o \Lambda^2 \cos\Theta$ *(Eq. 4.7)*

$m = 2\pi n_o\ \Lambda \sin\Theta/\lambda$ *(Eq. 4.8)*

$h_c = \lambda / 2n_o$ *(Eq. 4.9)*

$q_w = \left(\frac{m_{ambient}}{m_{hydrated}} \right) \times 100\ (\%)$ *(Eq. 5.1)*

$Y_I = A\cos 2\pi\left(vt + \frac{x}{\lambda}\right)$ *(Eq. 5.2)*

$Y_R = A\cos 2\pi\left(vt - \frac{x}{\lambda}\right)$ *(Eq. 5.3)*

$Y = Y_I + Y_R = \left|2A\cos 2\pi\frac{x}{y}\right| \cos 2\ vt$ *(Eq. 5.4)*

$\Theta(x, y) = z(x, y)k_{1+}(z_{max}\text{-}z\ (x,y)\ )k_0$ *(Eq. 5.5)*

$\Theta(x, y) = z(x, y)(k_1 - k_0) + \Phi$ *(Eq. 5.6)*

$I(x, y) = I_0(x,y)\ e^{\,i\Theta(x,y)}$ *(Eq. 5.7)*

$m = 2\pi n_o\ \Lambda \sin\Theta / \lambda$ *(Eq. 5.8)*

$f_c = \frac{1}{2} r_c$ *(Eq. 6.1)*

$E_I = E_I\ \sin(\omega t + \alpha_I)$ *(Eq. 6.2)*

$E_R = E_R\ \sin(\omega t + \alpha_R)$ *(Eq. 6.3)*

$E^2 = {E_I}^2 + {E_R}^2 + 2E_I E_R \cos(\alpha_R - \alpha_I)$ *(Eq. 6.4)*

$f_o = \frac{r^2}{2mW}$ *(Eq. 6.5)*

$f_z = \frac{r^2}{m\lambda}$ *(Eq. 6.6)*

$f_{lens} = [1 - n]\left(\frac{1}{\mathrm{r_i}} - \frac{1}{r_o}\right)\left(\frac{(1-n)d}{r_i r_o n}\right)$ *(Eq. 6.7)*

$f_{img} = \frac{f_{lens}\, r^2}{r^2 + 2f_{lens}\, mW}$ *(Eq. 6.8)*

List of Publications

- AlQattan, B, Butt H, Sabouri A, Yetisen A.K; Ahmed R, Mahmoodi N, Holographic direct pulsed laser writing of two-dimensional nanostructures." *RSC advances,* 2016, *6* (112), 111269-111275. (Chapter 3)

- AlQattan B, Benton D, Yetisen A.K, Butt H, Laser Nanopatterning of Colored Ink Thin Films for Photonic Devices. *ACS Applied Materials & Interfaces*, 2017, 9 (45), 39641–39649. (Chapter 4)

- AlQattan B, Yetisen A. K, Butt H, Direct Laser Writing of Nanophotonic Structures on Contact Lenses, *ACS Nano*, 2018, *12* (6), 5130–5140. (Chapter 5)

- AlQattan B, Benton D, Butt. H, Grating Lens for Imaging and Sensing Devices (2019 submitted). (Chapter 6)

Other Publications

- Ahmed R, Rifat AA, Sabouri A, AlQattan B, Essa K, Butt H. Multimode waveguide based directional coupler. *Optics Communications*, 2016,370:183-91

- Khalid, M W, Ahmed, R, Yetisen, A K, AlQattan, B; Butt, H, Holographic *Writing of Ink-Based Phase Conjugate Nanostructures via Laser Ablation. Scientific Reports,* 2017, *7* (1), 10603.

- Rashid I, AlQattan B, Yetisen A. K., Hassan M, Butt H, Ti Nanopatterning for Biological Sensor (2019 submitted).

- Haodong T, AlQattan B, Butt H, Cost-Efficient Smart Contact Lenses Based on Direct Laser Interference Patterned Graphene *(2019 submitted)*

Chapter 1: THESIS INTRODUCTION

1.1-Introduction

This thesis presents an investigation of the use of Holographic direct laser interference patterning (DLIP) for nanophotonic applications. Holographic DLIP is a single laser beam reflected by a mirror to allow rapid creation of high-resolution multiple laser beams on a target substrate. Photonic materials and periodic nanostructures are needed for numerous optical applications to become a new, strong path to solve important and challenging problems for human needs. Photonic structures can be fabricated by many types of processes; however, most of the nanofabrication processes are costly, time consuming and not flexible. Incorporating a meniscus lens with laser in front of a holographic Denisyuk reflection mode system was used to give three parameters for fabricating, optimizing and producing a rapid and low-cost nanostructure on ultra-thin films of metal. On the other hand, the challenge of using thin films of metal caused a thickness obstacle for efficient light diffraction from the nanostructure.

Photonic nanostructures of different synthetic dye-based inks were researched to reveal different optical properties. The synthetic dye-based media consisted of four ink colours (black, red, blue, and brown). Nanopatterning structure were produced by holographic DLIP to form constructive antinode fringes of electromagnetic gratings in dye-based inks. A thick nanostructure film of material (ink) was generated by multiple laser wave interference fringes to form the gratings. Although the four different types of dyes have the same periodicity, they produced a distinctive wavelength reliant on diffraction responses to monochromatic and broadband light. This occurs as they have different absorption characteristics which allow them to be used as low-cost nanophotonic structures.

Contact lenses are one of the global low-cost self-shelf biomedical devices used for vision correction. They could be used as quantitative analytical devices. It could be considered as highly promising for a point of continuous diagnostics care if nanostructures were united on the contact lens' surface. However, integrating nanoscale features into commercial contact lenses to produce low-cost biosensors is a challenge. The holographic interference was applied to generate optical patterning nanostructures over the surface of a hydrogel contact lens. The laser was able to produce one-dimensional (1D) and two-dimensional (2D) nanostructures on contact lenses. The holographic optical properties of these nanostructures were verified through different environmental conditions: ambient moisture, fully-hydrated, and artificial tears to demonstrate immediate optical alteration of diffraction from 41 to 48 degrees. The formation of 2D nanostructures on lenses increased the diffraction efficiency. The holographic laser ablation method demonstrated the versatility of 2D nanopattern geometries on contact lenses, showing one of the insignificant changes on the contact angle. The holographic nanostructures on the contract lens were used to sense the concentration of Na^+ ions to simulate the conditions in dry eye syndrome; the nanostructures detected the electrolyte concentration changes of (±47 mmol L^{-1}). Nanopatterns on contact lenses may be used to sense other ocular diseases in the early stages at point-of-care settings.

Large constructions, buildings, bridges, and aircraft require structural health monitoring. Due to their structural complex systems, extremely large and non-planar surfaces require very costly alert systems. The holographic interference patterning mode was utilized to produce another non-linear nanostructure via synthetic black dye to make low-cost and highly improved light sensing. The Fzp and curved nanostructures were made over a strong adhesion tape's surface as a tension indicator for monitoring and recording the health condition in civil engineering

and airplanes. Curved nanostructures could provide a strong signal of light to spot a change of a single or composite material tear or a building crack. Integration of a nanostructured substrate on a tape provides a light, flexible and ductile response to measure any fine change in unconventionally shaped structures. In addition, generating 2D distortion nanostructure with different sizes could deliver sensing and images at the same time for the target region.

1.2-Aim and objectives

1.2.1-Aim

The aim of this PhD thesis is to fabricate low-cost nanostructures for optical applications by using holographic DLIP of the Denisyuk reflection mode. The implications of four research studies are to investigate the effects of nanostructure spacing, material and shapes in order to fabricate economical, reliable, fast response optical sensors.

1.2.2-Objectives

The thesis' research confronted a number of challenges. Finding a reliable material and a feasible method to control nanopatterning structure spacing were the main challenges. In addition, finding the right thickness and type of material which could respond with the designated system (holographic DLIP) was a challenging task. Research of a new, efficient material which has good optical properties was necessary. Finally, optical nanostructures can be used to achieve effective low-cost solutions for some of existing problems. In order to achieve the research goals for this thesis, we can arrange the objectives in different stages:

1- A comprehensive review of the different nanofabrication processes has been conducted and it identified the advantages/disadvantages of these processes (Chapter 2).

2- Studying optical factors, nanopatterning, and understanding the nanofabrication mechanism (Chapter 2).

3- Selecting a material which has been used in nanotechnology as Au, to repeat-produce nanostructures (Chapter 3).

4- Studying the laser wave influence on material thickness and laser wave interference to create nanostructures (Chapter 3).

5- Finding the allowable parameters which could manage nanofabrication and optimization of the grating geometry (Chapter 3).

6- Creating different 2D nanopatterning shapes and analysing their optical properties (Chapter 3).

7- Identifying a new material that could respond to holographic DILP to make nanostructures (Chapter 4).

8- Studying optical properties (absorption) of the new nanostructure (Chapter 4).

9- Applying the developed nanostructuring solutions to some existing challenges

(Chapter 4).

10- Demonstrating nanostructure use for biosensors in optical applications (Chapter 5).

11- Generating a holographic curved nanostructure to make a nanophotonic strain sensor for engineering, aircraft and human intervention (Chapter 6).

1.3-Thesis structure

This thesis consists of seven chapters and supplementary material.

Chapter 1 includes the research topics covered in the thesis, the project's aim, objectives and the thesis' structure.

Chapter 2 is a literature review of nanostructure history and other nanostructures. It looks at the theoretical background and experimental researches.

Chapter 3 introduces a nanofabrication technique; there are different techniques to fabricate nanopatterning, however, they are costly. In this chapter a technique is introduced with some parameters to control 1D/2D nanostructures by laser holographic DLIP.

Chapter 4 presents different synthetic dye-based inks (black, red, blue, and brown). The nanostructure of the four inks has different optical properties. The thickness of the dyes helps to improve the optical dyes' efficiency. Several experimental investigations on the nanopatterning ink dye are carried out to show the advantages of these materials. Finally, some of the potential applications are shown.

Chapter 5 introduces the black synthetic dye used to fabricate nanostructures on commercial contact lenses. The nanostructure on the contact lenses was able to sense some eye diseases. The lens was exposed to different environments (ambient humidity, fully-hydrated with DI water, and fully-hydrated with artificial tears) to test the effectiveness and stability of the nanostructure.

Chapter 6 describes a technique of using black ink dye to produce a Fresnel zone plate and different curved nanopatterning structures. The curved nanostructure was tested to show a strong optical application integrated on a commercial adhesive tape for engineering, aircraft and human intervention sensing. The curved nanostructure on the tape was tested as a strain sensor and for other potential applications.

Chapter 7 discusses the research's summary and future work; and is followed by the references' list and supplementary material.

Chapter 2: LITERATURE REVIEW

2.1-Introduction

This chapter presents a literature review of the history and background of human interest and needs in photonic structure. The review regarding some of the lithography methods used to produce optical structures is presented in section 2.2. Holographic direct laser interference lithography and light response with photonic structure is discussed in section 2.3. Laser wave interaction with nanopatterning colour structure and the effect of the patterning's thickness on efficiency are presented in section 2.4. Integrating nanostructures on contact lenses for biological sensing application is discussed in section 2.5. Finally, producing optical strain sensing from non-linear structures on adhesive tape is considered in section 2.6.

2.2-Photonic applications

Humans have a great interest in natural materials. Engineers have always tried to use existing materials to produce substances that have better properties for the desired needs. In optics, making a material which can respond with light waves was a challenge. Scientists invented photonic materials which have a great response with visible light waves (400 nm-700 nm) over a certain frequency, by refracting and guiding them to a specific direction. This light (photons) can be used in manipulation and detection through transmission, emission, modulation, switching and detecting[1]. In addition, this material performs an important role in optics used in many fields, such as telecommunications, laser engineering, information processing, storage, sensing, solar cells, light emitting diodes, magneto-optic memories, video systems, colour

imaging and other industries [2-6]. Photonic materials can have different dimensions. It's important to explain one of the main periodic photonic materials which considers light wave propagation normal to the interface planes; it is called optical grating. Light within a material is no longer just an optical wave field if it enables an optical response to be made on the target material [7].

2.2.1-Grating history

Spectroscopy is the study of interaction of a material's composition with the wavelength of light. Diffraction grating is one of the significant elements in spectroscopy because it has a strong ability to disperse polychromatic light into constituent monochromatic light. Gratings are used to determine the life of chemical species in samples. They are also used in telecommunication to increase the capacity of fibre-optic networks [8]. An American astronomer, David Rittenhouse, was the first to report on diffraction grating in 1785 [9]. In 1821 Joseph von Fraunhofer began to work on diffraction grating to measure the absorption lines of the solar spectre and to derive equations of dispersive behaviour grating. Keeping the grating spacing uniform between the grooves has been the main objective to provide a good diffraction grating. It was a challenge to produce precision diffraction gratings and it attracted much attention from many of the world's scientists and technicians. Cornu (1893) realized groove spacing responded with light [10]. In 1947 Bursch and Lomb developed the first ruling engine at the University of Chicago. This engine was originally designed by Michelson in the 1910s and rebuilt by Gale. It managed a diamond ruler to produce gratings with 20 coarse grooves per millimetre (g/mm) [11].

2.2.2-Varied line space (VLS)

Cornu discussed that variations of the groove spacing modified the curvature of the diffracted wavefronts. While periodic random variations would produce stray light. He realized that using a uniform variation in groove spacing across the grating surface could be used as a function position to control grating surface spacing [12].

2.2.3-Modern lithography

Since the late 1960s, the industry has used a mechanical ruled machine to manufacture individual grooves by burnishing with a diamond tool. It has been used to manufacture gratings of 1000 grooves per millimetre. However, the aberration of ruled gratings was limited due to the mechanical motions. Modern industries have more requirements than before, such as speed, lower costs, and high precision [12]. In modern days, many tools have been used to make highly defined optical structures. There are many different types of lithography, which is the main process to reshape optical material structures [13].

2.2.3.1-Nano-printing through optical lithography

Photolithography is used to transfer a pattern from a mask to a photosensitive layer. Light and a mask are used for projecting patterns onto the target substrate surface to sacrifice some areas for patterns. As one of requirements in industry is to reduce patterning feature size, this has led to using shorter wavelengths as ultraviolet (UV) 365 nm and deep ultraviolet (DUV) from 100 nm to 248 nm to improve the structure spacing resolution [14, 15]. Usually a patterned mask made of glass or quartz is used to protect the area of the photoresist layer from light to produce

the patterning structure. The photoresist layer can be a mixture of organic compounds in a solvent solution. Positive and negative layers could be used. As a UV light is exposed to the photoresist layer the bonds of the exposed area break to become soluble and dissolve in the developing solution. The remaining photoresist under the mask remains, which is called the positive image. While the negative photoresist layer becomes harder as it is exposed to light, the rest is dissolved by a chemical developer [16, 17].

2.2.3.2-Moulding with UV-curing nano-imprint lithography

A mould with a patterned structure could be used for imprinting in one step. The mould is used to deform a thin resist film or an active material on a substrate. The mould material is made from hard quartz. The mould is pressed onto the silicon substrate at room temperature to transfer the pattern. High UV (400 nm) or thermal energy is used for curing and solidifying the imprint pattern, which is called cross-linking [15, 18-20]. After the mould is detached from the substrate, dry etching is used for cleaning the remaining layer to complete the process. Dry etching could be used on the target area by a bombardment of ions for cleaning [13, 21].

2.2.3.3-Stamping hot embossing nano-imprint

Similarly, a pattern can be transferred in one step by using a mould. A silicon mould is pressed into a thermoplastic polymer called poly (methyl methacrylate) (PMMA). The PMMA is pressed under a temperature of 200 °C and a pressure of 13100 kPa to take the pattern shape. When the temperature increases to the target point, the PMMA becomes rubber-like and starts to fill the pattern on the silicon mould. As the temperature decreases, the PMMA transforms

into a high mechanical-strength material. Then the mould can be separated from the sample and dry etching can be used for cleaning the PMMA residues to complete the process [22, 23].

2.2.3.4-Electron/ion beam lithography

A pattern mask and a pattern mould are usually fabricated by electron beam lithography. An electron beam (e-beam)/ion beam has highly sophisticated and precise nanolithography. Beams from electrons/ions are able to generate structures through focus to dimensions within a nanometre range and can be used to locally alter material at the point. Both can represent a direct nanofabrication tool which could fabricate 3D nanostructures [24]. As it uses electrical scanning with a thermometrically monitored mechanical motion, it enables the machine to achieve very complex patterns with a high resolution of structure spacing < 5 nm [25-29]. It is also considered as one of most successful lithographic techniques to create sub-50 nm metallic nanostructures with a great difference in the height-to-width aspect ratio [30]. However, there are many disadvantages of using the e-beam. The main cost of the e-beam is very high and it also requires expensive maintenance. In addition, high-tech equipment is required to run the e-beam [31-33]. Moreover, there are many types of materials which are harmed by the high energy of the e-beams. The consequence of the high energy can generate heating effects, radiolysis and knock-on damage on the material [34-37]. Additionally, to construct an unbroken surface structure it requires a long time for a small area [38]. Using the e-beam for writing about 1 cm^2 could need several hours to be completed [39].

2.2.3.5-Direct writing by nano/femtosecond laser

A laser pulse induces an interaction of radiation with matter. The incident radiation of a laser is used to conduct photons to transfer energy to a material lattice. A nanosecond laser used an external energy source to excite atoms from grade state to a higher-level state. Atoms rapidly plunge into a metastable level to emit photons and thus excite other atoms to release more photons, spontaneously emitted to discharge an intense pulse of light within the nanosecond range [40]. Laser spot ablation could be used as a lithography method. The delivered photons generate thermal energy to melt, boil and vaporize the material lattice. This electrons' vaporization process is characterized as ablation [41, 42]. The effect of laser fluence (energy/area) pulse ablation thresholds is used as a measurement for controlling the ablation zone per pulse. Increasing the number of pulses or the energy level would increase the heating of the vaporization/ablation for more depth [43]. A femtosecond laser makes limited damage on optical surfaces due to a decrease of the pulses' timespan. It could remove a very small range of micrometre diameter, 20 µm to 30 µm, to make better ablation control. Making an optical patterning structure would require many incremental single steps of 1 µm between each laser pulse to form an optical geometry [29, 44, 45].

2.2.3.6-Laser nano- patterning

Another method involves photographic recording of a stationary interference fringe field. It could be considered as one of the advanced processes for creating a mic/nanostructure by direct laser interference patterning (DLIP). This method is able to fabricate a periodic patterned structure on planar and nonplanar surfaces. This DLIP could fabricate complex patterns with varying dimensions. In addition, this technique would produce large areas within a short period

of time, of up to several cm^2/s using a single, or multiple laser beams. The laser beam can be split into two or more coherent laser beams and they intersect with each other to make a standing wave pattern in the region of the intersection (Appendix, Figure 2S.1) [12, 46]. The DLIP can be used on metals to make a photothermal effect. This type of process involves a localized meeting and selective ablation zones of the material at the interference maxima positions of the laser waves [47]. An optical system requires strict maintenance of mirrors, collimating optics etc. to produce the best contrast and fringe structures through laser interference [46].

2.2.3.7-Single-beam interference

A single collimated monochromatic coherent light beam reflects back upon itself to make an interference pattern; this system is called holographic DLIP [48, 49]. Holographic DLIP reduces the cost and complexity of the optics' set-up to save more time. The generated interference pattern on the substrate surface (photoresist) is called holographic grating (sinusoidal shape), where the spacing (Λ) depends on the angle (Θ) between the substrate surface and the plane's surface. The groove depth (h_c) of a holographic grating could be affected by the substrate thickness and reflective index of a material(n_o); while (c) represents the speed of light (Eq. 2.1). A holographic DLIP system is able to produce 10,000 grooves per holographic millimetre [12]. This system rapidly could create low-cost and flexible optical 1D and 2D nanostructures [50]. The rapid nanopatterning structure can be used as an important economical tool to produce different optics' applications [51, 52].

$$n_o=\frac{C_{vacuum}}{C_{material}} \quad \text{(Eq. 2.1)}$$

2.2.3.8-Lithography systems' comparison

The range of lithography techniques are also affected by capital and the cost of the maintenance of the tools. There are a large variety of devices that could be used in nanotechnology. Since every lithography technique could be affected by structure resolution, shapes, dimensions and production rate, it can be classified in general with number and the devices' classification is needed to build a lithography system (Table 2.1).

Table 2.1: Comparison among lithography techniques' equipment

Lithography	Capital cost	Operation cost	Structure resolution
Nano-printing (optical-proximity)	Condenser lens, DUV/UV source, photomasks, objective lens	Photoresist, photomasks, chemical solution (developer)	2-3 μm [53, 54]
Moulding with UV- nano-imprint	Condenser lens, UV source, transparent quartz /silicon mould	UV curable monomer, interment for retaining nanoscale cleaning	a few tens of nanometres [29, 54, 55]
Stamping hot embossing nano-imprint	Condenser lens, , quartz/silicon mould	Elastomeric elements, source of heat, instrument for retaining nanoscale cleaning	6-40 nm [29, 55]
Electron/ion beam	Electronic beam source, 1^{st} condenser lens, beam blanker, 2^{nd} condenser lens, aperture, deflector, final condenser lens, interferometric stage, PC control set-up	High energy source, annealing, clean room equipment, cooling system	< 5 nm [29, 56, 57]
Direct writing by nano/femtosecond laser	Laser source, beam expander, z-modular, theta lens objective lens, mirrors, mechanical stage, PC control set-up	Cooling supply	a few micrometres [58-60]

Laser nano-patterning	Laser source, aperture, lens, multiple mirror, beam splitter	Highly precise mirrors' alignment	a few hundred nanometres to micrometres [41, 46]
Single-beam interference	Laser source, dielectrics mirror, a mirror, a sample holder	Distilled water for cooling	a few tens of nanometres to micrometres [48, 61]

2.3-Holographic DLIP and light on grating structure

2.3.1-Electromagnetic waves and holographic DLIP

The term laser, is a short form of (light amplification by the stimulated emission of radiation). The radiation is produced from adding an element of neodymium to transparent material to the crystal yttrium-aluminium garnet (YAG). The host materials excite the light by emitting photons from atoms. These emitted photons have a single wavelength (monochromatic) and they move in phase with one another in a narrow range (coherent) [40]. A laser beam has standing waves which contain electromagnetic waves and can interact with many types of materials [40, 62]. In the late 1800s, J.C. Maxwell provided evidence that the light/laser has electromagnetic waves in nature. He generated an equation to explain the relation between an electric fields (E) and a magnetic field (H). The two fields have an interdependence relationship. Any produced light waves have an E-field and a H-fields and everywhere they are perpendicular to each other as time varies. When the sets of E-waves and H-waves constituently propagate in one axis, they are considered linearly polarized waves. Wave propagation is called wave plitude (Figure 2.1) [63].

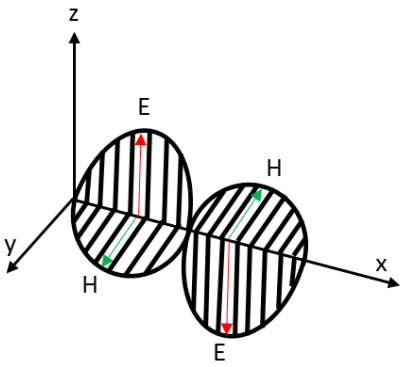

Figure 2.1: Electric and magnetic waves' relation

2.3.2-Laser interference

The phenomena of interference depend on one or more beams of a high intensity laser waves' overlap in some region of space (a substrate). The components of any electromagnetic wave can be described as scalar on three dimensions at x, y, and z- axes (E_x , E_y, E_z, H_x , H_y, H_z). The interference could be considered as deriving from the laser beam waves propagation along the same line, along the positive x-axis (assume horizontally and parallel) and sharing the same common constant plane. It could be described in terms of an E-field component because the H-field has lower energy than the E-field. As the two waves with the same frequency and speed overlap to make the two harmonic waves, they add to each other. The resultant of the two E-waves field of E_I-incident electric wave with E_R-reflection electric wave produces a superposition wave (Eq. 2.2) (Appendix, Figure 2S.2) [64].

$$E = E_I + E_R \qquad \text{(Eq. 2.2)}$$

Similarly, if two E-waves of the same frequency propagate in opposite directions, they would construct a superposition wave as they overlap. The E-waves are a sine wave and harmonically vary by time E(x, t), at certain zero points called nodes(x = 0, $\frac{\lambda}{2}$, λ, $\frac{3\lambda}{2}$,…..) . While the half way

point between each two nodes of amplitude at (x=$\frac{\lambda}{4}$, $\frac{3\lambda}{4}$, $\frac{5\lambda}{4}$…..) have the maximum values (superposition) and these points are called the antinodes (Appendix, Figure 2S.3) [62]. **The holographic DLIP** used the same method of interference of opposite directions. However, the interference could be used at the vertical axis (z-axis). The laser beam propagates through a thin film coated in glass and is reflected from an underlying plain mirror which is called the Denisyuk reflection mode system (Figure 2.2). The interference can happen when a reflected laser beam interferes with the same incident beam waves to make a concentrated energy zone. This zone generates interference fringes to make ablation on the target film in horizontal and vertical directions. The interference produces constructive interference which allows the node of the magnetic field to overlap with an anti-node of the electric field and vice versa [62].

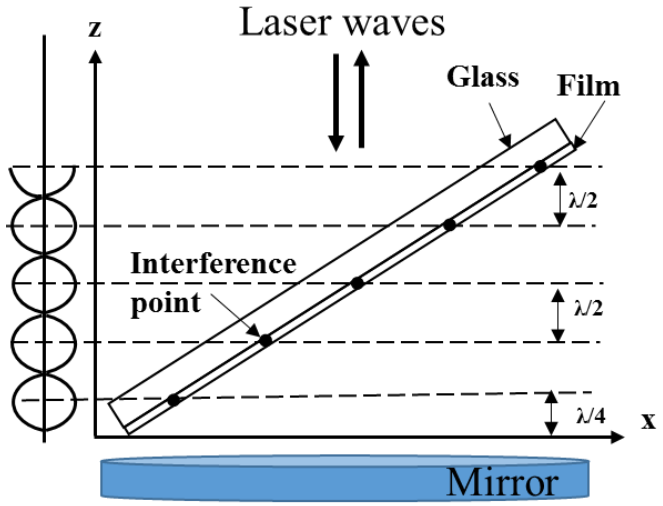

Figure 2.2: Laser light interference in DLIP Denisyuk reflection mode

The superposition wave of contractive interference (anti-nodes) could reach (1/2) the laser wavelength to make a number of ablation lines as (m=$\frac{1}{2}$,$\frac{2}{3}$,$\frac{5}{2}$,..). While the grating fringe could be controlled by changing the exposure angle [12, 49]. Further discussion about holographic interference theory is covered later in (Chapter 3) and in the experimental chapters.

2.3.3-Light propagation

The phenomena of light propagation relates of light interaction with material media. When passed through a medium, light velocity depends on the electric and magnetic properties of the medium. Light waves can pass in two different media. As laser waves strike against the interference separation of the two media, a portion of the incident waves or flux density will be diverted back to become reflection waves and the rest will be transmitted across the second material boundary as refracted waves (Figure 2.3) [63].

2.3.4-The law of transmission, reflection and refraction

Snell's law determines incident wave behaviour on the plane of two different interface transparent mediums. Frequency harmonic waves represent the number of waves arriving to the interface per second, as denoted with v. The waves could be reflected and transmitted waves at different periods to become secondary wavelets; they have the same frequency. The elapsed period is t = 1/v. As light waves pass from the incident medium with refractive index n_i and transmit to second higher medium n_t, the light waves would diffract. The incident waves travel with a speed v_i=c/n_i; while the speed in transmission medium n_t is v_t=c/n_t and because $n_t > n_i$ would make $v_t < v_i$ (Figure 2.2) [65, 66]. If the incident of waves is with angle θ_i then it generates angles reflection θ_r and transmission θ_t. As the transmitted wave has an angle, it can be called a refractive wave. It could only occur between two transparent materials (Eq. 2.3, 2.4) [40, 63].

$$\frac{\sin\theta_i}{\sin\theta_t} = \frac{v_i}{v_t} \qquad \text{(Eq. 2.3)}$$

This produces the law of refraction:

$$n_i \sin\theta_i = n_t \sin\theta_t \qquad \text{(Eq. 2.4)}$$

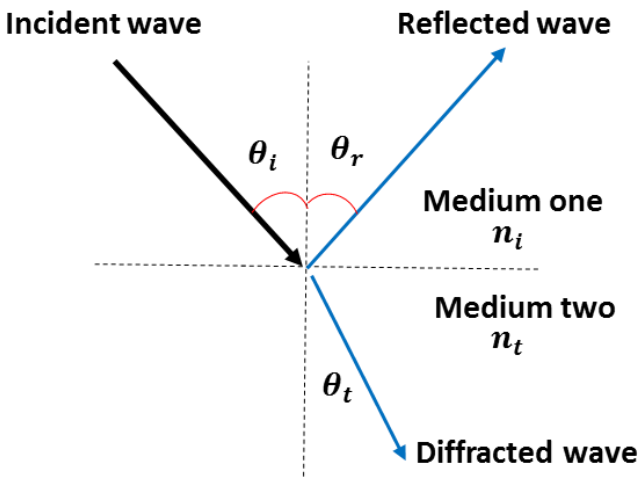

Figure 2.3: Reflection and transmission through different mediums

2.3.5-Refraction through an aspherical surface

A lens has an aspherical surface with a radius centre (r) which has a refractive surface; Snell's law gives the principle reason as the change of mediums (air and glass). A lens has two radiuses: an inner radius and the outer radius. As a laser point source placed in front of a lens, the ray will refract or converge to a distinctive point and then diverge. This distinctive point is called the focal point (f_{lens}) of the lens. There are further details in Chapters 3 and 6.

2.3.6-Light and diffraction grating

Monochromatic light should be discrete as it reaches a grating surface. Different monochromatic light could be used in optic analysis. Illuminated laser beams are directed to

periodic samples as blue a wavelength centre of λ = 450 nm, green - λ = 532 nm, and red - λ = 635 nm for measurement. This discrete representation responds' with each groove to form a set of diffracted wavefronts. An incident light ray of wavelength is affected by structure grating spacing (Λ) to be diverted with a diffraction angle (α) (discrete angles). This angle depends on whether the light is diffracted on the same side to make a reflection or the opposite side of the substrate to make transmission diffraction (Figure 2.4(a-b)) [67].

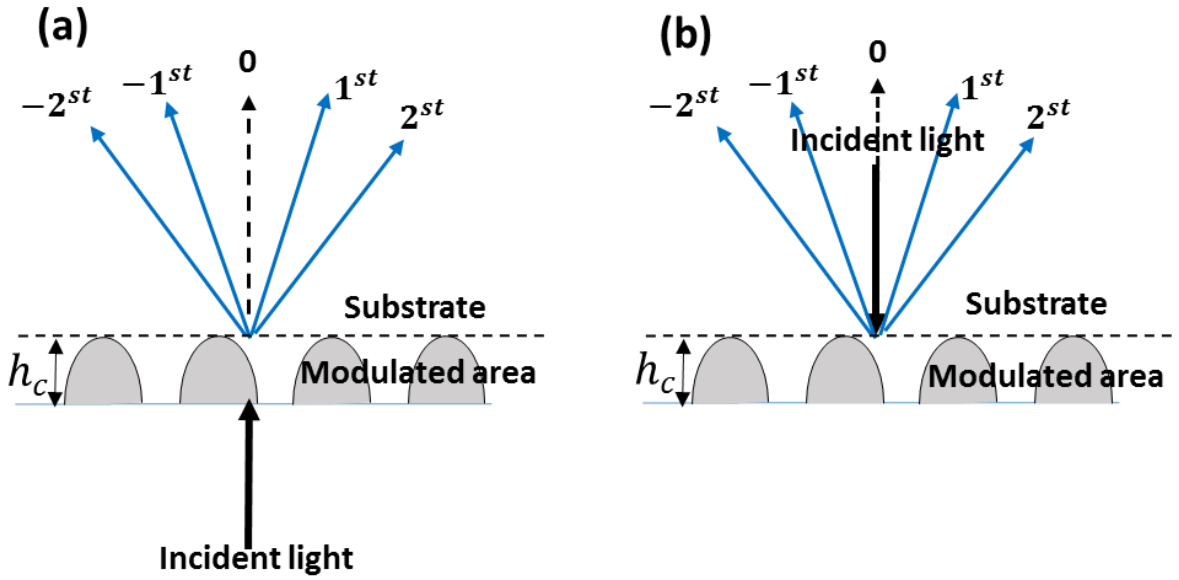

Figure 2.4: Holographic grating on diffracted incident light of a grating structure by (a) reflection, (b) transmission

Either reflection or transmission is measured from an incident light wave perpendicular to the grating surface. The diffracted orders clockwise from the incident light are called positive orders; while the negative orders are considered from counter-clockwise of the incident light [50]. Usually the reflection point results from an incident wave of a metal surface [65]. In our research, the transmission has been used as the main character of the diffraction measurement because it is more relevant to our applications.

2.3.7-Light dispersion grating

The primary rule of a grating structure is to scatter or diffract a single wavelength (illumination). While if white light is used on gratings, it can be separated into several wavelengths. White light dispersion is an important optical property to measure patterning structure efficiency. Dispersion can be measured per unit angle or per unit length [12, 68]. A customized set-up has been used in our research on different types of structures (Chapters 3-6).

2.4-Colour material and film efficiency

2.4.1-Colour material

Living creatures in nature have a wide variety of attractive photonic structures, which have distinguishable roles to confine light and to reflect specific visible colours [69, 70]. It has inspired the development of different nanostructures for diverse types of optical colouration [71, 72]. Optical nanostructures in nature can be replicated to be used in optical applications [73]. This means nanomaterials which can produce colouration from different surfaces is extremely desirable for some applications. The colourization of nanomaterials can be miniaturized for multifunctional optoelectronic devices. Nanostructural materials can be produced by a variety of advanced methods. Metallic nanostructures which could generate subwavelength structures are able to develop a strong reflection of color. The metallic materials have a high refractive index, which makes the nano-metallic structure durable and generate stable colours [74-76]. Nanoparticles from latex polymer particles also have very attractive colours due to facile chemical modification and composition adjustment. They can

be produced as independent patterned structural colours which have good wavelength reflectance. They also can have various shapes, and chemical and physical properties to make them easily fabricated and modified. They are deposited in micrometre quantities and assemble as a unit by inkjet printing. They could be arranged as a three-dimensional dielectric structure to make a photonic band gap [77, 78]. This allows them to be used in semiconductor microelectronic and plastic electronics to produce high performance devices for medical and industrial technology applications [79]. Silver nanoplates (SNPs) are another colour type which can be produced on a large-scale and are assumable as metallic film for tuneable plasmatic properties. Monolayer metallic ultra-films (8-20 nm) could be used as surface plasmon resonance and tuned to a selected wavelength range of 500-800 nm. Excitation of the metallic nanostructure can induce incident light to lead to great optical local–field enhancement to make effective wavelength-photon scattering [80]. This generates the ability of controlling and manipulating light to be used on sensors [77]. In addition, blue phase liquid crystal (BPLC) is composed of uniform lattices which can be rearranged to desired directions to use them on photonic applications. Liquid crystal (LC) is soft matter placed in the order of 3D cubic architecture, which has dimensions of a few hundred nanometres. The BPLC also has a sensitive response which is stimulated with temperature, electric fields, and light irradiation. Micropatterning of a crystallographic direction could be arranged in a uniform orientation to reflect different colour and temperature change [81-83]. Laser pulses induce transient local heat which leads to melting and reshaping to form nanostructures. Controlling laser power, spot size and frequency, besides the spot location, would manage to reach the target nanoscale [84]. The nanometre-size features could be used as plasmatic resonances leading to different visible colour [85]. Colour nanostructures could be generated by holographic DLIP for low-cost optical applications [51].

2.4.2-Material efficiency

Holographic DLIP set-up requires material substrate film thickness which could allow laser waves to pass through it and reflect to produce a holographic pattern structure. Thin film material is usually used for laser interference, to generate the thin grating of amplitude transmittance [68, 86]. On the other hand, thick metal film would not allow a laser pulse to transmit for ablation in holographic DLIP system. Amplitude grating could also generate a nanopatterning structure which is described as an absorption coefficient. Although sinusoidal thin gratings have good transmission of diffraction grating efficiency, a sinusoidal absorption grating has better efficiency [87]. The diffraction efficiency of the grating was considered to come from the well-defined structure spacing, which is able to interact with incident light to diffract intense and visible order points (Figure 2.5). Efficiency is influenced by wavelength and is considered an important characteristic of diffraction grating quality (Table 2.2). It is desirable to achieve a high-efficiency grating because it is a measure of good structural lines on optic spectra [88]. It also implies that higher diffraction energy means lower stray light. It would be practical to consider five domains of sinusoidal-groove gratings, progressively increasing in modulation efficiency (μ) [12].

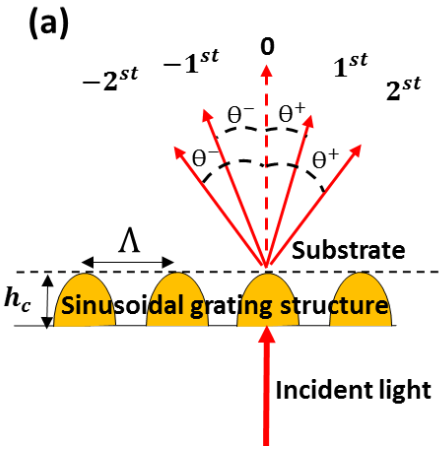

Figure 2.5: The thickness of sinusoidal grating structure influences the diffracted order efficiency

$\mu = h_c / \Lambda$ (Eq. 2.5)

Table 2.2: Grating efficiency range

Domain	Modulation
Very low	μ<0.05
Low	0.05 <μ<0.05
Medium	0.15<μ<0.25
High	0.25<μ<0.4
Very high	μ>0.4

Holographic dielectric nanostructures from low-cost medium with high absorption would provide a great example of good efficiency [89]. They would provide a degree of phase shift based on a change from material refractive index. When the waves pass through the incident medium due to refraction there is a phase shift for the transmit wave. The dielectric material can be effective as an absorption constant, which can help to propagate a light wave through boundary conditions at the entrance surface of the medium. Knowing the medium thickness (h_c), wavelength (λ), the average refractive index ($n_{o)}$, and the grating spacing (Λ), the diffraction could be calculated more precisely [90]. Four synthetic film dye-based inks (black, red, blue, and brown) have been used to measure different optical properties of 1D nanostructures (Chapter 4).

2.5-Biosensor contact lenses

Holographic DLIP reflection mode can be used for the adoption phenomena of black dye to generate nanostructures on contact lens, to detect some leading causes of blindness.

2.5.1-Selecting contact lens

A number of ocular diseases are associated with increasing medical services' costs. Some of these diseases affect near-sightedness or far-sightedness and they alert the patients to have their eyes examined [91]. However, there are some diseases which are the leading causes of blindness among working age adults, but are not checked in the early stages. Edema, graves', glaucoma, dry eye syndrome are some of the common diseases that affect a large number of people in the world [92-95]. Millions of people around the world suffer from dryness which usually starts as discomfort but can lead to blindness. There are many engineering solutions to solve the problems [96, 97]. A non-invasive technique is needed to make a continuous monitoring sensor. Tear fluid could be considered as an important external fluid to measure some significant levels in ocular diseases [98]. A contact lens is a small optical system placed directly on the cornea. Most contact lenses are made from a soft material composition to interact with tear film [99]. It could be used as a measurable device for care diagnostics if nanostructures are integrated on the surface to become biosensors. Different types of contact lens could be purchased from local markets. Studies on about 10 types and from five manufacturers of contact lenses have been carried out to measure surface roughness and the swollen state (Table 2.3) [100]. Surface roughness (R_{max}) and water quantity or the swollen state (q_w) have an important role in the comfort of lens wearing. Surface defects or poor wettability on any contact lens can cause irritation in the cornea. As the equilibrium content of water decreased the value of the surface roughness increased [101]. The R_{max} range 13-40 nm is considered as very high and a lens with a smooth surface should be below 5 nm. Acuvue Advance could be considered as a good lens even though its swollen state was in the medium range [100].

Table 2.3: Contact lens roughness and water content comparison [100].

No.	Commercially available Lenses	Material	R_{max} (nm)	q_w (%)
1	Acuvue 2	HEMA/MA	17.4	58
2	Acuvue Advance	Silicone hydrogel	4.1	47
3	Focus Dailies	PVA	14.0	69
4	Focus Night & Day	Silicone hydrogel	40.9	24
5	O2 Optix	Silicone hydrogel	35.3	33
6	Precision	VP/MMA	13.4	74
7	Purevision	Silicone hydrogel	32.9	35
8	SpofaLens	HEMA	5.7	39
9	Weicon	VP/MMA	132.1	60
10	W&V	HEMA	120.4	39

2.5.2-Nanostructure on contact lens and hydrophobicity measurement

Integrating nanostructures in soft contact lenses represents an essential challenge. There are different nanofabrication methods which could be used as in sections 2.2.3.1-7. A holographic laser ablation method could be the best for integrating low-cost optical nanostructures on contact lenses (further discussion in Chaptre 5). Making nanopatterning structures on a contact lens' surface could increase the hydrophobicity or contact angle and this could decrease the lens' softness. As the hydrophobicity is considered important, its range and the methods have to be addressed for measurement. The hydrophobicity range of water adhesion tension is based on the contact angle (Θ) measured between the hydrophilic and hydrophobic conditions. In hydrophilic conditions the water droplets spread over the material's rough surface with a contact angle of around zero. In hydrophobic conditions the water droplets become unstable on the material surface to form a contact angle of at least 90° (Table 2.4) [102].

Table 2.4: Contact angle range

Type of surface	Contact angle (°) range
Super hydrophilic	~0
Weak hydrophilic	(56-65)< Θ <0
Weak hydrophobic	90 > Θ > (56–65)
Hydrophobic	120 > Θ > 90
Super hydrophobic	Θ>150

Three contact angle measurement techniques could be used (sessile drop, captive bubble, Wilhelmy plate). A study has shown the sessile drop technique to be more effective and practical for contact lenses [103]. The sessile drop uses a syringe to place a drop of liquid on the lens' surface. It has many advantages, as it is fast, easy to carry out and it could be performed on static and dynamic contact angle measurements (Chapter 5).

2.6-Nanostructure for sensing and imaging

Fresnel zone plate and distortion structure patterning structures could be produced by holographic DLIP reflection mode. This project discusses the use of patterning structures to make an inexpensive strain sensor.

2.6.1-Strain sensors

Buildings and bridges are subjected to environmental change, especially in hidden areas which could damage the main supported construction. Strain sensors are needed as an alert system for structural damage in civil engineering and aerospace. They could be used for monitoring the structural health condition [104]. Many types of strain sensors could help in large deformation detection and on conventional surfaces. Bridges and airplanes are exposed frequently to

dynamic loads. Recently, some MicroStrain miniature strain sensors have been used to improve public safety. They use wireless embedded nodes on a large concrete bridge structure to provide wireless monitoring [105]. Similarly, non-destructive testing (NDT) techniques enable the use of current technologies to inspect bridge cables by robot. This technique uses high frequency sound waves to capture the reflected signal to detect cracks in the wires in the cables [106].

Fibre Bragg grating (FBG) is considered as one of the important strain sensors for air planes. It is used in aircraft because it helps to decrease maintenance efforts with low additional weight. It is distributed in a composite structure, similar to a human neural network. The FBG has been also used in health systems for bridges, and for monitoring dams. It measures a reflected change of wavelength or modulation of the refractive index from the grating, as an effective response of expansion and compression [107, 108]. Other types of strain transducers could sense large deformation. The Huper-Stratchable sensor uses a piezoelectric sensor made from PVDF nano/microfibres. It is capable of adapting to curved surfaces and withstanding high strain levels. It could measure along the x-direction with an average tensile speed of 20 mm/s [109]. Similarly, capacitive microelectromechanical strain systems and 3D acceleration sensors are used to measure the seismic response in a building. They are considered as low-power consumption MEMS wireless strain sensors for monitoring civil structures. They can measure plastic hinge activity and settlement with a range of > 1 km. A microelectromechanical sensor is able to report a displacement of +/- 5 mm; while an accelerometer strain sensor is capable of reporting a vibration acceleration signal of 0.2 m/s^2 [24].

Optical nanostructures could be used to make low-cost, feasible and high-response strain sensors. Nanostructures could provide an efficient response on unconventional structures'

surfaces [110, 111]. Modification of patterning structures could provide a non-linear response to adapt unconventional surfaces with a defined level of sensing. Displacement of grating lines would introduce arbitrary light wave shifts to form strong zero/non-zero orders (non-linear) as Fresnel zone plate (Fzp) and distortion structures; they could manipulate light with high efficiency for use in sensing [112, 113].

2.6.2-Fresnel zone plate lens and distorting patterning fabrication methods

The Fzp is thought of as an attractive device in photonics, which is used for focusing. The Fzp is constructed from multiple rings with a certain radius. They are repeatedly arranged as opaque and transparent circles. The arrangement of the rings would diffract to the focal point. The focal point is described as where light wave rays would converge towards a certain point or converge from it [62], and the Fzp focal point could be used for sensing and imaging [113, 114]. It could be fabricated with different techniques such as the ion/e-beam, femtosecond laser, photomask and others [115-117]. Another non-linear patterning structure is called the curved structure. This patterning is made similar to the grating structure; however, it has a distorted or curved lines' structure. The curved lines result from a quadratic displacement. The Fzp is caused from a group of circles; while the quadratic distortion is produced from arcs of circles (Chapter 6). The distorted lines' pattering structure is also able to interact with light to diffract multi-focal points [112, 118].

2.6.3-Quadruple wave

Using the Denisyuk reflection mode system enables us to produce two types of structure: Fzp and distortion patterning structures. However, the laser pulse standing wave is able to generate

a straight lines' grating structure based on laser beam reflection interference (Fig. 2.2). Replacing the flat mirror with a concave mirror could affect the reflective laser wave phase; the concave mirror has a semi-sphere surface shape and would change the refection waves to a quadratic waves. If the laser pulse is aimed at the mirror axis, it would generate an Fzp structure. An arc-circle structure would be produced if it reflected from the mirror off the axis. The reflected waves (quadratic waves) are considered as non-linear waves which interfered with the coming waves to form the Fzp or distortion structure [118, 119]. If the Fzp and distortion patterning structures are integrated on an adhesive tape, they could be used on unconventional constructions for imaging and strain sensors (Chapter 6).

Chapter 3: HOLOGRAPHIC DIRECT PULSED LASER WRITING OF TWO-DIMENSIONAL NANOSTRUCTURES

This chapter is based on a published Journal Paper, published online

AlQattan, B.[(1)], Butt, H.,[(1)], Sabouri A.[(1)], Yetisen A. K. [(2,3)], Ahmed R.[(1)] and Mahmoodi N. [(1)] Holographic direct pulsed laser writing of two-dimensional nanostructures. 2016, 6 (112), 111269-111275)

[(1)] Nanotechnology Laboratory, School of Engineering, University of Birmingham, Birmingham B15 2TT, UK.

[(2)] Harvard Medical School and Wellman Center for Photomedicine, Massachusetts General Hospital, 65 Landsdowne Street, Cambridge, MA 02139, USA

[(3)]Harvard-MIT Division of Health Sciences and Technology, Massachusetts Institute of Technology, Cambridge, MA 02139, USA

Author contributions: Bader AlQattan is the main author of the work and he addressed the idea of managing the main parameters to control the spacing of the nanostructure. He designed the experiments, executed all necessary optical characterization, performed data analysis, and wrote the manuscript. Rajb Ahmed contributed to the modelling/simulation work. Nasim Mahmoodi provided the different gold samples' thicknesses. The rest of the co-authors, Dr Ali K. Yetisen, Dr Aydin Sabouri and the principal supervisor, Dr Haider Butt reviewed and edited the manuscript.

3.1-Abstract

Laser interference lithography involves removing a very precise area of a material to reshape it for use in nanotechnology applications. Several methods could produce patterned nanoscale structures; however, many of them are expensive and require a long period of time. The fabrication technique of the laser holographic Denisyuk reflection mode (holographic DLIP) could be used to generate nanostructures on various thin films. The process is considered as low-cost, fast, and it is not complicated to produce the nanoscale features.

3.2-Introduction

Photonic materials and periodic nanostructures have a numerous of applications in sensing, spectroscopy, telecommunications, and security industry [2-5]. Photonic structures can be fabricated by many advanced processes that may achieve resolution down to 10 nm; however, achieving precise and uniform structures require sophisticated equipment and time consuming fabrication processes[31, 32]. Bottom-up fabrication of photonic crystals through self-assembly involves ion depletion of highly-charged particles from the solution requiring lengthy dialysis times[38]. Similarly, top-down fabrication of nanophotonic devices through e-beam writing over 1 cm^2 can take from hours to days to complete [39]. Hence, there is a clear need to develop low-cost fabrication techniques to rapidly fabricate large area periodic nanostructures with high resolution. Laser ablation compared to lithography/e-beam milling for fabrication of micro/nano structures is known as a faster method, moreover, it requires less number of processing steps[120, 121]. Laser ablation has been utilized to create optical devices operating in the visible region[122, 123]. Direct laser writing procedures have low energy requirements and rapid production times not only for one-dimensional nanostructures 1D but also for two-

dimensional 2D nanostructures[124, 125]. In particular, creating 2D structural gratings with high-resolution is highly desirable for optical applications including lasing, biosensing, and spectroscopy[126]. Likewise, direct laser interference patterning (DLIP), where single laser beam is split to produce interference of multiple laser beams on a target substrate, is capable of rapidly generating 2D nanopatterns. However, it has the disadvantages of requiring complex optical setups and precise control over system parameters, which increase the cost. Combining the advantages of DLIP with holographic DLIP can reduce the cost and time. Holographic DLIP involves an original laser beam reflection mirrors to allow rapid creation of high-resolution 1D and 2D surface gratings[3, 4].

3.3-The mechanism of surface grating

We previously described a laser patterning technique to create 1D ink gratings using a holographic patterning system[124]. The interference of laser light in a multilayer field allowed the ink to be ablated in antinode (constructive) regions of a recording medium[3]. The utilization of this approach created 1D parallel and radial gratings[4]. However, the effect of patterning parameters on the formation of surface gratings was not studied. In addition to the interference pattern geometry, understanding the mechanism and the effect of optical factors such as interference angle and superposition of the interference waves in the creation of gratings will allow controllable fabrication and optimization of the grating geometry. Also, the ability to rapidly fabricate surface gratings in 2D patterns remains elusive with this approach.

Here, we demonstrate the holographic DLIP strategy for rapid fabrication of 2D nanostructures at low cost. A pulsed nanosecond (ns) laser in holographic Denisyuk reflection mode was used to produce gratings in various metal thin films deposited on glass substrates. The system utilized

a highly-intense pulse, which created an interference pattern to ablate localized regions in the metal layer. We demonstrate this fabrication technique to tune the parameters in order to control the geometry and spatial periodicity of 1D and 2D gratings in squares and rectangular (parallelograms) arrays. Light diffraction from the 2D nanostructures was spectrally analyzed and angle-resolved measurements were performed to characterize the fabricated gratings.

3.4-Results and discuss

3.4.1-Fabrication technique

Figure 3.1a shows the schematic of the hologram recording setup in Denisyuk ablation mode. The laser reference beam initially passes through a meniscus converging lens to be focused (focal length ~ 8.55 cm) then it defocuses to form diverging beam. The lens increases the size of beam after the focus point as it moves in the z-axis (vertical) and the ablated spot diameter in Au film expand. The focal point (f) of the lens is:

$$\frac{1}{f} = [1 - n](\frac{1}{r_i} - \frac{1}{r_o} + \frac{(1-n)d}{r_i r_o n}) \qquad \text{(Eq. 3.1)}$$

where r_i is the inner radius, r_o is the outer radius, n is the reflective index, and d is the lens thickness. The reference beam propagates through the thin metal film and is reflected from the underlying mirror. The reflected laser beam (object beam) interferes with the reference beam to create concentrated energy zones (interference fringes) in horizontal and vertical directions, ablating the thin film at energy-concentrated antinode regions (constructive interference). The interference caused by the nodes of magnetic field overlap with antinodes of electric field. The electric (E) and magnetic (H) field vectors at the three axes (x, y, z) are:

$$E_x = -2A_x\,[\sin(\frac{\omega z}{v_1})\,]e^{-i(\omega t-\frac{\pi}{2})} \quad \text{(Eq. 3.2)}$$

$$E_y = -2A_y\,[\sin(\frac{\omega z}{v_1})\,]e^{-i(\omega t-\frac{\pi}{2})} \quad \text{(Eq. 3.3)}$$

$$E_z = H_z = 0 \quad \text{(Eq. 3.4)}$$

$$H_x = -2A_y\ n_1\,[\cos(\frac{\omega z}{v_1})\,]e^{-i(\omega t)} \quad \text{(Eq. 3.5)}$$

$$H_y = 2A_x\ n_1\,[\cos(\frac{\omega z}{v_1})\,]e^{-i(\omega t)} \quad \text{(Eq. 3.6)}$$

where A, ω, t, and λ_o represent axis plane, angular velocity, time, and wavelength, respectively. The position of antinodes can be predicted by $z = \frac{m\lambda_o}{2n_1}$ [64].

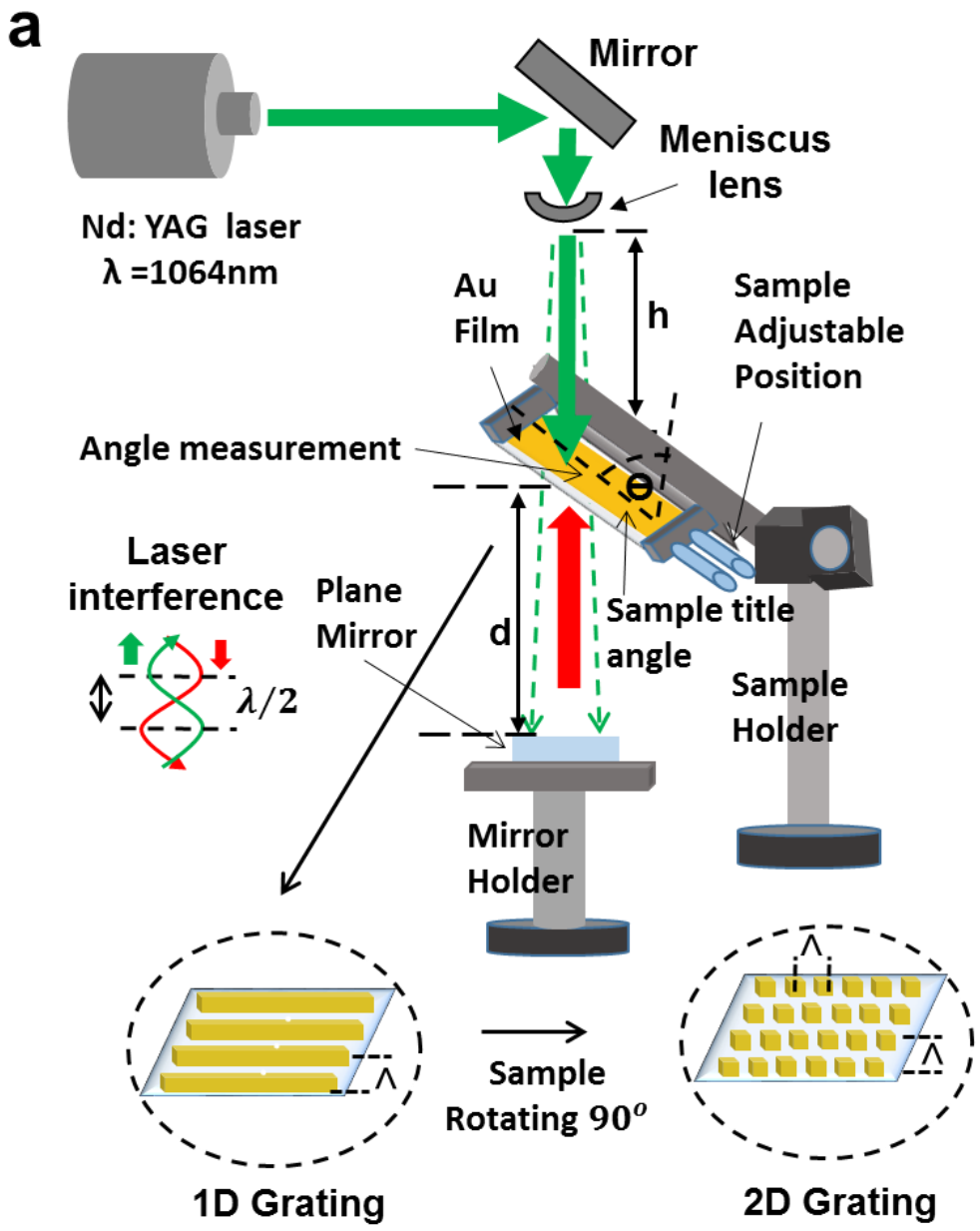

Figure 3.1: Fabrication of 1/2D patterns through nanosecond laser light interference in holographic DLIP Denisyuk reflection mode. (a) Nd:YAG laser beam (3.5 ns) propagates through a converging lens and reflected back from a plane mirror to ablate the localized regions of the recording medium (metal film).

The experimental periodicity (Λ) can be calculated from counting the average of ten structure lines on the optical microscope surface images. However, the theoretical periodicity cannot be calculated because the laser beam diverges with distance (h) (Appendix, Figure. 3S.4).

3.4.2-Computational modelling of the focused beam interference

To understand the optical interference-induced patterning with 1064 nm focused beam (through biconvex lens), which produce a grating in the Au film, computational modeling was performed using COMSOL Multiphysics simulation package based finite element method (FEM)[127, 128]. Scattering and periodic boundary conditions were set to define the interference pattern. The computational area was created with triangular meshing elements. The maximum degree of freedom was ~126,884. Completed mesh consisted of 17,963 domain elements and 1,183 boundary elements. Convergence test was carried out with fine mesh elements for improving the result accuracy[129].

Figure 3.2a illustrates the computation geometry and E-field intensity distribution for the focused laser beam interference. The normalized intensity profiles were computed for the tilted observation plane angle variation (θ= 30° and 45°). Peak distance decreased with larger tilt angles (Figure 3.2b). Figure 3.2c-d shows focused beam inference arc length or structure spacing (Λ) as a function of tilt angle of observation plane (θ) and distance variation (Figure 3.2d). As tilt angle of the observation plane increased, the interference spacing shifted to lower values. Similarly, the distance was varied to compute interference spacing. As the distance between mirror and observation plane increased, the interference spacing increased linearly. Hence, a 2D simulation was performed for the computation simplicity, reduce computation time with a μm range simulation domain that was smaller than the experiment. In addition, simulations at different wavelengths were performed. Figure 3.2e is showing interference nodes as a function of wavelength. As the optical wavelength is increased the grating spacing is also increased.

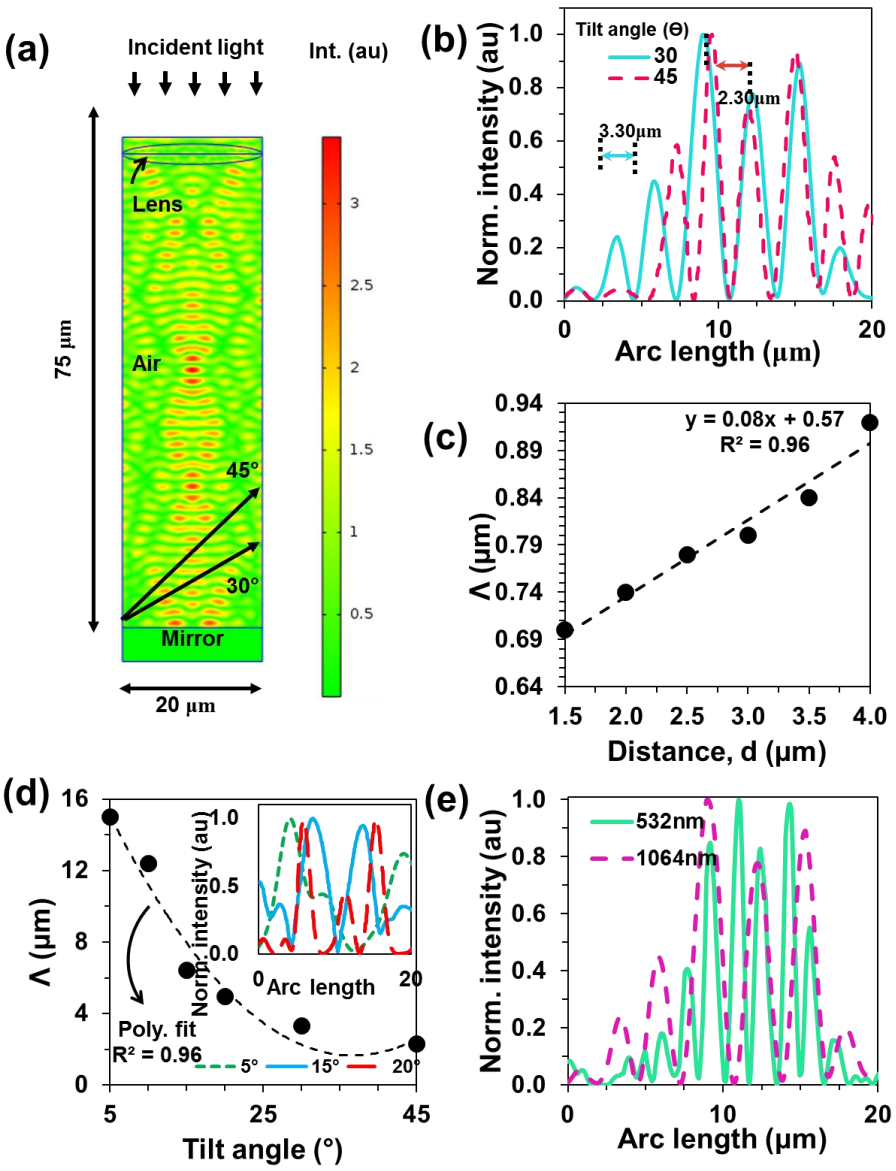

Figure 3.2: FEM modelling of the focused beam interference(a) Computational geometry for the focused laser beam interference and its 2D intensity distribution. (b) Normalized intensity profile plotted for the focused laser light interference at planes of 30° and 45°, respectively. (c-d) Focused beam interference spacing as a function of distance between mirror and the observation plane (*d*) and tilt angle (θ). Inset shows normalized intensity profiles as a function of arc lengths. (e) Grating spacing as a function of wavelength.

3.4.3-Diffraction grating and 2D patterns fabrication

An Nd:YAG laser beam (λ=1064 nm, 3.5 ns pulse) with a single pulse energy on the order of 330 mJ was used. The Au-Ti film of the nominal thickness of 14 nm (Au 10 nm, Ti 4 nm) was

patterned through controlling the tilt angle with respect to the surface plane of the mirror to create well-ordered gratings with different periodic spacings at each angle. Figure 3.3a-c shows the microscopy images of Au-Ti surface gratings with varying periodicity based on the tilt angle (θ). The periodicity of the grating was 7.7 μm when the tilt angle was 6° (Figure 3.3a); and as it increased to 15°, the periodicity decreased to 3.28 μm (Figure 3.3b). This approach allowed for creating highly-controllable gratings having a periodicity of ~980 nm at a tilt angle of 45° (Figure 3.3c).

The effects of the laser writing parameters on the grating formation were experimentally studied (Figure 3.3d-f). The tilt angle varied between 0° and 45°. Since the beam was not collimated, reducing the two parameters, height, h (lens - recording medium) and distance, d (sample - object), also contributed to decreasing the grating spacing (Figure 3.3e-f). The tilt angle variation had the highest impact on decreasing the grating spacing; and by using the three parameters together, the gratings were controllably fabricated and optimized.

Further studies were done on 25 nm Au coated samples. The pulse energy was varied from 30 mJ to 330 mJ and more details of the energy selection are found in the Appendix, (Figure. 3S.5-7). It was found that by increasing the energy, the width of grating bars were decreased which is due to more material ablation caused by more pulse energy delivered to the substrate (Figure 3.3g). The optical microscopy images of structures made by 330mJ are shown in (Figure 3.3h-i). Additionally, the number of consecutive pulses at same region was altered form (3.3j-l). By increasing the number of pulses, negligible changes in grating spacing were observed. However, it was found that the width of periodic grating bars is reduced, possibly again due to more energy deposition and further ablation. This three parameters optimization of structure spacing (Λ) is a repeatable process and it has used on four samples (Appendix, Figure 3S.8).

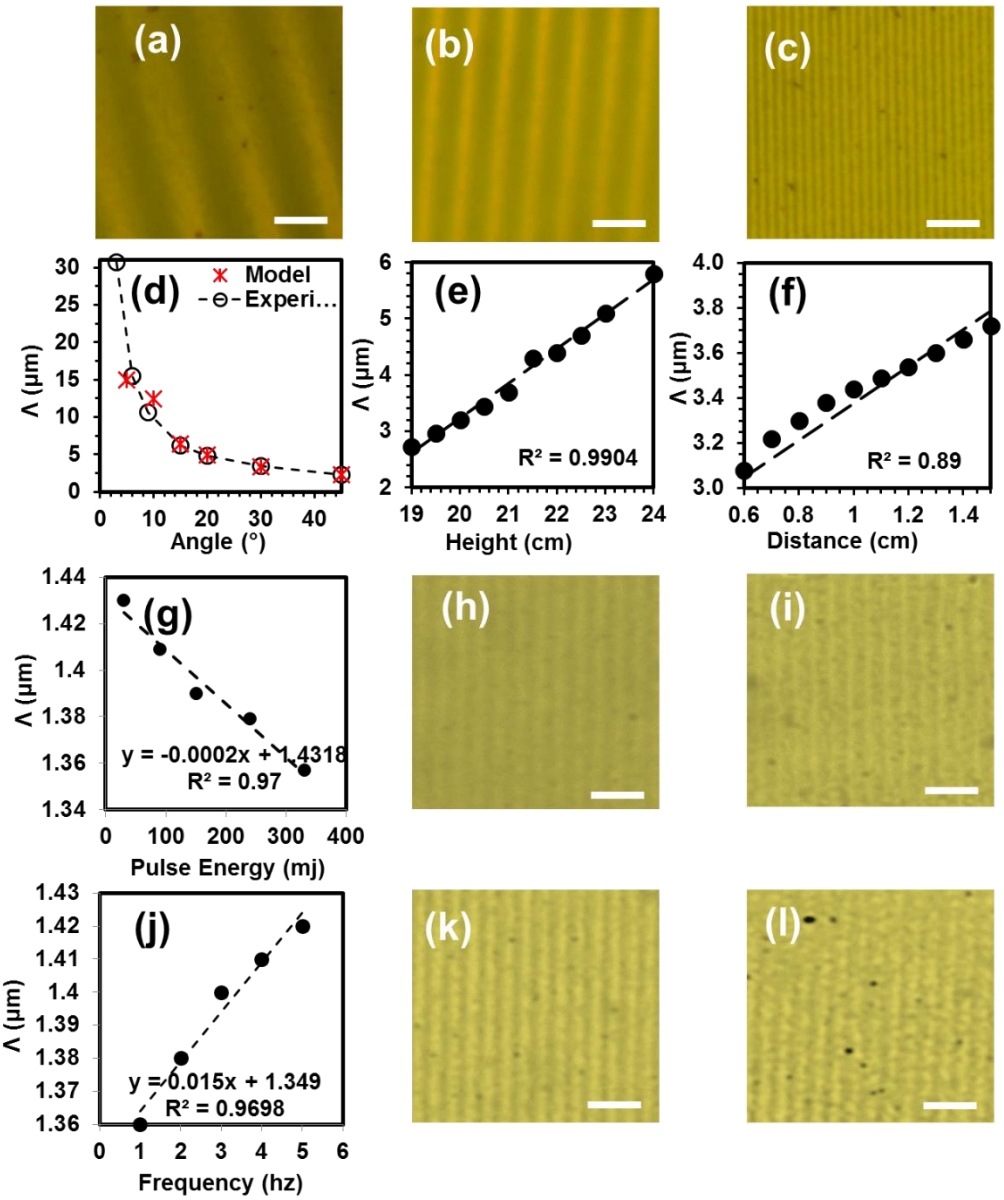

Figure 3.3: Microscopy images of the Au-Ti surface gratings fabricated by holographic DLIP. (a) Grating with periodicities of 7.7 μm, (b) 3.28 μm, and (c) 960 nm. The effect of changing (d) tilted and modelling angles, (e) mirror-sample distance, and (f) laser beam-sample distance on grating periodicity. (g) The effect of changing energy on grating bar width. Microscopy images of 25nm Au sample produced with (h) energy of 90mJ and periodicity of 1.4μm and with (i) energy of 330mJ and periodicity of 1.3 μm. (j) The effect of altering number of pulses on grating periodicity. Optical microscopy images of grating made with 330mJ energy at (k) 3 and (l) 4 Hz. (scale bar = 5 μm)

2D periodic Au nanostructures were also fabricated by exposing the recording medium to multiple beam pulses. After the first exposure (1D grating formation), the sample was rotated 90° (Figure 3.1) and subsequently exposed to laser light to produce 2D grating periodicity. By

varying the rotation/tilt angles, structures with square and rectangular (parallelogram) arrays were produced. Figure 3.4 illustrates the fabricated structures in 25-40 nm thick Au films. Figure 3.4a shows 25 nm 2D pattern of square arrays (90° rotation) with dimension of each square near 640 nm × 640 nm produced at a tilt angle of 30° and figure 2.4b produced at different parameters. This smallest feature size and grating distance was achieved by optimizing the three parameters [3, 130]. Figures 3.4c and 3.4d show a 40 nm thick array of squares (2.98 µm × 3.04 µm) and rectangles (5.8 µm × 950nm).

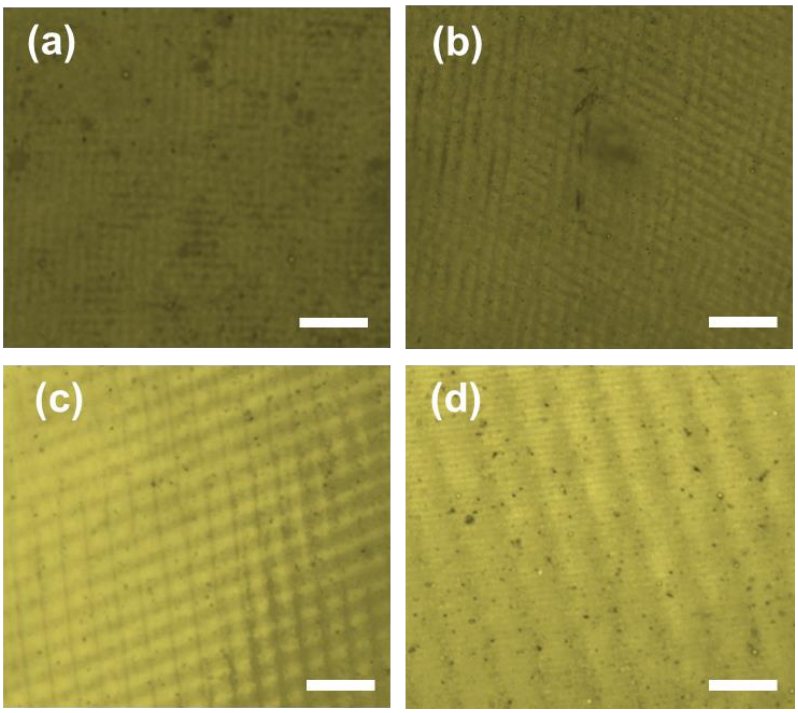

Figure 3.4: 2D Au square arrays fabricated by holographic DLIP. Arrays of 25 nm thick (a) squares (640 nm × 640 nm) and (b) parallelograms (2.4 µm × 1.8 µm). Arrays of 40 nm thick (c) elongated squares (2.98 µm × 3.04 µm) and (d) parallelograms (5.8 µm × 950 nm). (scale bar = 10 µm)

3.4.4-Optical characterization of the gratings

The diffraction of light from 2D arrays was analyzed by normally illuminating the periodic samples with a red laser beam (λ = 650 nm) and observing the transmitted light on a perpendicular flat screen. Upon illumination with laser light, the square pattern (640 nm × 640

nm) produced a diffraction pattern consisting of four first order spots, with a distribution along the horizontal and vertical axes (Figure 3.5a). The angular distribution of the spots was measured to be ~40° with respect to the undiffracted light source (zero order in the centre). The optical measurements of diffraction were consistent with four spots locations on horizontal and vertical axes. Gratings having small periodicities resulted in first order diffraction only and large diffraction angles on both axes. The diffraction from a rectangular (parallelogram like) array (2.4 µm × 1.8 µm) produced horizontal axis spots at 10° and 24° for first and second orders, while vertical axis spots were at 23° and 39° for the first and second orders, respectively (Figure 3.5b).

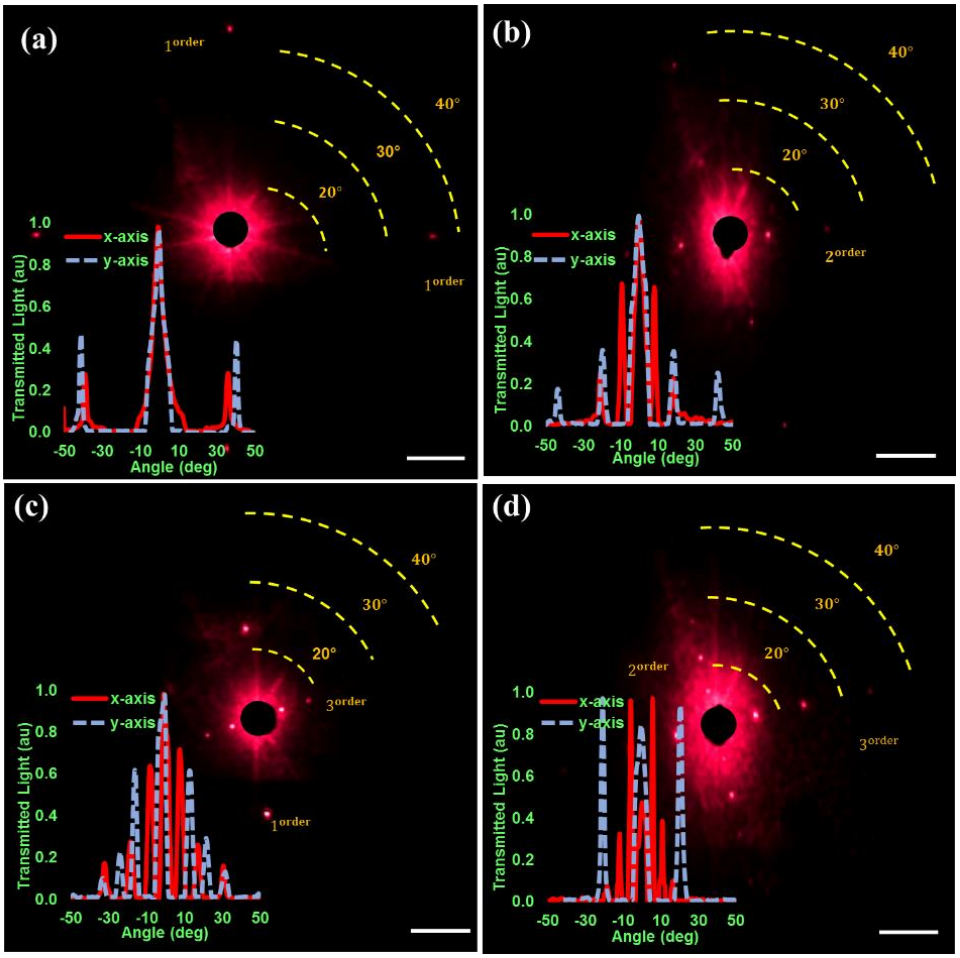

Figure 3.5: Diffraction of monochromatic light λ = 650 nm from 2D nanopattern arrays. Light diffraction from (a) squares (640 nm × 640 nm), (b) rectangles (2.4 µm × 1.8 µm) (c) rectangles (parallelograms) (5.8 µm × 950 nm)), and (d) squares (2.98 µm × 3.04 µm),. Angle-resolved measurements of diffraction intensity for the diffraction patterns shown in (a-d) respectively. (scale bar = 10 µm)

An increase in the array periodicity size decreases the diffraction spot angles; however, it was also associated with an increase in the number of diffraction orders (Figure 3.5c-d). The diffraction patterns produced for the elongated square (2.98 µm × 3.04 µm) array sample showed three orders (10°, 23°, and 33° horizontally; and at 9°, 20°, and 27° vertically) along each axis. Finally, the interesting results for rectangles (parallelograms) (5.8 µm × 950 nm) in Figure 3.5d show that by having none uniform periodicities (in the two axis) customised diffractions can be produced. The results also show that change in the recording medium thickness is a crucial factor for the required diffraction efficiency of optical applications. As the Au thickness of patterns increased from 25 nm (Figure 3.5a-b) to 40 nm (Figure 3.5c-d), the intensity of the light diffraction spots also increased[130]. Therefore, both the grating spacing and the thickness of the material influenced the characteristics of light diffraction.

Angle-resolved measurements were used to analyze the diffraction efficiency of 2D gratings using a halogen light source (Ocean Optics HL-2000). The transmission from the square and rectangular 2D structures generated four visible rainbow patterns. These 25 nm thick Au patterns were analysed in the horizontal and vertical axes. The optical light intensity measurements were conducted on each sample perpendicularly placed 13.5 cm away from the light source. The light diffraction from the 2D samples was spectroscopically analyzed using a motorized rotation stage (Figure 3.6a). The stage rotated from -90° to 90° with 1° step increments. This measurement was repeated for each axis to record the distribution of the rainbow diffraction pattern.

Figure 3.6b shows angle-resolved measurements of rectangular arrays from 6.5° to 10° from the normal within a spectral range from 450 to 900 nm. The rectangular structure diffracted light at wide bandwidths of 450 nm and 400 nm on horizontal and vertical axes, respectively (Figure 2.6b-c).

Figure 3.6c shows the vertical axis wavelength spectrum, covering a range from 8.5° to 13.5°. The transmitted light intensity distribution of diffracted light through a square grating in both axes is less than elongated-rectangular arrays. Figure 2.6d shows the diffraction of light through a square array measured from 29° to 41°. The highest transmitted light intensity in the x axis (~3900 au) was from 580 nm to 640 nm. However, in vertical axis shown in Figure 2.6e, the wavelength range was from 470 nm to 740 nm from 29.5° to 39.5°. The maximum light intensity of the vertical axis was ~2600 au. The transmitted light intensity for the square array was ~3900 au and ~2600 au on the horizontal and vertical axes, respectively. The square pattern bandwidth was 300 nm on the horizontal axis and 260 nm on the vertical axis.

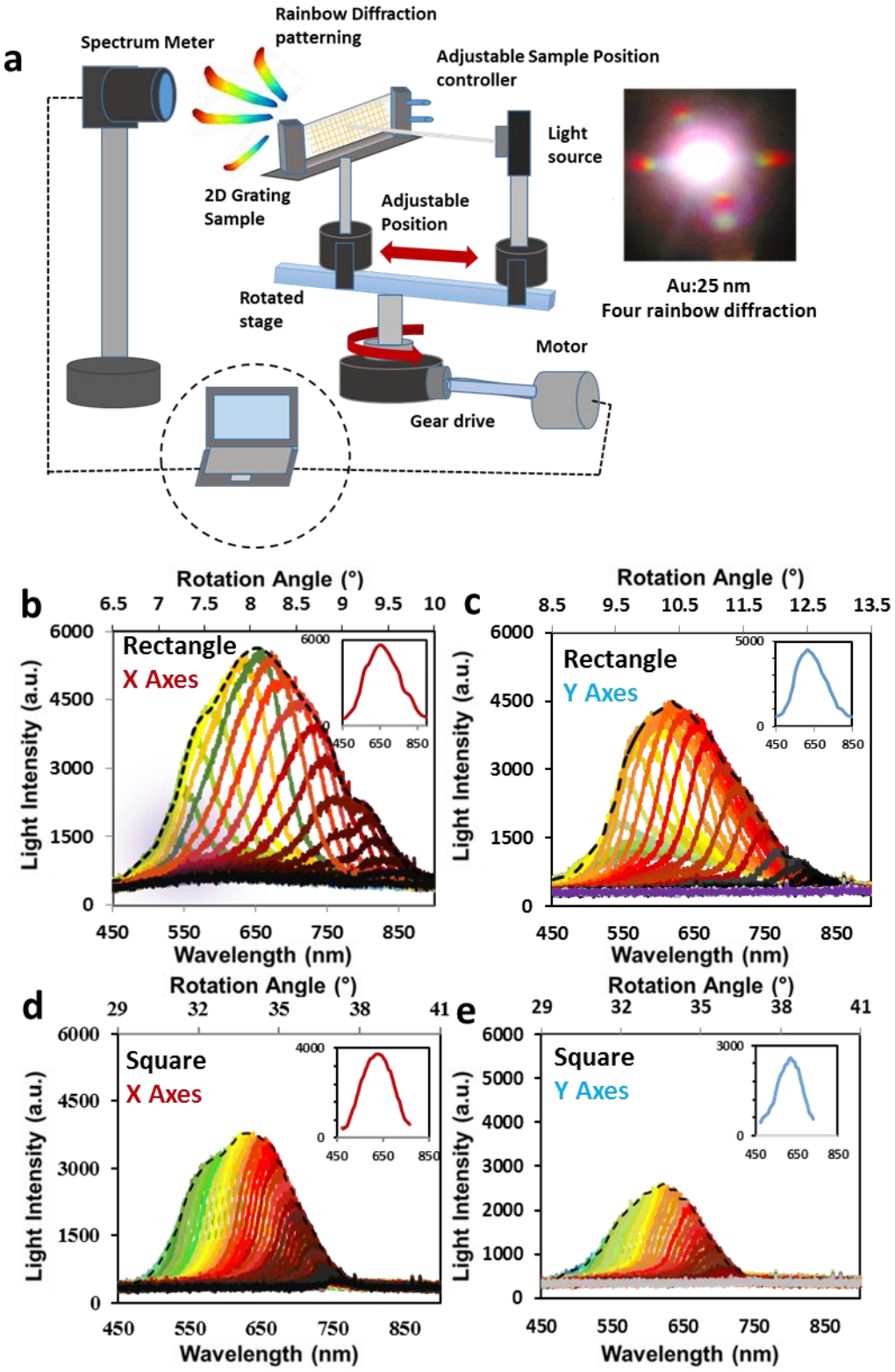

Figure 3.6: Angle-resolved measurements of the diffraction pettering fabricated *via* holographic DLIP. (a) The spectroscopy system contains a white light beam that passes through a 2D metal film sample on a motorized stage. (b) Transmission spectra of 25 nm thick elongated-rectangular array (2.4 µm × 1.8 µm) x axis and (c) y axis. Transmission spectra of square array (640 nm × 640 nm) (d) x axis and (e) y axis.

3.5-Conclusion

Holographic DLIP has many advantages which allow substantial improvement in the production process, offering low cost, fabrication flexibility and simple setup as compared to other nanofabrication strategies. The present holographic DLIP strategy can generate 1D gratings with single pulse (nanosecond range) and create 2D patterns by multiple pulses to achieve highly controllable nanoscale arrays. Grating spacing was controlled by varying the tilt angle with respect to the object surface plane. In addition, adjusting the distances between the laser-source-mirror also enhanced the control over the grating periodicities. The three parameters controlling the structure spacing (Λ) are optimized and it is a repeatable process. Controlling these parameters allowed the creation of accurate 2D holographic nanostructures. The fabricated Au structures were 2D square and rectangular arrays having thicknesses of 25 nm and 40 nm. Angular-resolved measurements were used to investigate the diffraction characteristics of the 2D gratings produced. Increase in the grating distance also increased the number of visible diffraction orders. A variety of grating shapes, periodicities and the tailored optical effects were rationally designed and characterized. Additionally, the diffracted light efficiency was observed to increase with the Au film thicknesses. The fabricated 1/2D holographic arrays could have applications in biosensors, security devices, and printable optical devices.

Chapter 4: LASER NANOPATTERNING OF COLORED INK THIN FILMS FOR PHOTONIC DEVICES

This chapter is based on a published Journal Paper, published online

AlQattan B. [(1)], Benton D. [(2)], Yetisen A. K. [(3),] Butt H. [(1)]: Laser Nanopatterning of Colored Ink Thin Films for Photonic Devices. ACS Applied Materials & Interfaces, 2017, 9 (45), 39641–39649)

[(1)] Nanotechnology Laboratory, School of Engineering, University of Birmingham, Birmingham B15 2TT, UK.
[(2)] Aston Institute of Photonics Technologies, Aston University, Birmingham, B4 7ET, UK
[(3)]Harvard-MIT Division of Health Sciences and Technology, Massachusetts Institute of Technology, Cambridge, MA 02139, USA

Author contributions: Bader AlQattan is the main author of the work and he conceived the idea of producing a 1D nanostructure on four coloured dyes. He designed the experiments, executed all necessary optical characterization, carried out data analysis, and wrote the manuscript. The rest of the co-authors Dr David Benton, Dr Ali K. Yetisen, and the principal supervisor, Dr Haider Butt reviewed and edited the manuscript.

4.1-Abstract

Different synthetic dye-based inks consisting of four ink colours (black, red, blue, and brown), which have different absorption light profiles, were used to fabricate nanostructures with a holographic ablation based on direct laser interference patterning. Several lasers beams will be made to interfere with one another to produce interference patterns containing nanoscale fringes to create high and low intensity regions. A laser in holographic Denisyuk reflection mode was used on thick films of material (ink) to make interference fringes' gratings structures. All the ink-based dyes have the same nano-spacing structure, but they have different responses to light.

4.2-Introduction

Nanofabrication techniques such as electron beam lithography (e-beam) or Focused Ion Beam (FIB) milling can produce meticulous nanostructures with 2-5 nm resolution [28]. However, they require high-power energy supplies, have long production times, and involve complex setups and equipment [131-134]. In addition, they are not amenable for a variety of materials which can be directly processed [49]. Coloration of different nanomaterials as metasurfaces is highly desirable to produce multifunctional and miniaturized optoelectronic devices. These devices may comprise metallic nanostructures with high polarization-independent reflection, strong contrast, fast response time, and long-term stability. In addition they may have controllable optical absorption of a nanostructured polymer film to diffract light[135]. However, these devices require layers with specific arrangement as short-range ordered nanoholes in a gold film, which affect the total cost and time, and these devices can be only

used in reflection mode [84, 136]. Nanoparticle (NP) assemblies can also be used to create functional optical/electrical devices for sensing, electronics, displays, and catalysis. Sophisticated design patterns, high intensity and wide angle-independent structural colors are the key features of the NP-based optical devices. Ejecting ink from the nozzle, wetting, and sputtering, spreading, and retracing processes can affect the precisions of the final structure of the printed nanostructures [77, 137]. The localized surface plasmon resonance of silver nanoplate (SNP) substrates can be tuned from 500 to 800 nm in the visible spectrum. These devices have selective optical absorption and scattering behaviour based of specific nanoparticle sizes. However, they required complex chemical syntheses processes. Moreover, the colours of silver films lead to strong electromagnetic scattering [138]. Cubic liquid-crystal structures have been developed for electronic and photonic applications [139]. Many advanced reflective photonic applications could be achieved based on the patterned crystallographic orientation of the cubic soft lattice of a blue phase liquid crystal (BPLC). The BPLC could be produced with UV irradiation and photomask which are complex and high cost [139, 140]. In addition photolithograph has been widely used to make various nanostructures for optical devices operating in the visible region [141, 142]. However, using pulsed laser ablation required low energy and rapid production [143, 144]. Recently, direct laser interference patterning (DLIP) has been used to produce nanostructures in thin materials. Such nanostructures can be patterned into 1/2/3D geometries [48, 50, 51, 145], and complex patterns such as Fresnel lenses and filters [48, 49, 145]. The expansion of this platform to a wide range of low-cost materials is highly desirable for large-scale production.

Here, a holographic ablation based on a direct laser interference patterning method rapidly produced low-cost optical nanostructures. A Nd:YAG laser (532 nm) was used in holographic Denisyuk reflection mode to create ablative interference fringes [48, 51]. The laser wavelength

of 532 nm was selected because its abortion is better for the target material. It was utilized on different synthetic dye-based inks, which have different optical properties, to produce 1D photonic nanostructures. Tested ink media consisted of four ink colours (black, red, blue, and brown). Holographic DLIP allowed forming constructive antinode fringes of electromagnetic field from the standing wave to create gratings in dye-based inks. Using thick film of material (ink) causes multiple laser wave interference fringes to form the gratings. A thick amplitude grating invariably describes an absorption grating. Usually a thick holographic grating can be expressed as a sinusoidal absorption grating and it has different characteristics of diffraction compared to conventional gratings with sharp edges. This is because the shape and the thickness of the recording medium influences the transmission profile [146, 147]. Such dye-based ink gratings can be used in a myriad of devices to produce light deflection, guidance, or coupling. In the present work, the nanostructures based on the four dye-based ink gratings have been spectrally analyzed and angle-resolved measurements were performed to characterize their optical properties. This is the first demonstration of laser based nanopatterning of multiple ink formulations and their usage for wavelength dependent optical devices. The work demonstrates the possibility of nanopatterning organic and florescent materials which cannot be processed through methods such as photolithography and electron beam lithography.

4.3-Materials and methods

4.3.1-Preparation of the ink recording media

Black, red, blue and brown ink colours (Staedtler Lumocolor) have refractive indexes of 1.6, 1.65, 1.59 and 1.62 respectively. Diluted ink solutions (1:8, v/v in ethanol) were spin coated on 1-mm thick glass slides at 200 rpm for 35 s. The inks used were permanent and had a long-term

durability. The glass slide has refractive indexes of 1.5 and it contributed to the total refractive indexes of each ink colour.

4.3.2-Fabrication of the diffraction gratings in ink

Holographic direct laser interference patterning was used in Denisyuk reflection mode. Laser beams (λ=532 nm) initially directed by a mirror travelled to an ink-based recording medium and reflected from a plane mirror to ablate the localized regions of the medium. The exposure angle of all ink films was set to 18° from the surface plane of the plane mirror (object).

4.3.3-Spectroscopic measurements of the ink gratings

The diffraction of light from 1D gratings of the four inks (black, red, blue and brown) were analyzed by normally illuminating the periodic samples with violet (λ = 405 nm), green (λ = 532 nm), and red (λ = 635 nm) laser beams and observing the transmitted light perpendicularly on a flat screen, placed 17 cm away.

4.3.4-Angle-resolved measurements of the gratings

A halogen light source (HL-2000, Ocean Optics) and a goniometer setup were used to carry out angle-resolved measurements of the diffraction efficiency of the ink gratings. Diffraction spots from the ink nanostructures were analyzed in transmission mode. Each sample was placed 17 cm away from the optical probe to analyse the diffraction wavelengths. A motorized rotating stage was used for broadband spectroscopic analysis of the rainbow diffraction through the nanostructure gratings. The rotation stage had 0.5° steps from ranging from -90° to +90°.

4.4-Results and discussion

4.4.1-Holographic fabrication of 1D nanostructures

Figure 4.1a shows the diagram of the hologram recording setup in Denisyuk ablation mode. The laser beams initially directed by a mirror travelled to an ink-based recording medium and reflected from a plane mirror to ablate the localized regions of the medium. To form the gratings, four dye media were used: black ink (a combination of blue, red, and yellow dyes) (Figure 4.1b), red ink (Figure 4.1c), blue ink (Figure 4.1d), and brown ink (a combination of green, yellow, and red dyes) (Figure 4.1e).

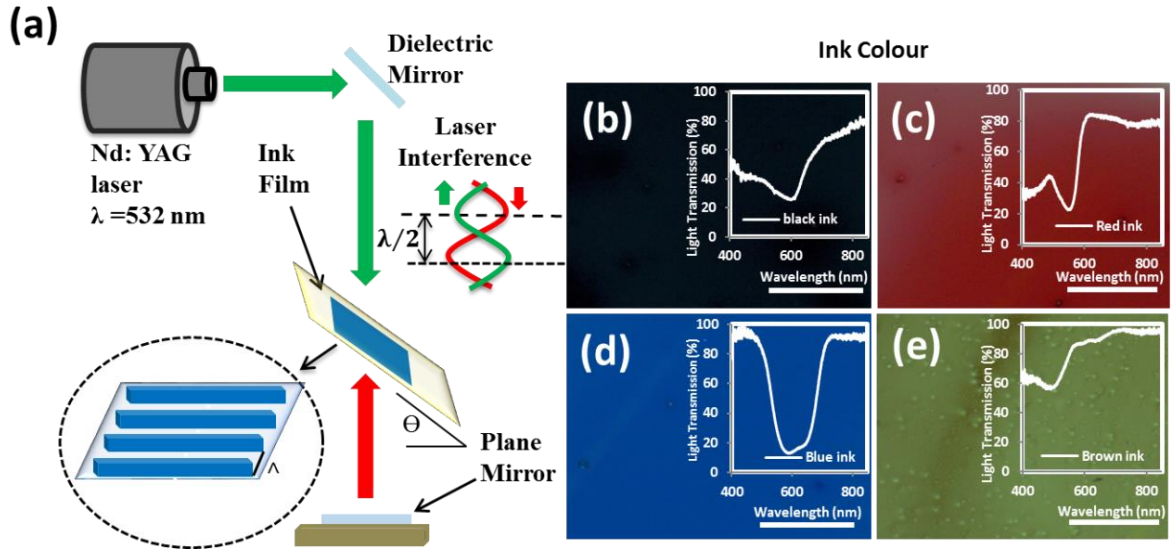

Figure 4.1: Fabrication of 1D patterns through nanosecond DLIP in holographic Denisyuk reflection mode.(a) Nd:YAG laser beam (532 nm, 3.5 ns) was directed to a dielectric mirror and passed through a dye-based ink medium and reflected back from a plane mirror to ablate a localized region of the recording medium. Four dye-based ink mediums are (b) black, (c) red, (d) blue, and (e) brown. The light transmission measurement for each medium added on each colour. (scale bar = 200 μm)

A halogen light source was used to analyze the transmission of each ink-based recording medium (insets in Figure 4.1). The transmitted halogen light generated the visible range

wavelengths from 380 nm to 740 nm. For thick materials, the recording media could be described in terms of light absorption percentage (Absorption %= 1-Transmission %). The black ink had the most absorption of light in the visible range, absorbing more than 75% of all wavelengths (Figure 4.1b). The red ink had low absorption (20-45%) of light in the visible range and it allowed 80% light transmission over 620 nm wavelengths (Figure 4.1c). On the other hand, the blue ink has shown high light transmission below 500 nm and above 700 nm (Figure 4.1d). Brown ink consisted of different dye compositions, showing high light transmission at all wavelengths. As a result, red and blue inks had sharp absorption dips in the visible spectrum; however, the black and brown inks were highly absorbent in the visible spectrum since they were composed of many colours.

Holographic DLIP was performed to produce a well-ordered grating in each ink medium, where the size of the grating pattern ranged from 0.2~1.0 cm in diameter (roughly the size of laser beam). The four ink media received the same laser beam energy (210 mJ) and they produced the same 1D nanostructures. The red ink had low peak absorption at 532 nm so it produced the smallest spot size (0.25 cm). The black ink had the largest laser spot size as compared to the other inks due to its high light absorption and ablation within the green region of the spectrum (Figure 4.2a). The laser ablation process was the result of the laser interference of two beams, which can be described by:

$$E_I = E_{01}\, sin(kx + \omega t + \varepsilon_I) \quad \text{(Eq. 4.1)}$$

$$E_R = E_{0R}\, sin(kx + \omega t + \varepsilon_R) \quad \text{(Eq. 4.2)}$$

$$E = E_I + E_R \quad \text{(Eq. 4.3)}$$

where E_I is the incident laser wave and E_R is the reflected laser wave from the plane mirror, k is the propagation number or the magnitude of grating vector and $k=2\pi/\lambda$, and x, ω, t, Λ, λ represent axis plane, angular velocity, time, grating spacing, and wavelength, respectively. The initial phase or angle is sampled as ε. The other countenance of symbols shows the resultant wave E of initial and reflection waves [61, 148].

$$I=I_o \cos\left(\frac{2\pi\Lambda}{\lambda}\right) \quad \text{(Eq. 4.4)}$$

$$\Lambda = \frac{\lambda}{2\sin(\Theta)} \quad \text{(Eq. 4.5)}$$

The grating structure was created as a result of the intensity (I) of laser interference, where (I_o) is the maximum laser interference intensity (Eq. 4.4). The exposure angle of all ink films was 18° from the surface plane of the plane mirror (object) so the four inks had the same grating spacing of 840 nm. The difference between the experimental results of grating spacing and the analytical solution was 2% (Eq. 4.5). The period of grating spacing can be controlled by the exposure angle (Θ) between the laser beam and the tilt angle from the surface plane of the mirror (Eq. 4.5) [51, 61].

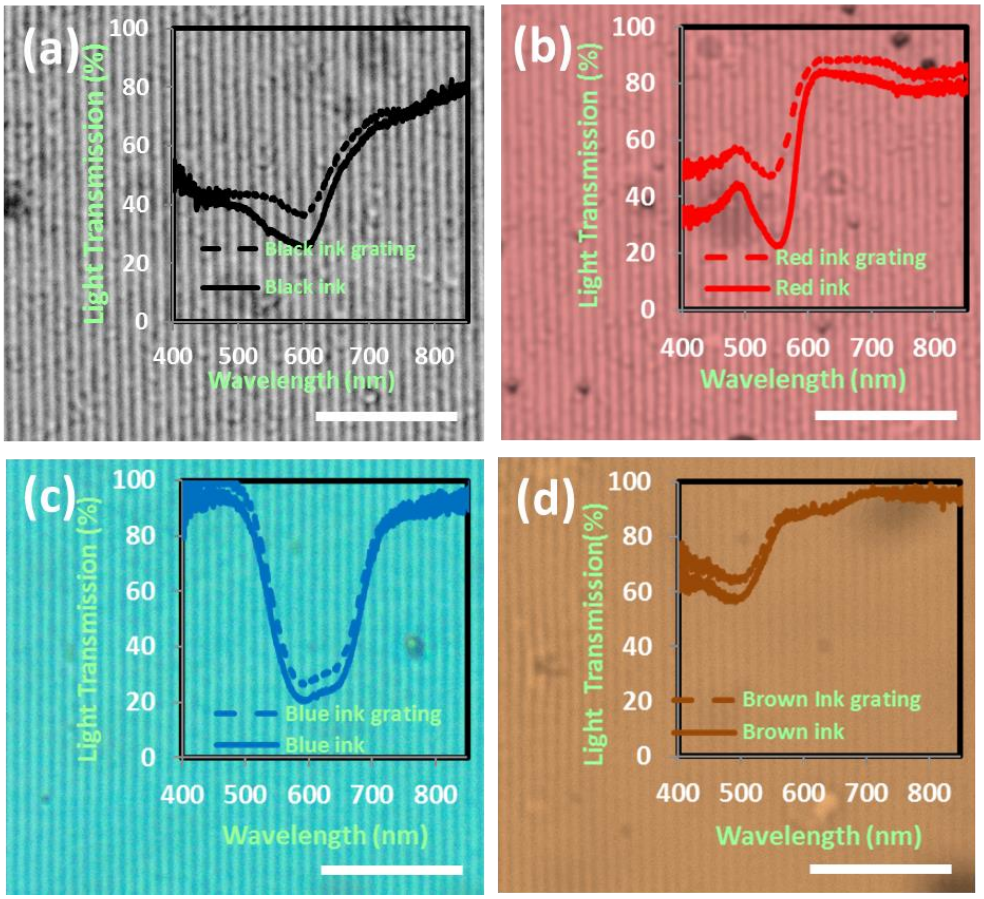

Figure 4.2: Optical microscopy images of 1D surface grating nanostructures fabricated on 915 nm thickness dyes by holographic DLIP. Gratings having periodicities of 840 nm in (a) black, (b) red, (c) blue, and (d) brown inks. The light transmission graphs of each ink were integrated for normalization. (scale bar = 10 μm.)

The formation of gratings on the four coloured inks has increased the broadband light transmission. The average transmission ranges between 3-20% (Figure 4.2a-d). The highest percentage of transmission change was in the red ink while the lowest one was in the brown ink, whereas the transmission increased by 8% and 10% for blue and black inks, respectively (Figure 4.2). In general, transmission of light changed in all the ink media operating between 400-650 nm except for red ink which remained in the entire visible spectrum. The highest absorption zone of the red ink was at 559 nm, close to the laser beam wavelength of 532 nm. SEM images show magnified images for the nanostructures of black and blue gratings (Figure 4.3a-b).

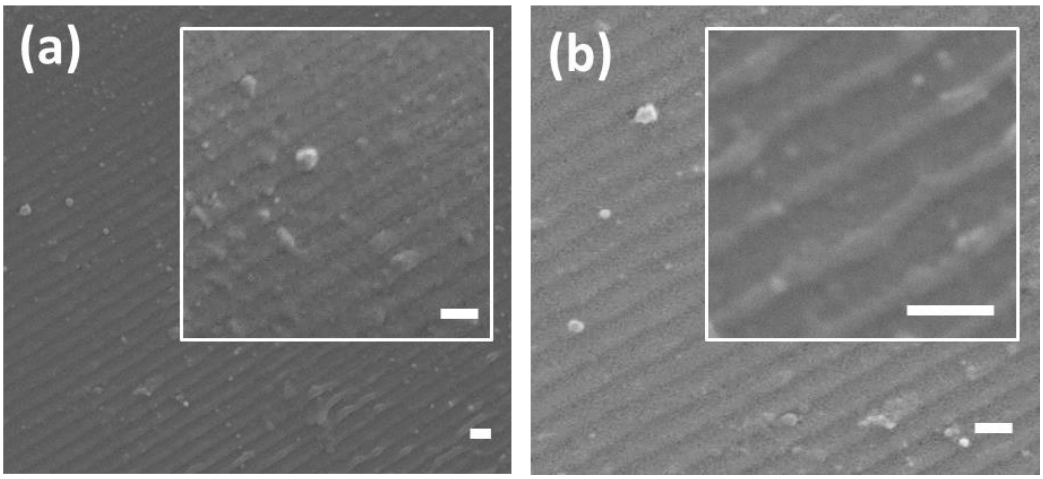

Figure 4.3:SEM grating image of (a) black, (b) blue gratings. The light transmission graphs of each ink were integrated for normalization. (SEM scale bar=1 μm)

4.4.2-Optical characterization of the gratings

The created nanostructures were amplitude gratings. However, different absorption regions of the ink produced different diffraction responses. Although the standing wave field had the same source wavelength, different dye inks formed different diffraction patterns. The black grating had the same spacing as the other inks but it has different diffraction responses when illuminated with different laser beams (Figure 4.4). The black ink based grating has generated additional diffraction spots [149]. The violet laser beam illumination (405 nm) of the grating resulted in diffraction of the first order at 27° and the second order at 73°, which agreed with the theoretical diffraction spots (Eq. 4.6). In addition, the secondary wave diffracted two more spots (Figure 4.4a). The laser beam (532 nm) produced diffraction of the first order at 39°, which was similar to the theoretical diffraction angle while the secondary wave created two additional spots at 18^{o} and 63^{o} (Figure 4.4b). Additionally, the red laser beam (635 nm) resulted in the diffraction of light at 47° with 2° difference as compared to the theoretical diffraction value and the secondary wave diffraction was at 24° (Figure 4.4c). The additional

diffraction spots resulted from the high absorption of black ink and subsequent secondary standing wave. The black dye-based ink received one of the standing beam stronger (532 nm) than the other (1064 nm). The two wavelength could electromagnetically induce diffraction intensity based on the thickness and the medium of the grating [149, 150]. Although the black ink generated additional diffraction spots from the secondary standing wave, another experiment has been conducted on black ink with Nd:YAG laser beam 1064 nm and there was no sign of secondary grating diffraction (Appendix, Figure. 4S.9).

$$\Lambda = \frac{\lambda m}{sin(\alpha)} \qquad \text{(Eq. 4.6)}$$

The red and brown inks showed resemblance in the diffraction of the first order (Figure 3.3e-f, k-l). However, there was a slight change in the (405 nm) laser diffraction of the second order from the two ink gratings (Figure 4.4d-j). The red ink has generated diffraction at 68° and the brown ink diffraction was at 71° due to the change reflective index of each colour (Eq. 4.7-9). In addition, there were no signs of secondary grating diffraction because both inks gratings had low absorption profiles to produce a secondary grating (Figure 4.2b-d). Furthermore, the blue ink had slight differences on the diffraction points with an additional weak diffraction spot when illuminated with a 532 nm laser beam (Figure 4.4g-i).

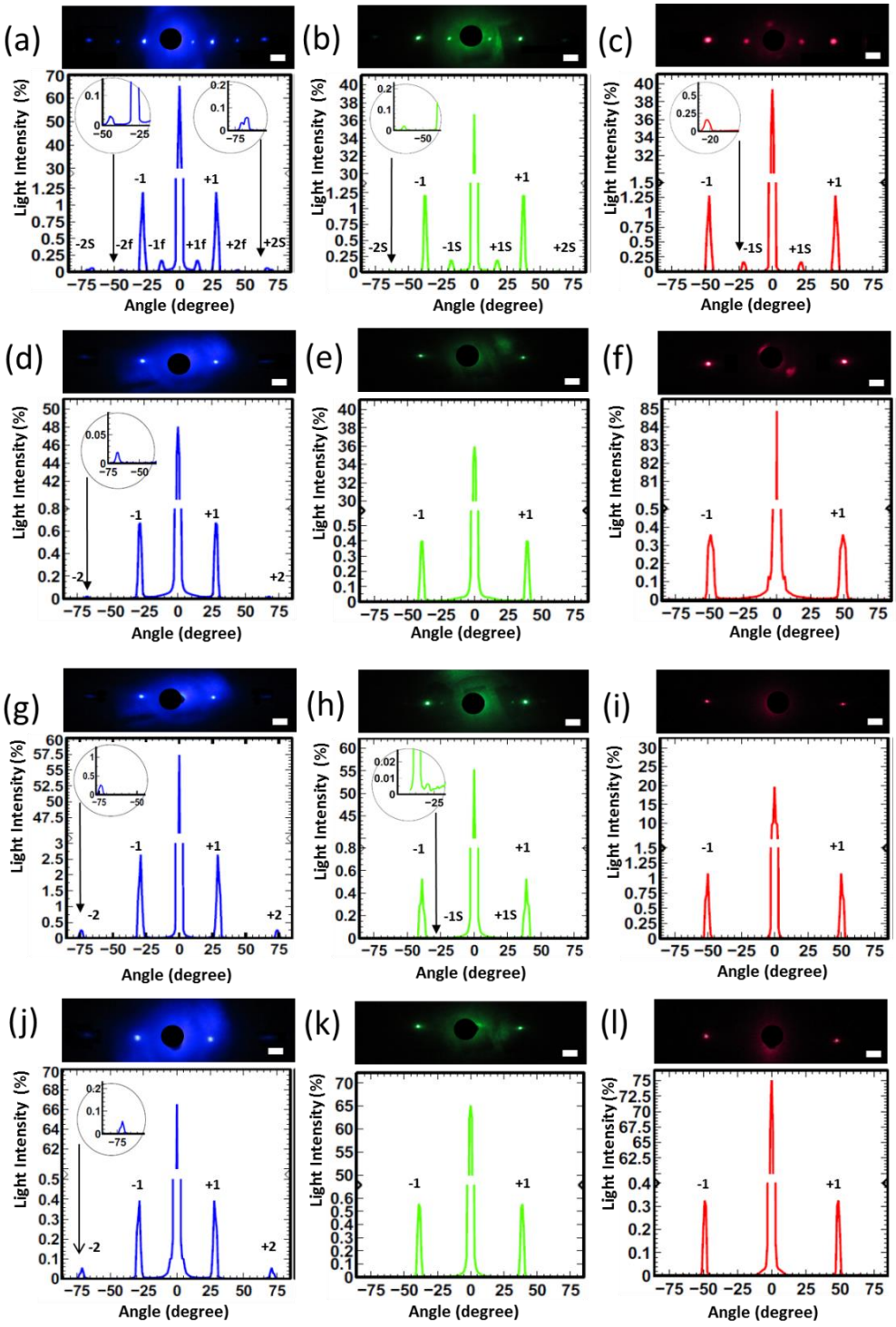

Figure 4.4: Diffraction from nanostructures upon illumination from three onochromatic light sources (405 nm, 532 nm and 635 nm) on patterned ink gratings (Λ = 840 nm) (a-c) Black, (d-f) red, (g-i) blue, and (j-l) brown inks.(scale bar=5 cm)

In addition, most of the absorption range was within 560-650 nm, which should allow more diffraction intensity for a 635 nm laser beam (Figure 4.4i). However, the primary diffraction spot locations of the three laser beams on the blue ink grating closely matched with the

calculated theoretical values (Table 4.1). As a result, the longer wavelength of laser light diffracted through a larger angle than the shorter wavelength laser light. In addition, the diffractions from the three lasers did not have identical positions even though the spacing of the gratings for the four inks were the same. This is because they have different refractive index of thick material. The experiment has been repeated multiple times on four different samples using the four colours and the results showed that the material colour has influenced the diffraction. The diffraction angle (α) of each order (m) and can be theoretically estimated by (Eq. 4.6).

Table 4.1: Diffraction from ink based gratings using three laser beams (405 nm, 532 nm, 635 nm) and comparison with the theoretical values. C: Colour, L: Laser, Exp S: Experimental secondary laser, Exp P: Experimental primary laser, Ther.: Theoretical values calculated with Eq. 4.6.

Ink-C.	L.(nm)	Exp. S(1)	Exp. P (1)	Ther. (1)	Exp.S(2)	Exp.P(2)	Ther.(2)
Black	405	13^o	28^o	28.8^o	44^o	73.2^o	74.6^o
Black	532	18^o	39^o	39.3^o	63^o	-	-
Black	635	22^o	47^o	49.1^o	-	-	-
Red	405	-	28^o	28.8^o	-	68^o	74.6^o
Red	532	-	39^o	39.3^o	-	-	-
Red	635	-	49^o	49.1^o	-	-	
Blue	405	-	29^o	28.8^o	-	74^o	74.6^o
Blue	532	32^o	39^o	39.3^o	-	-	-
Blue	635	-	50^o	49.1^o	-	-	-
Brown	405	-	28^o	28.8^o	-	71^o	74.6^o
Brown	532	-	39^o	39.3^o	-	-	-
Brown	635	-	49^o	49.1^o	-	-	-

Variation in monochromatic light wavelengths to illuminate ink gratings changed diffraction efficiency. The diffraction efficiency (I_{eff}) of each ink grating was considered from the relation of the intensity of first order I_1 and the zero-order intensity I_0 and ($I_{eff} = I_1/I_0$). The black ink had three equal monochromatic diffraction spots of the first order because of its absorption behavior of the broad wavelengths. However, the diffraction efficiencies of the three laser beams were not the same because some of the ink-based gratings had different light

transmissions at zero-order (Figure 4.5a). The light diffraction efficiency of the red ink at 635 nm was the lowest because most light transmitted in the zero-order as the same wave colour (Figure 4.5b). On the other hand, this was not the case for the blue ink. The light at 405 nm had high diffraction efficiency due to the two waves (primary and secondary) creating a higher sinusoidal absorption grating with small waves to produce a phase grating diffraction in the same position of the first order(Figure 4.5c) [146, 149]. The brown ink light diffraction efficiency was the lowest because it had low light absorption (Figure 4.5d). The ink thickness had an important role on light diffraction based on absorption parameter (Q') and refractive index effect can be calculated as:

$$Q'=2\pi\lambda h_c/n_o\Lambda^2 \cos\theta \quad \text{(Eq. 4.7)}$$

$$m=2\pi n_o \Lambda \sin\theta/\lambda \quad \text{(Eq. 4.8)}$$

$$h_c=\lambda/2n_o \quad \text{(Eq. 4.9)}$$

where h_c is the grating thickness, and n_o is the refractive index of the grating vector [146, 151]. Black ink was selected to test the effect of the thickness because it had equal transmission for three monochromatic laser lights. The laser light (635 nm) was used to test the transmission profile of different thicknesses.

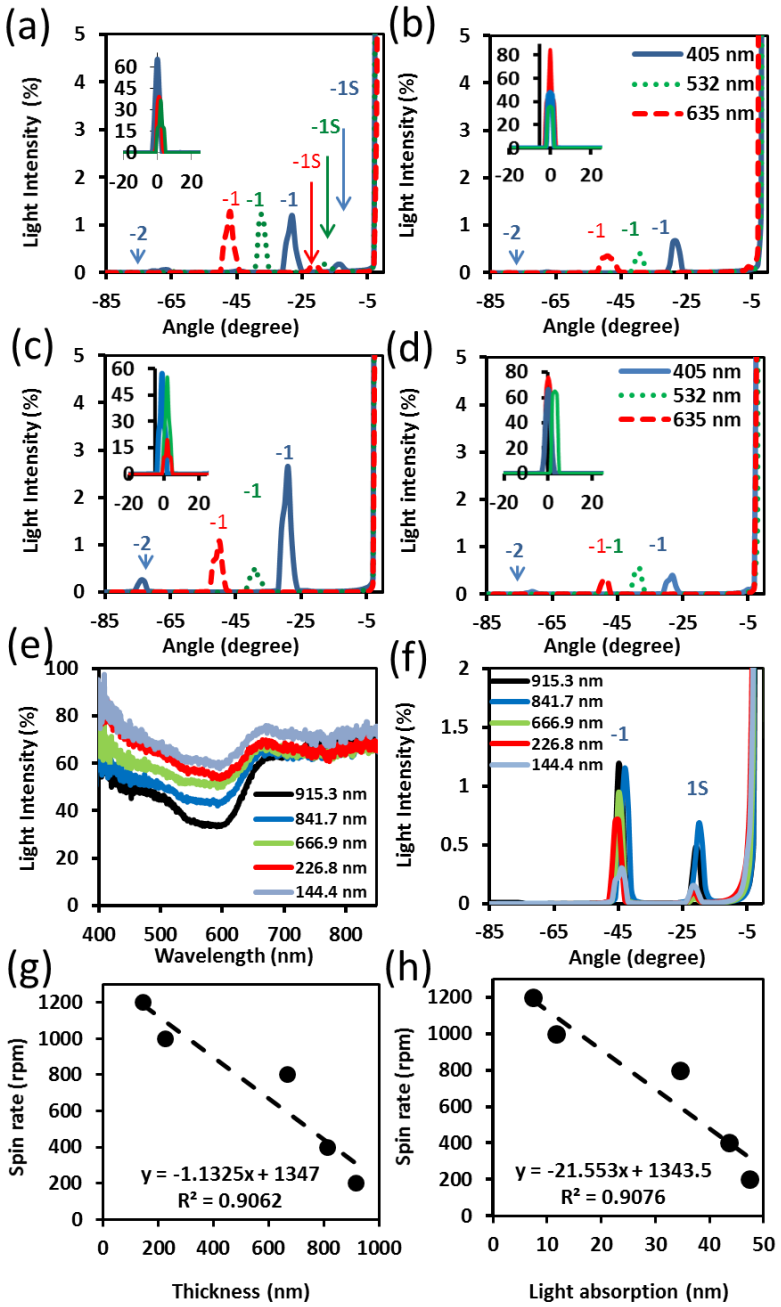

Figure 4.5: Diffraction intensity of the zero and first order from three monochromatic lights (405 nm, 532 nm and 635 nm) on four patterned ink gratings: (a) black; (b) red; (c) blue; (d) brown ink gratings; black ink gratings at different thicknesses in (e) transmission; (f) diffraction modes spin-coating effect; (g) thickness; (h) light absorption.

The black ink was spin-coated on 1 mm thick glasses at a speed of (200-1200 rpm). The transmission decreased with lower spin-coating speed and higher thickness (Figure 4.5e). Additionally, the diffraction intensity of first order increased with increasing thickness of the ink layer (Figure 4.5f). However, the secondary grating diffractions did not follow the first

order trend and showed different responses in diffraction intensity. The first order diffraction is commonly used in optical applications because it has the highest efficiency, and in the present analysis, it can be the primary evaluation parameter. The thickness of the ink medium was being controlled by the spin-coating speed (Figure 4.5g). In addition, the ink layer thickness had a significant effect in light absorption (Figure 4.5h). As a result, increasing the ink thickness reduced the transmission, which enhanced the diffraction efficiency. The refractive index and absorption parameters at different thicknesses were calculated by (Equation 4.7-9); and therefore, 915 nm thickness was chosen as the best medium thickness for the subsequent experiments. Using laser interference in Denisyuk reflection mode, the material thickness must be reasonable to allow the laser waves to pass through any substrate to produce the ablative reflection waves. If the material does not transmit the laser waves, the medium would burn it or not respond. In addition, if the absorption reaches zero or 100% transmission, the target material would not interact with the laser wave. This material can be considered as being of a reasonable thickness, because some materials, such as Au, did not respond with the laser pulse in the reflection mode system if the thickness exceeded 40 nm (Chapter 3) [51, 122]. For these reasons, the ink thickness was sufficient (from 50% to 100%), in particular the black and blue inks.

4.4.3-Spectrum rainbow diffraction measurement

A goniometer controlled spectroscopy setup was used for angular measurements and the distribution of the rainbow diffraction pattern from each ink grating was recorded (Figure 4.6a). The angle-resolved diffraction measurements of the four ink gratings were measured at a maximum broadband light intensity to quantify the highest value of diffracted wavelength distribution. The maximization enabled to have the same bandwidth of grating diffraction

within the range of 400-850 nm. The rainbow diffraction of each ink grating had different arcs and number of orders. The length measurements were based on placing a screen at 30 cm away from diffraction samples. The black ink grating had the widest dispersion pattern as compared to the other inks, and it produced two diffraction orders with a total angular diffraction of 43° from one side of the rotation stage (0° to +90°). The total length of the two orders was 22.83 cm (Figure 4.6b-f). The red and brown ink gratings had the same total angular diffraction having a width of 19° to (10 cm long) (Figure 4.6c-g and 4.6e-i). However, the blue ink formed a different shape of the rainbow to create a thinner width at the green region with a total diffraction of 23° and 12.7 cm long (Figure 4.6d-h). The black ink generated two rainbow patterns: the first order was 17°-22° and the second order was at 21°-60° from the two laser waves (Figure 4.6f). The black ink had the highest diffraction intensity of all light waves due to high light absorption (Figure 4.56j), but 11% of light waves was diffracted at the first order (Appendix, Figure 4S.10). However, the red ink diffracted less light from the rainbow pattern because it had low light absorption (Figure 4.6g) and diffraction concentrated at the peaks at 490 nm to 625 nm based on its absorption zone (Figure 4.6). The blue ink grating had the highest diffraction value of 73% because of the light absorption between the two peaks (Figure 4.5l). Nevertheless, the lowest intensity of wavelength distribution was with the brown ink, reaching a maximum of 28% diffraction (Figure 4.6i). This is because brown medium lost most of light to transmission at the zero-order that led to a low percentage of overall light diffraction (Figure 4.6m) (Appendix, Figure S4.11). Consequently, the four ink gratings showed a different response on the rainbow diffraction pattern. The blue and red grating inks indicated that both of them were able to create single wavelength low-cost photonic structures with wavelength dependence. However, the black and brown inks were not able to generate specific wavelength filtering because both inks diffracted light in all wavelengths.

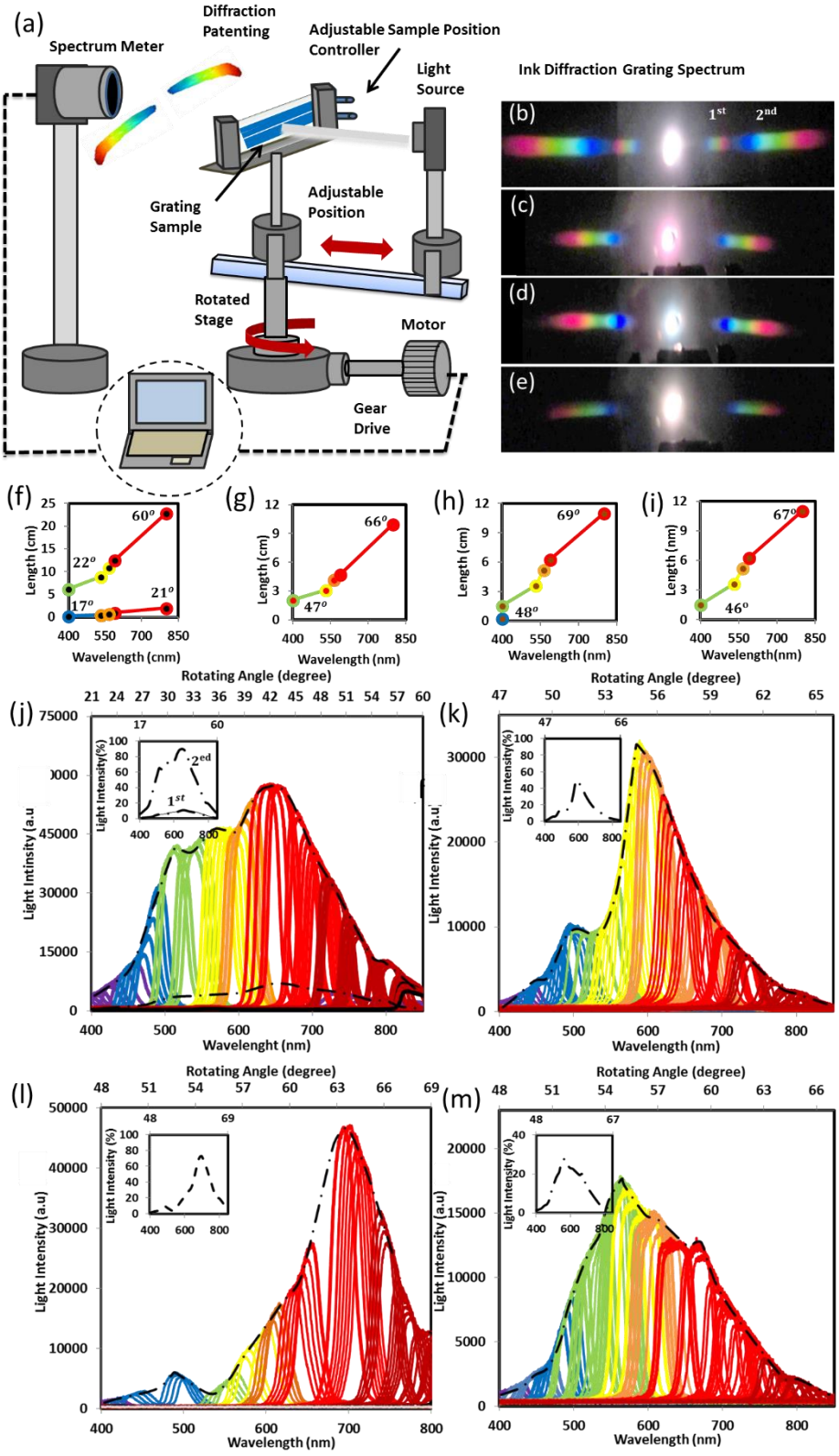

Figure 4.6: Angle-resolved measurements of the diffraction gratings fabricated *via* holographic DLIP. (a) The spectroscopy system contained the diffraction of a broadband light beam that passed through a 1D ink sample on a motorized stage to measure the rainbow pattern. The rainbow grating diffraction pattern of (b) black, (c) red, (d) blue, and (e) brown inks. Rainbow pattern length from the grating diffraction of (f) black, (g) red, (h) blue, and (i) brown light diffraction. Spectroscopy measurements of (j) black, (k) red, (l) blue, and (m) brown dye-based inks. (scale bare =5 cm)

4.5-Applications of the ink-based gratings

The dye-based inks on glass substrates could be used as low-cost wavelength filters. Their thickness of the ink layer could be controlled to adjust the percentage of light transmission and to create different photonic effects (Figure 4.7a1-4). The numbers of laser pulses were varied on the dye-based inks to filter transmission but this process ablated most of the ink medium to create ~90% of the light transmission. The laser energy and the thickness of the recording medium should be controlled to finely tune the optical properties of the wavelength filter transmission. In addition, the hydrophobicity measurements were carried out on the ink gratings with deionized water (Figure 4.7b). The nanopatterned gratings were created on the four ink types (Figure 4.7c) to show the visible effect of nanostructures and to create 1D structures (800 nm periodicity) for the hydrophobicity measurements. The hydrophobicity has increased after the nanostructure formation on the dye-based inks, but possibility of less than 10% of difference from dye ink gratings colour and instrument accuracy precision. We also demonstrate this capability by creating 1D nanostructures in blue ink (Figure 4.7d-e). In addition, there are many other optical applications that can be achieved with dye-based ink gratings. Multiple laser exposures were conducted to ablate the ink substrate in a x-y linear movement stage at 15° to produce a 1D diffraction grating in the form of a signature. A 1D grating based signature with blue ink can be used to create a high security feature (Figure 4.7f1-f2). According the manufacturer, the inks have long-term durability. In these experiments, there was no change in sample quality after a year. The image of the sample shown in (Figure 4.7f1) is one year older than the second image in (Figure 4.7f2), and they both have comparable optical performances. Moreover, a 1D diffraction grating based logo of ‘University of Birmingham’ was created by ablating black ink as examples of sophisticated design of trademark and brands for diverse commercial applications (Figure 4.7g1-g2). Their applications in optical devices include

holographic displays, data storage, filters, light trapping, security systems, and sensors [61, 143, 145, 152].

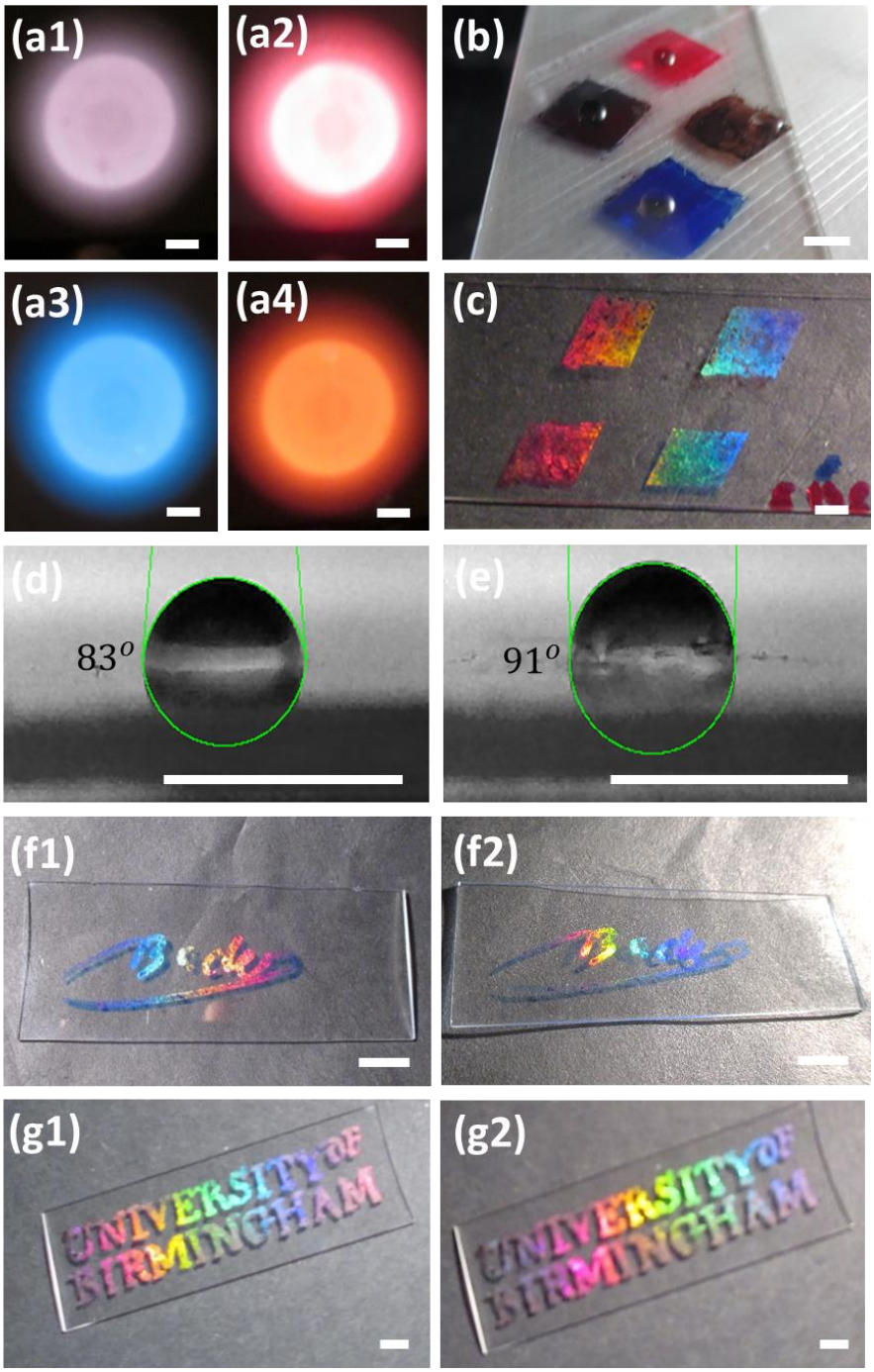

Figure 4.7: Hydrophobic properties and applications of dye-based ink gratings. (a1) black, (a2) red, (a3) blue, and (a4) brown ink wavelength filters. (b) Hydrophobicity measurements on the dye-based inks. (c) The nanopatterned gratings in array form. (d-e) hydrophobicity contact angle change. (f1-f2) Blue ink based 1D grating personal security signature. (g1-g2) Black ink-based surface grating University of Birmingham logo. (scale bar=5 mm)

4.6-Conclusions

We report the production of optical nanogratings based on economical dye-based inks. The diffraction from these gratings depended on the ink's refractive index and incident wavelength. The black ink based nanostructures displayed additional diffraction spots from its secondary grating, while the phase grating in the blue nanostructure enhanced light diffraction of the same wavelength. Moreover, with increasing ink thickness, the light diffraction is enhanced and the effective transmission is decreased. In addition, the ink based gratings can be used as a wavelength-dependent filter and their thickness can be controlled to adjust the percentage of transmission. In particular, the blue and red ink nanostructures have the potential to be used as low cost wavelength-dependent photonic structures, which have application in displays, fibre optics, and biosensors. Furthermore, hydrophobicity measurements were performed on the four ink gratings to show the increase in the contact angle due to the topology of the nanostructures. To demonstrate the utility, the blue ink based grating was demonstrated as an example of an advanced personal security signature, and a black ink grating was patterned to display 'University of Birmingham' as a distinctive logo. The DLIP patterning method described herein has wide potential applications in commercial diffraction optics.

Chapter 5: DIRECT LASER WRITING OF NANOPHOTONIC STRUCTURES ON CONTACT LENSES

This chapter is based on a published Journal Paper, published online

AlQattan B. [(1)], Yetisen A. K.[(2)], Butt H. [(1)], Direct Laser Writing of Nanophotonic Structures on Contact Lenses, ACS Nano, 2018, 12 (6), 5130–5140)

[(1)]Nanotechnology Laboratory, School of Engineering, University of Birmingham, Birmingham B15 2TT, UK.

[(2)]School of Chemical Engineering, University of Birmingham, Edgbaston, Birmingham, B15 2TT, UK

Author contributions: Bader AlQattan is the main author of the work and he perceived the idea of producing nanostructures on contact lenses. He designed the experiments, executed all necessary optical characterization, carried out data analysis and simulations, and wrote the manuscript. The rest of the co-authors Dr Ali K. Yetisen, and the principal supervisor, Dr Haider Butt reviewed and edited the manuscript.

5.1-Abstract

Economical manufacturing of nanopatterning on a regular daily-used commercial contact lens could decrease the healthcare cost. Nanostructures on contact lenses could help to detect the leading cause of some conditions of blindness. Several methods could be used, but most of them are costly and complicated. Using the black dye ink absorption with a laser in holographic Denisyuk reflection mode can generate low-cost smart contact lenses.

5.2-Introduction

Ocular diseases are associated with increasing healthcare costs involving visual acuity tests, prescriptions of eye drops, and corrective lenses, and eye surgeries. For instance, diabetic macular edema, which is the leading cause of blindness among working age adults in the United Kingdom, degrades visual acuity because of the inflammation on the central retinal thickness. This is a result of increased intraocular pressure due to damaged blood vessels in the retina, resulting in vision impairment [153]. Graves' disease is another ocular condition resulting in the overproduction of thyroid hormones (hyperthyroidism) causing eyelid lag and retraction, leading to the deterioration of eye muscles and cornea [154, 155]. Another major ocular disorder is glaucoma, with over 60.5 million patients globally, and it is estimated that this number will rise to 79.6 million by 2020[156]. Glucoma is caused by the increase of intraocular pressure due to the build-up of fluids, damaging the optic nerve leading to complete blindness in worse cases[157]. Lastly, inadequate amount of tear or oil production can cause dry eye syndrome. It may be caused by Meibomian gland dysfunction (blockage of oil glands) and/or

lacrimal gland dysfunction (LGD, aqueous tear deficiency). The dryness could lead to vision impairment, discomfort, and eventually blindness. Tear electrolytes such as Na^+ ion concentrations can be used to diagnose the dry eye severity at early stages [158]. Existing diagnoses of ocular vision diseases involves testing of visual acuity and prescribing corrective lenses [159]. However, there is a clear lack of quantitative point-of-care diagnostics to aid ophthalmologists. It is highly desirable to build a platform on existing commercial contact lenses to create functionalities such as sensing biomarkers and physical changes in the eye.

Commercial silicone-hydrogel contact lenses are widely used to correct common vision problems. They are made from a variety of hydrogel compounds with different compositions but all of them have high water content to interact with the tear film[100]. Tears have substantial diagnostic information regarding ocular diseases and they can be used as a surrogate medium for analyzing blood chemistry [158, 160]. Recently, an optical fibre sensor attached on a contact lens was developed for the quantification of tear electrolytes [161] .Various nanostructures have been fabricated within hydrogels that act as optical transducers[32]. However, integrating nanoscale features into hydrogel structures represents a fundamental challenge for producing functional contact lenses. Nanofabrication approaches to form optical structures in polymers are costly and time consuming [45, 131]. Nanostructures can be fabricated on contact lenses by contact printing [162, 163], nanoimprinting, micro transfer molding,[164] pattern replication induced by an ion field, and ultrashort laser pulse lithography. However, these fabrication approaches require multiple steps, high-energy supplies, long fabrication times, complex setups, and specialized equipment [45, 116, 131]. In addition, they are not capable of producing accurate and reproducible nanostructures on soft polymers [49, 165]. On the other hand, most laser interference systems can produce nanostructures; however, these systems may not be able to generate multiple laser pulses

without damaging the target substrate as the contact lenses are composed of hydrogel materials and can be easily damaged by high-energy laser pulses [125].

Here, a holographic laser ablation method was developed to produce optical nanostructures on commercial contact lenses. A black dye was used on the contact lens to create an interaction between the laser interference and the lens material. The dye thickness on the contact lens was estimated through a light transmission comparison of other spin-coated dye thicknesses on glass [61]. Low-cost optical nanostructures were rapidly created by direct laser interference patterning (DLIP) in holographic Denisyuk reflection mode to create ablative interference fringes on the contact lens surfaces [49, 51, 61]. One dimensional (1D) nanostructures were fabricated on the contact lenses and angle-resolved spectral measurements were performed to characterize their optical properties. In addition, 2D nanostructures were fabricated to study the light diffraction effects with monochromatic light and broadband white light. The surface wettabilities of 2D nanostructures were determined through contact angle analysis by measuring the angle between a drop of liquid and a contact lens surface. Hydrophilic properties may aid in increasing the tear distribution capability over the contact lens surfaces [166]. The hydrophobicity was measured by sessile drop technique as this method was fast and efficient to perform at static and dynamic angles [167].

5.3-Materials and methods

5.3.1-Preparation of the recording media on contact lenses

Commercial silicone-hydrogel contact lenses were used in this work (Narafilcon A, Acuvue, Johnson & Johnson). All lenses had a dioptric power of -0.5 with a base curve of 8.6 mm and

a total length of 14.2 mm [168].The oxygen permeability of the contact lenses was 1×10^{-9} $\frac{cm^3_{STP}.cm}{cm^2.s.cmHg}$. These contact lenses were fabricated by the copolymerization of monofunctional polydimethylsiloxane (MPMDSM), *N*,*N*-dimethylacrylamide (DMA), hydroxyethyl methacrylate (HEMA), siloxane macromer, tetraethyleneglycol dimethacrylate (TEGDMA), polyvinyl pyrrolidone (PVP), and they can accommodate 46 vol% of water (Appendix, Table 45. 1) [169-172]. To prepare a sample, the contact lens was dehydrated, attached to a glass slide, and a synthetic black dye (thickness ~ 915 nm) was directly deposited on it [26-29]. The thickness of the dye on the contact lens was estimated based on the transmission of different spin-coated thicknesses on glass substrates and compared with the published work. This thickness was chosen because it optimized laser interference in Denisyuk mode to provide a well-defined nanostructure to interact with the laser beam (Appendix ,Figure 5S.12)[61]**.** The lens was hydrated with deionized water (DI) and artificial tear solution (Hypromellose 0.3 wt% eye drop) [170, 171]. In addition, the contact lens was tested in a cuvette for continuous sensing measurements.

5.3.2-Fabrication of diffraction gratings on contact lenses

Holographic direct laser interference patterning was used in Denisyuk reflection mode. A nanosecond pulsed laser (λ=1064 nm, 240 mJ, 3.5 ns selected in Chapter 3) was used to ablate the black dye which was deposited over the contact lens surface by pen tip. The interference between the incident and reflected laser beams ablated localized regions of the dye medium. The exposure angle of all dye films was 35° from the surface plane of the plane mirror, which was used to produce the object beam in the holography setup.

5.3.3-Spectroscopic measurements of the ink gratings

The diffraction of light from 1D gratings was analyzed by normally illuminating the periodic samples with blue (λ=450 nm), green (λ=532 nm), and red (λ=635 nm) laser beams and recording the transmitted light on a flat screen placed perpendicularly 17 cm away from the sample. The testing was performed on plain lenses, black dyed lenses, and on lenses with patterned nanogratings, in three phase conditions (dry lens, wet with DI water and wet with artificial tear solution).

5.3.4-Angle-resolved measurements of the gratings

A halogen light source (HL-2000, Ocean Optics) and a goniometer setup were used to carry out angle-resolved measurements of diffraction efficiency on the ink nanogratings. The sample was placed 17 cm away from the optical probe to analyze the diffracted wavelengths. A motorized rotating stage was used for the broadband spectroscopic analysis of the rainbow diffraction produced by the nanostructure gratings. The rotation stage had a precision of 0.5° step from -90° to +90°.

5.4-Results and discussion

5.4.1-Holographic fabrication of nanostructures on contact lenses

Figure 5.1a shows a schematic of the hologram recording setup in Denisyuk ablation mode. The laser beams (λ=1064 nm) initially directed by a mirror travelled to the black dye on the contact lens (recording medium) and reflected off from a plane mirror, placed below, to ablate

the localized regions on the medium. The synthetic black dye on the contact lens was selectively ablated to form a holographic nanograting structure. This dye was chosen as it was able to increase the absorption to enable ablation to generate low-cost gratings [145, 147]. A holographic contact lens was produced through laser interference (Figure 5.1b). 1D and 2D nanostructures were created on the contact lens (Figure5.1c-d). The nanostructure fabricated on the contact lens was measured using optical and scanning electron microscopy techniques (Figure 5.1e). The contact lenses have different thicknesses and concave geometry for achieving comfort in the eye (Figure 5.1f). A dry contact lens was sliced to measure the lens thickness (Figure 5.1g) and the pattern was formed near the edge of the lens to prevent obstructing the vision through the centre of the lens. The lens was sandwiched between glass slides for testing purposes. The plain (unmodified) thickness was measured when the lens was at ambient moisture. The thickest of the lens was ~170 μm, which decreased to 65 μm in the central regions. On the other hand, the thickness of the lens increased to 185 μm at the edges and 85 μm in the centre when it was fully hydrated with DI water (Figure 5.1h).

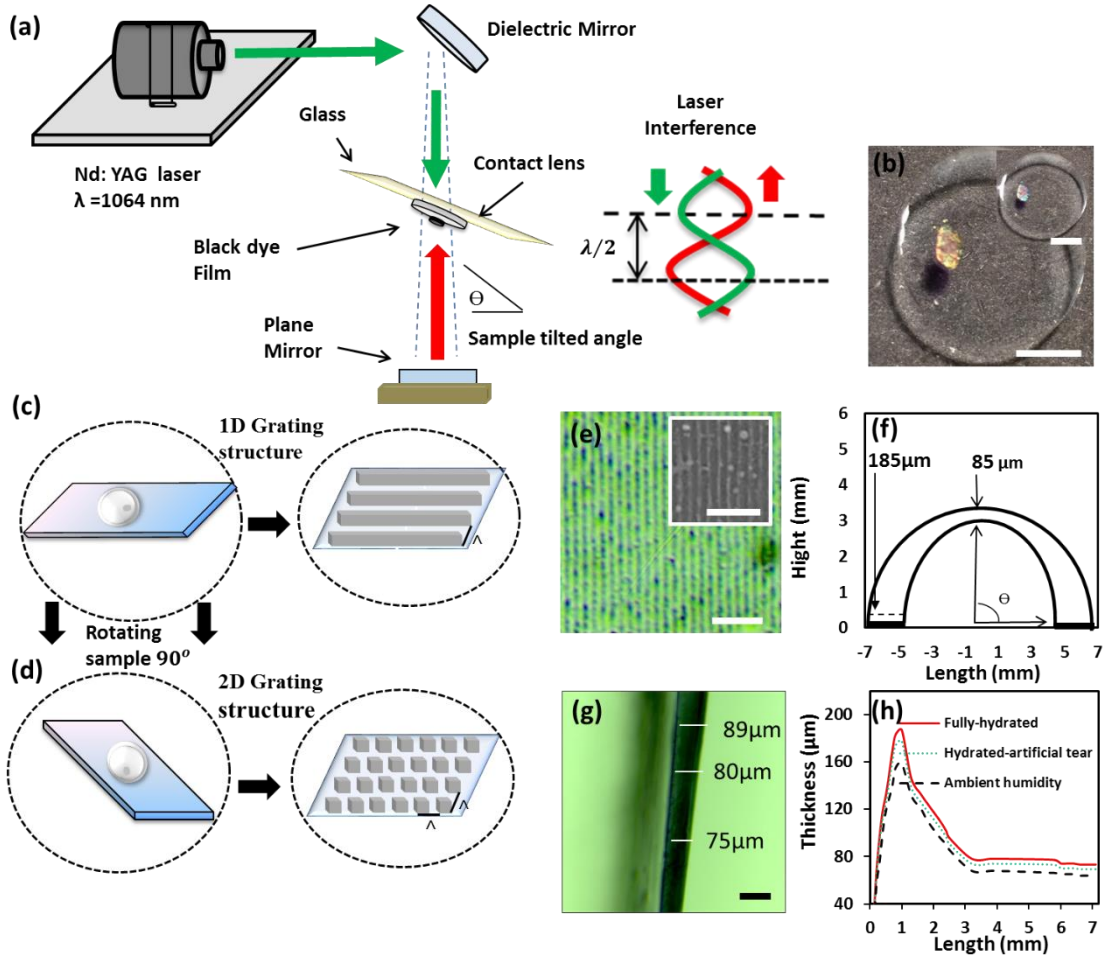

Figure 5.1: Fabrication of 1D nanopatterns on a contact lens through nanosecond DLIP in holographic Denisyuk reflection mode. (a) Nd:YAG laser beam (1064 nm, 3.5 ns) was guided by a mirror and passed through a dyed contact lens and reflected back from a plane mirror to ablate localized regions in the recording medium. (b) Fabricated ink-based holographic nanostructures on contact lenses (scale bar=5 mm). Schematics of (c) 1D and (d) 2D nanostructures. (e) Optical microscopy image of 1D nanostructure surface. The inset shows the SEM image of the surface topography (scale bar=5 μm). (f) Contact lens geometry and thickness distribution. (g) An optical image of a contact lens cross section in ambient humidity conditions (scale bar=100 μm). (h) Contact lens thickness change in ambient humidity, fully-hydrated condition in DI water, and hydrated condition in artificial tear.

The artificial tear solution decreased the thickness of the plain lens by ~10 vol% as compared to the DI water. This could be attributed to the decrease in Donnan osmotic pressure caused by the electrolytes in the artificial tear. The water content in the contact lenses were considered in equilibrium swelling degree q_w (Eq. 5.1), where $m_{ambient}$ was the lens mass in ambient humidity and $m_{hydrated}$ was the lens mass in fully-hydrated condition [100].

$$q_w = \left(\frac{m_{\text{ambient}}}{m_{\text{hydrated}}}\right) \times 100\ (\%) \qquad \text{(Eq. 5.1)}$$

Holographic DLIP ablates synthetic black dyes on the contact lens to form a grating. Nanoscale grooves were produced on the contact lens surface due to the high energy of interference. The main laser ablation process on the lens was created by the laser interference of two beams: Y_I is the incident laser wave (reference) and Y_R is the reflected laser wave (object) from a plane mirror. The higher energy of interference produced when two laser interacts with each other which can be described as:

$$Y_I = A\cos 2\pi\left(vt + \frac{x}{\lambda}\right) \qquad \text{(Eq. 5.2)}$$

$$Y_R = A\cos 2\pi\left(vt - \frac{x}{\lambda}\right) \qquad \text{(Eq. 5.3)}$$

$$Y = Y_I + Y_R = \left|2A\cos 2\pi\frac{x}{y}\right| \cos 2\,vt \qquad \text{(Eq. 5.4)}$$

where A, v, t and λ represent axis plane, velocity, time, and wavelength, respectively. The grating spacing depends on the exposure angle (Θ) of the contact lens at ambient conditions [48, 51]. At an exposure angle of 35° (from the horizontal plane), a grating spacing of 925 nm was produced. This spacing can be theoretically calculated by using the grating equation.

The difference between the experimental results of grating spacing and the analytical simulations was ~3% (Eq. 4.5)[12].

5.4.2-SEM structure images, light transmission and polarization on contact lenses

Figure 5.2a-c shows the SEM images of the fabricated nanostructures on the contact lenses and the optical transmission analyses in the wavelength range of 400-850 nm. The transmission studies were performed on plain lenses, lenses with thin black dye film, and the lenses with nanopatterned gratings. The lenses were tested in three phases: ambient humidity, fully-hydrated with DI water, and fully-hydrated with artificial tear. The transmission on the plain contact lens changed in different phases (Figure 5.2d). When the contact lens was in ambient humid condition, it had the highest transmission (95%). However, the transmission decreased in fully-hydrated DI water and artificial tear conditions. The contact lens was a transparent material in ambient humidity condition, but when in wet condition, an additional medium was absorbed by lens' matrix. This additional media changed the effective lens thickness and the refractive index which altered the absorption and transmission through the lens based on the refractive index of the solution (Figure 5.2d). However, the deposition of the black dye on the lens highly decreased the light transmission by 80% (Figure 5.2e) [61]. Increasing the absorption contributes to increasing the ablation efficiency with the Nd:YAG laser beam. However, if the absorption threshold reached >90%, laser beam could not ablate the sample as low-energy laser beam passes through the sample and returning beam from the plane mirror becomes ineffective in producing interference. The formation of the grating on the contact lens increased the transmission efficiency by 35% (Figure 5.2f). Light polarization was also measured in the plain lens at ambient humidity, fully-hydrated, and grating lens at ambient humidity conditions, where the light transmission ranged from 0° to 90°, reaching complete absorption (Figure 5.2g-i). Neither the fully-hydrated mode nor the black dye on the lens nor the grating nanostructures affected the polarization properties of the incident light.

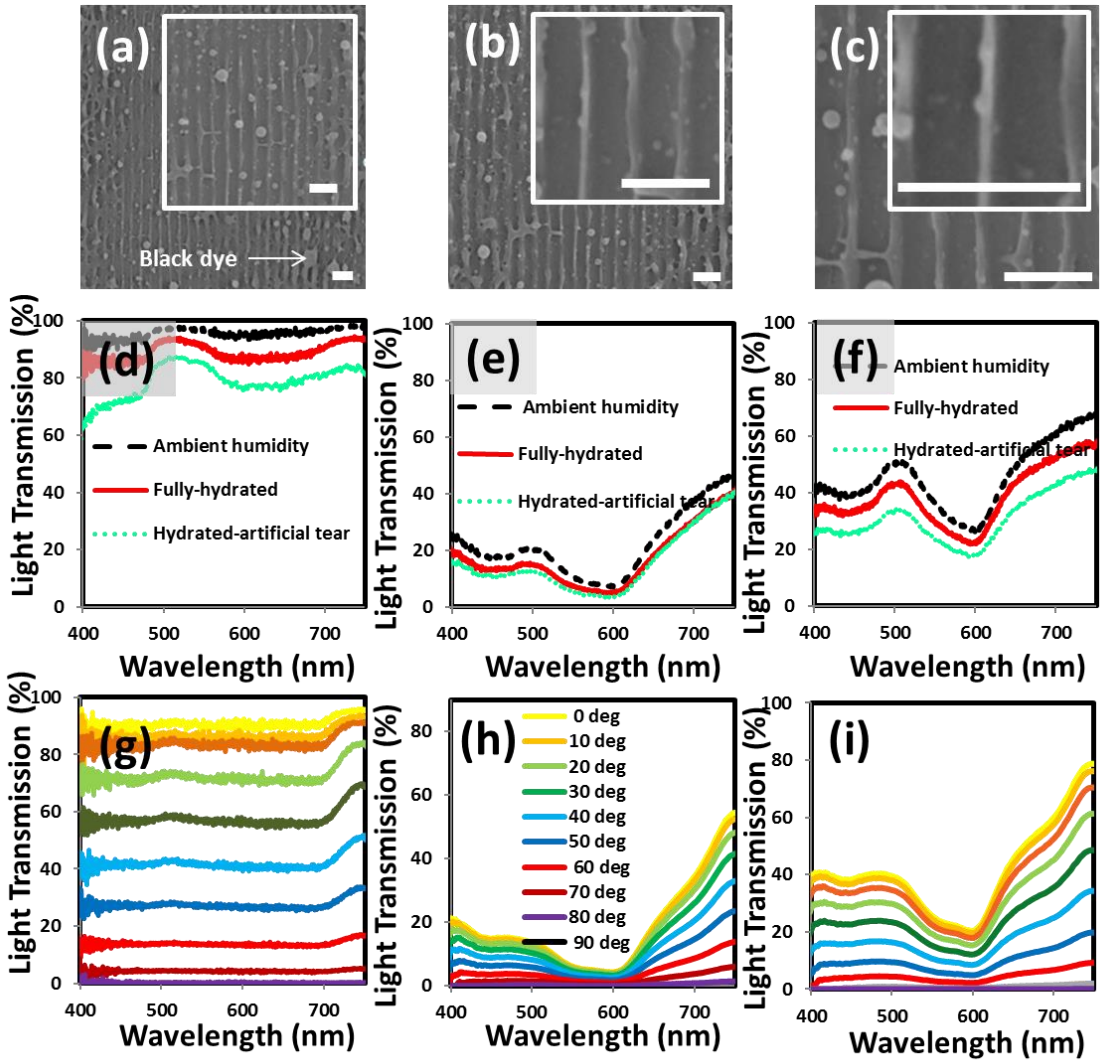

Figure 5.2: Electron microscopy and spectroscopy analyses of the nanopatterned (a-c) SEM images of 1D nanostructures on the contact lens with increasing magnification (scale bar=5 μm). Scale bar for (c) is 2 μm. The optical transmission spectra for commercial contact lens in three conditions: (d) plain lens, (e) black dye coated the lens, (f) and nanopatterned lens at different moisture conditions. Effect of incident light polarization on transmission in (g) fully-hydrated plain lens, (h) dyed lens in ambient humidity, and (i) nanopatterned lens in ambient humidity.

The depth profile was simulated on z(x,y) plane to characterize the groove measurement. The vertical and horizontal axes represent the repeated periodicity of Gaussian distribution. The 1D pattern was simulated to have a groove spacing of 925 nm and a depth of 800 nm at refractive indexes of ambient humidity 1.50, fully-hydrated 1.40 and hydrated with artificial tear 1.33.

Similarly, modulation of the 1D phase difference was produced based on the difference path profile of the nanostructure at the x-y plane (Eq. 5.5-7).

$$\Theta(x,y) = z(x,y)k_{1+}(z_{max}\text{-}z(x,y))k_0 \quad \text{(Eq. 5.5)}$$

k_1 and k_0 represent the vectors of the substrate and the z_{max} is the maximum depth. The phase difference can be summarized with arbitrary phase constant Φ:

$$\Theta(x,y) = z(x,y)(k_1 - k_0)+\Phi \quad \text{(Eq. 5.6)}$$

Phase constant can be modulated as the complex value to become:

$$I(x,y) = I_0(x,y)\, e^{i\Theta(x,y)} \quad \text{(Eq. 5.7)}$$

where laser beam intensity profile (Gaussian beam illumination) represented by I_0 and I(x,y) was used to compute the diffraction of the far field[116]. Diffraction from 1D nanostructures on the contact lens gratings were simulated (Figure 5.3a1-c1). The experimental illumination from three monochromatic light sources (450 nm, 532 nm and 635 nm) were analyzed. The blue laser beam illumination (450 nm) on the lens nanopatterns resulted in the diffraction of the first order at 27° (Eq. 4.6)[61].

Where *m* represents the diffraction order. As the contact lens was soaked in DI water for 20 min, the thickness of the lens increased, elevating the first order diffraction to 29°. Then the contact lens was brought back to ambient humidity and immersed in artificial tear for 30 min. It was kept for longer time because the artificial tear had higher viscosity (6.4 $mm^2\ s^{-1}$) than water at 24°[173]. The optical analysis showed additional degrees of angular diffraction (Figure 5.3a2). The simulated diffraction values of lens at ambient conditions were identical to that of fully-hydrated lens (Eq. 5.8). The green laser beam illumination (532 nm) on the lens nanopattern showed an increase in diffraction angle for the first order showing 34° for the lens

having ambient humidity condition. The diffraction increased by 2° when the lens was fully hydrated and had additional 2° when it was hydrated with artificial tear (Figure 5.3b2).

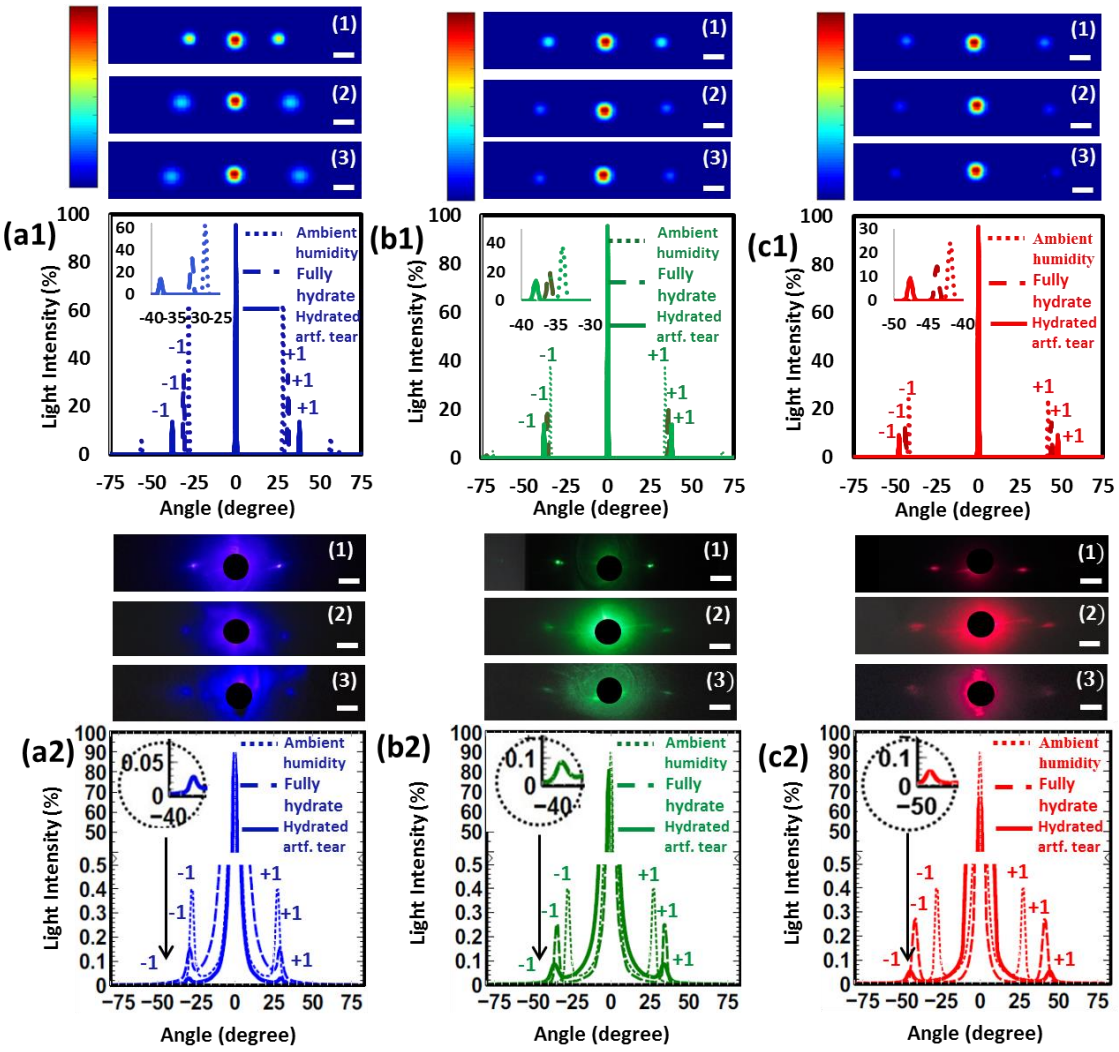

Figure 5.3: 1D surface grating nanostructures fabricated by holographic DLIP.Simulation and experimental diffraction results for gratings with a periodicity of Λ=925 nm on the contact lens surfaces in ambient humidity, fully-hydrated and artificial tear conditions. (a1) Simulated and (a2) experimental diffraction results for 450 nm wavelength at different humidity conditions. (b1) Simulated and (b2) experimental diffraction changes at 532 nm. (c1) Simulated and (c2) experimental diffraction for 635 nm. Scale bar=5 cm.

Similar trend of change was obtained with the red laser beam illumination (635 nm) on the grating, but the diffraction angle was higher than that of the blue and green lasers. There was 4° difference between the contact lenses at ambient moisture and fully-hydrated conditions. The difference in diffraction with ambient humidity state and fully-hydrated condition with artificial

tear was ~7° (Figure 5.3c2). The theoretical values were estimated based on the effective refractive index of DI water with contact lens (~1.40) and artificial tears (1.336). Although the refractive index of pure DI water is 1.33, but when it is measured within the contact lens, it becomes ~1.40. The observations showed that the experimental results matched with the theoretical values. However, in the case of the artificial tears, the refractive index was equivalent to the human tear [169, 172-174] .Table 5.1 shows the experimental and theoretical diffraction values of all wavelengths.

Table 5.1: Diffraction from contact lens gratings using three laser beams (450 nm, 532 nm, 635 nm) and comparison to the theoretical values. Exp: Experimental diffraction angle, Theo: Theoretical diffraction angle values. amb-hum:ambient humidity, full-hyd:fully-hydrated, and hyd-tear: hydrated with tear.

Laser wavelength (nm)	Exp. Amb.hum (°)	Theo. amb-hum (°)	Exp. full-hyd (°)	Theo. full-hyd (°)	Exp. hyd-tear (°)	Theo. hyd-tear (°)
450	27	29	29	32	31	33
532	34	35	36	37	38	39
635	41	43	45	45	48	47

The illumination diffraction angles of each wavelength were influenced by the nanostructure on the surface of the contact lens. Longer wavelengths of laser light diffracted through a larger angle than the shorter wavelengths. In addition, the lens in ambient moisture had the lowest diffraction angle as compared to the other two states because the lens was the thinnest in this condition. Increasing the lens thickness contributed to reducing the lens grating gap which increased the diffraction angles. In addition, artificial tear in lens showed higher diffraction angle than the fully-hydrated condition in DI water although it had proportionally smaller effective thickness. This phenomenon can be attributed to the decrease in Donnan osmotic pressure within the contact lens caused by the presence of electrolytes in artificial tear.

Therefore, the grating structure in the lens could be used as a generic sensor to measure analyte concentrations based on ionic changes from human eye tears *via* rapid light diffraction changes:

$$m=2\pi n_o \Lambda \sin \Theta/\lambda \quad \text{(Eq. 5.8)}$$

Where $\mathbf{n_o}$ represents effective refractive index.

5.4.3-Fabrication of 2D nanostructures on contact lenses

2D periodic square nanostructures were also fabricated with holographic DLIP by exposing the recording medium to two beam pulses. The sample was rotated 90° after the first exposure to produce the 2D square patterning, with the same tilt angle used in both exposures (Figure 5.1a). The 2D grating structure had a periodicity 925 nm × 925 nm (Figure 5.4a). The 2D nanopatterning enhanced the transmission by 10% in the all phases as compared to the 1D structure with ambient humidity state and fully-hydrated condition with artificial tear (Figure 5.4b). This was due to reduced dye coated regions and overall more transparent lenses. The diffraction measurements were performed with illuminations from three laser beams on the 2D grating structure to measure the optical properties of the lenses. The 450 nm illumination produced four diffraction spots from the 2D patterning. The diffraction points were at 27° on the x and y-axes (Figure 5.4c-d). Similarly, the diffraction angles were 34° for 532 nm (Figure 5.4e-f) and 41° for the 635 nm laser wavelengths (Figure 5.4g-h). The 2D pattern was compared with 1D grating based on the diffraction efficiency. The diffraction efficiencies ($\boldsymbol{I_{eff} = I_1/I_0}$) of the lenses were considered from the relation of the intensity of the first order $\boldsymbol{I_1}$ and the zero-order intensity $\boldsymbol{I_0}$. Although the diffraction intensity in the three laser illuminations were close for the both 1D and 2D in the x-axis, the efficiency of the 2D grating was higher. The zero-order diffraction of the 2D grating was lower than that of the 1D, which indicated higher

efficiency at x-axis. In addition, the 2D gratings had additional diffraction spots along the y-axis due to the geometry of structures. As a result, the 2D diffraction patterns had higher diffraction efficiency and they added more optical features by increasing the number of dimensions in which light was diffracted.

5.4.4-Spectrum rainbow diffraction measurement

To evaluate the response of the nanopatterns to broadband white light, a goniometer setup was used to carry out angle-resolved diffraction efficiency measurements. Diffraction spots from the nanostructures of contact lens were analyzed in transmission mode. The spectroscopic analysis of the rainbow diffraction was performed on a motorized rotating stage with a broadband halogen light source illumination. The rainbow distribution of grating diffraction was recorded by moving the motorized stage with 0.5° step increments from -90° to +90° (Figure 5.5a). The 1D and 2D rainbow diffractions of the two contact lenses were measured. The length measurements were based on placing a screen at 16 cm away from diffraction samples. The angle-resolved diffraction from the two lens gratings were measured at a maximum broadband light intensity to quantify the highest value of diffracted wavelength distribution. The maximization enabled to have the same bandwidth of grating diffraction within the range of 400-850 nm to compare 1D and 2D x-axes nanostructured patterns. The rainbow diffraction patterns of 1D and 2D lens gratings had same arcs (37° to 58°). These patterns showed low visible wavelength intensity at 570 nm. The diffraction efficiency of contact lens with ambient humidity condition was less than 10% for the two patterns (Figure 5.5b). The 2D nanostructures formed four rainbow diffraction patterns based on the shape of the nanostructure.

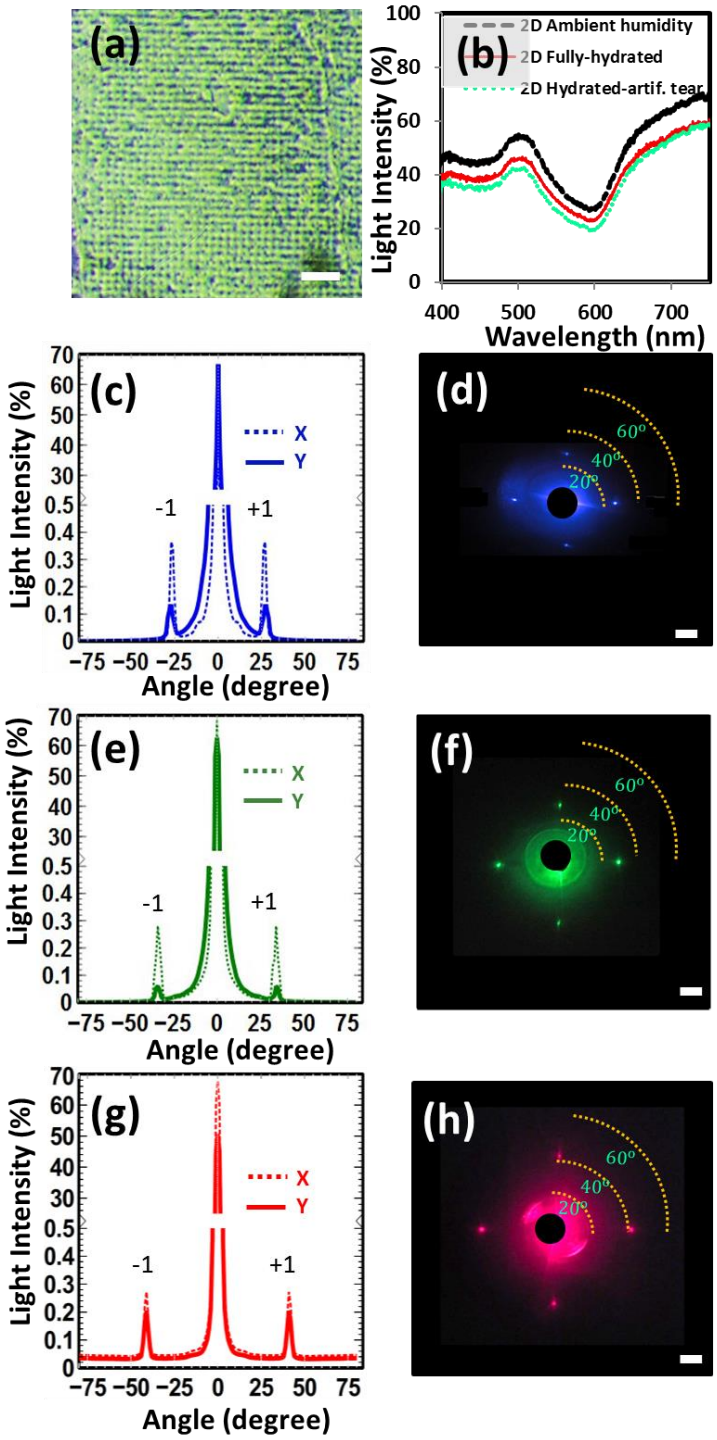

Figure 5.4: Optical characterization of 2D surface grating nanostructures (925 nm × 925 nm) fabricated by holographic DLIP on the contact lens. (a) An optical microscopy image of the 2D grating. (b) Angle-resolve measurements of diffraction readouts in transmission mode upon illumination with three monochromatic beams: (c-d) 450 nm, (e-f) 532 nm, and (g-h) 635 nm. (scale bar=5 cm)

The x-axis of the 2D grating generated similar trend and intensity as compared to the 1D rainbow diffraction patterns. The second rainbow diffraction of the 2D grating in y-axis had lower intensity. Figure 5.5c shows holographic contact lens attached on an artificial eye model showing the location of the nanostructure. The 2D rainbow image displayed diffraction in x and y axes (Figure 5.5d).

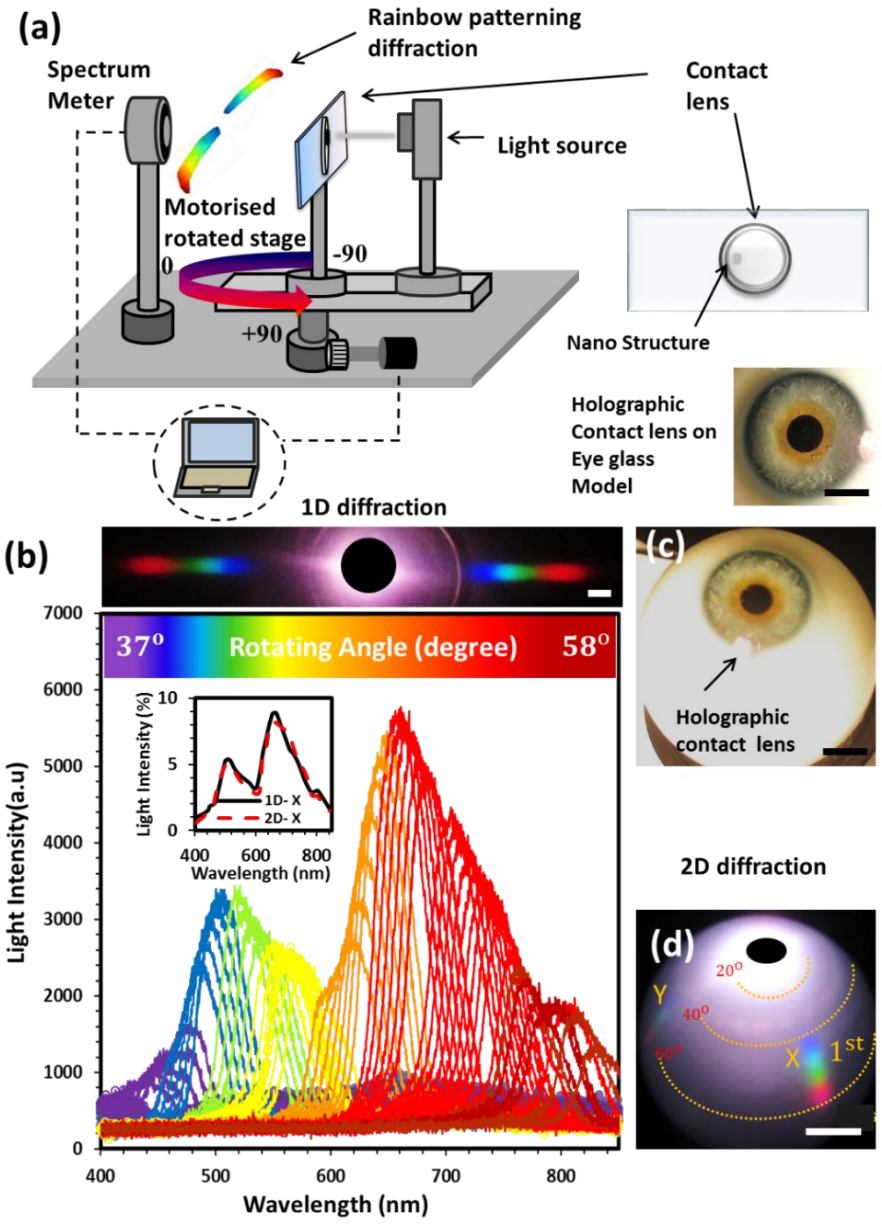

Figure 5.5: Angle-resolve measurements of the 1D and 2D diffraction patterns from the contact lens. (a) The spectroscopic measurement of the rainbow diffraction of 1D nanostructure over the contact lens in transmission mode using a broadband light. Scale bar=5 mm. (b) Broadband white light angular measurements for 1D and 2D gratings along the x-axis. Scale bar=5 mm. (c) Holographic contact lens on an eye model. (d) 2D rainbow diffraction of the holographic contact lens on spherical screen. (scale bar=1 cm)

5.5-Fabrication of different nanostructures on contact lenses

Fabricating nanostructures on the contact lens can change the surface contact angle as well as the optical properties. If the contact angle increases due to the nanopatterning of the surface then the contact lens will become more hydrophobic. Therefore, its softness will decrease and its suitability for human eye wear will become a challenge as it can cause irritation [175]. The hydrophobicity of unmodified contact lens with sessile drop test (5 μl) was ~59°,[176] whereas the 1D nanopatterned contact angle displayed 62.8° (Figure 5.1e). Four different nanopatterning structures were produced for this experiment. The 1.28 μm × 1.28 μm structure showed similar structural patterns as the earlier 2D nanostructure, but it had a relatively larger grating spacing (Figure 5.6a1). However, the diffraction on the nanopatterns showed two orders on each side of the x and y axes with 8 diffraction spots in total (Figure 5.6b1). The 2D square structure produced four identical rainbow diffraction patterns but closer to the zero order (Figure 5.6c1). The square nanopatterning showed some increase in the contact angle, reaching ~71° (Figure 4.6d1). The second nanostructure was a rectangular pattern and had a grating size of 1.68 μm × 1.45 μm (Figure 5.6a2). It produced 12 diffraction spots, which were influenced from the grating spacing and shape (Figure 5.6b2) [51]. In addition, it created four visible rainbow diffraction patterns (Figure 5.6c2) and the contact angle was lower than the first nanostructure (Figure 5.62d).

The next nanostructure was a rectangular pattern produced by three laser pulse exposures to obtain spacings of 0.85 μm × 2.4 μm (Figure 5.6a3). The 2D nanostructure produced three horizontal sets of diffraction (Figure 5.6b3). Two orders of rainbow diffraction were produced in each axis (Figure 5.6c3). The contact angle showed an increase of 11° as compared to the

contact lens in ambient humidity (Figure 5.6d3). The final structure was fabricated with three laser pulses and had a smaller nanostructure geometry between large gaps (Figure 5.6a4). The contact angle measured was ~62.5°, closest to the 1D nanopatterned lens and the unmodified contact lens (Figure 56b4).

Holographic DLIP system enabled producing different types of nanopatterns on the soft and fragile lens surfaces. The contact lens material (silicone-hydrogel), which is not purely solid at ambient humidity conditions, withstood up to three laser pulses without significant damage to the relatively thin matrix. The four different nanoscale shapes fabricated had an effect on the arrangement of diffraction distributions, with grating spacing influencing the location of the diffraction spots. Structures shown in Figure 5.6a1 and Figure 5.6a3 displayed an increase in the contact angle although the structure area on the lens was relatively smaller (2 mm). The nanostructure geometries can be easily optimized by vary the nanostructure to tailor the wetting properties of contact lenses to suit various eye conditions and comfort levels.

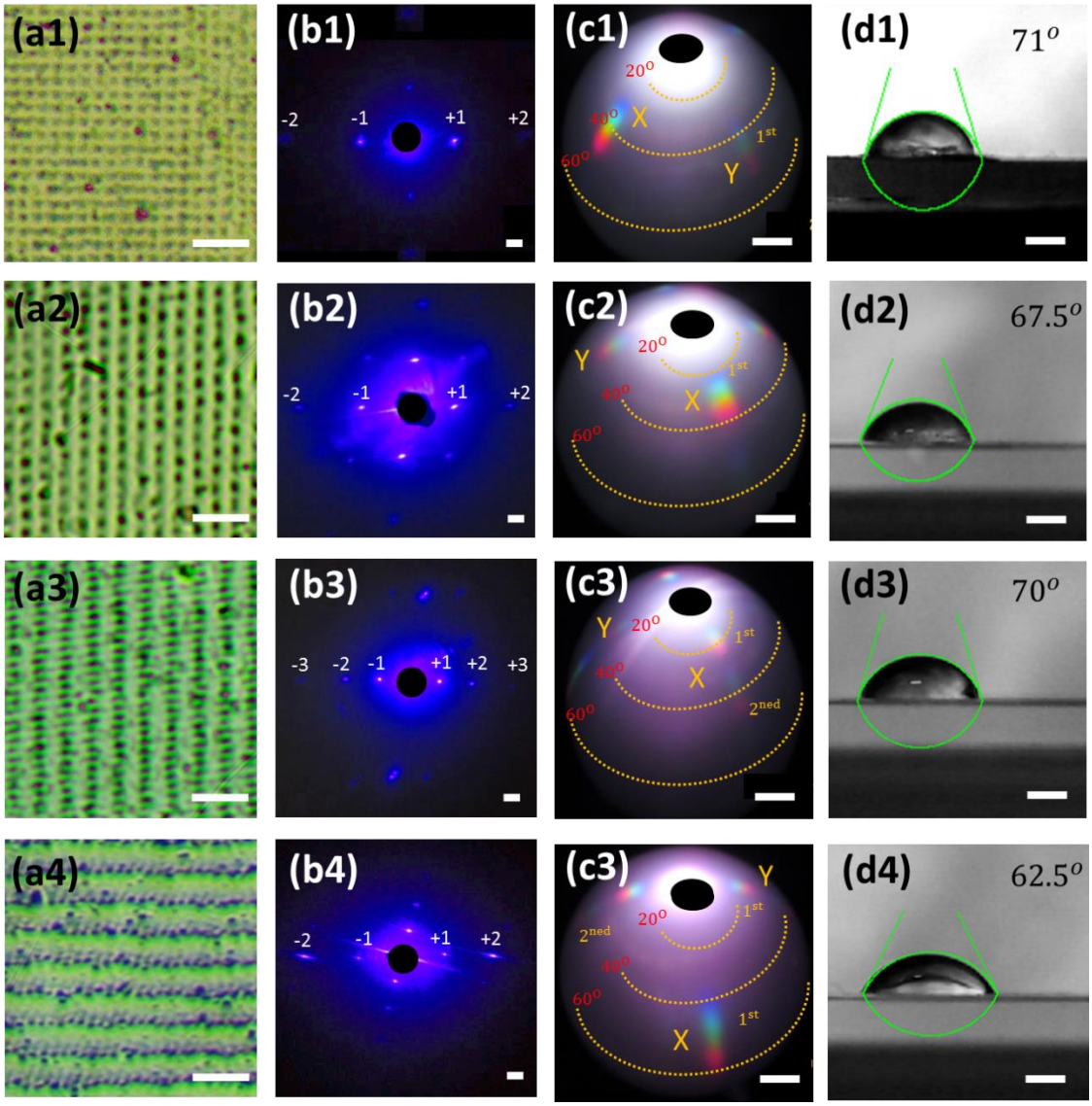

Figure 5.6: Optical microscopy images of 2D nanostructures with different geometries on contact lenses. (a1) 1.3 µm × 1.3 µm, (2a) 1.7 µm × 1.5 µm, (a3) 0.9 µm × 2.4 µm, and (a4) 0.9 µm × 2.7 µm. Scale bars = 5 µm. (b1-4) Diffraction of monochromatic light (450 nm) *via* 2D patterned arrays. Scale bar=1.0 cm. (c1-4) Rainbow diffraction from 2D patterned arrays, scale bar=1.0 cm. (d1-4) Contact angle measurements of 2D nanostructures on contact lenses. (scale bars = 1.0 mm)

5.6-Nanostructures on contact lenses for optical sensing

The nanopatterned contact lens was used as a generic sensor. One of the 2D nanostructure patterns (925 nm × 1555 nm) was used to sense analytes in the artificial tears. The x-axis diffraction pattern (in response to 925 nm spacing) was used to detect different concentrations

of Na^+ ions in tears, as an increase or decrease in electrolytes can be an indication of eye disorders [158]. The normal concentration of Na^+ and Cl^- ions in human tears are 142 mmol L^{-1} and 135 mmol L^{-1}, respectively [177]. Different concentrations were prepared in DI water for testing purposes. The contact lens was placed in a cuvette for continuous optical measurements. The black dye and nanostructured contact lenses were tested in transmission mode in the cuvette at different Na^+ ion concentrations. The transmission of the black ink dye on contact lens showed no significant change from 0 mmol L^{-1} and 230 mmol L^{-1} Na^+ ions but decreased at higher concentrations (Figure 5.7a).

The transmission increased through the nanopatterned contact lens and the diffraction intensity changed with increasing Na^+ ions in the solution (Figure 5.7b). The nanogratings on the lens surface had periodic grooves and the refractive index of the groove medium changed the grating's diffraction properties. Hence, the variation in transmission was based on the change in the effective refractive index due to the change of electrolyte concentrations (Figure 5.7c1-4 and Appendix Table 5S.2). The diffraction measurements for the contact lens nanostructures were carried out with a 635 nm laser illumination. The readings were recorded every 10 min with different electrolyte concentrations. This time frame was selected as sufficient period to achieve equal comparison between all concentrations. (The results showed an increase in diffraction angle with increasing concentration of Na^+ ions (Figure 5.7d). It is hypothesized that the increase in ion concentrations caused the lens to expel water and shrink, leading to a decrease in grating spacings and hence an increase in diffraction angles. The lenses can be further functionalized by using engineered dyes/materials which respond to specific analyses such as glucose, electrolytes, or proteins.

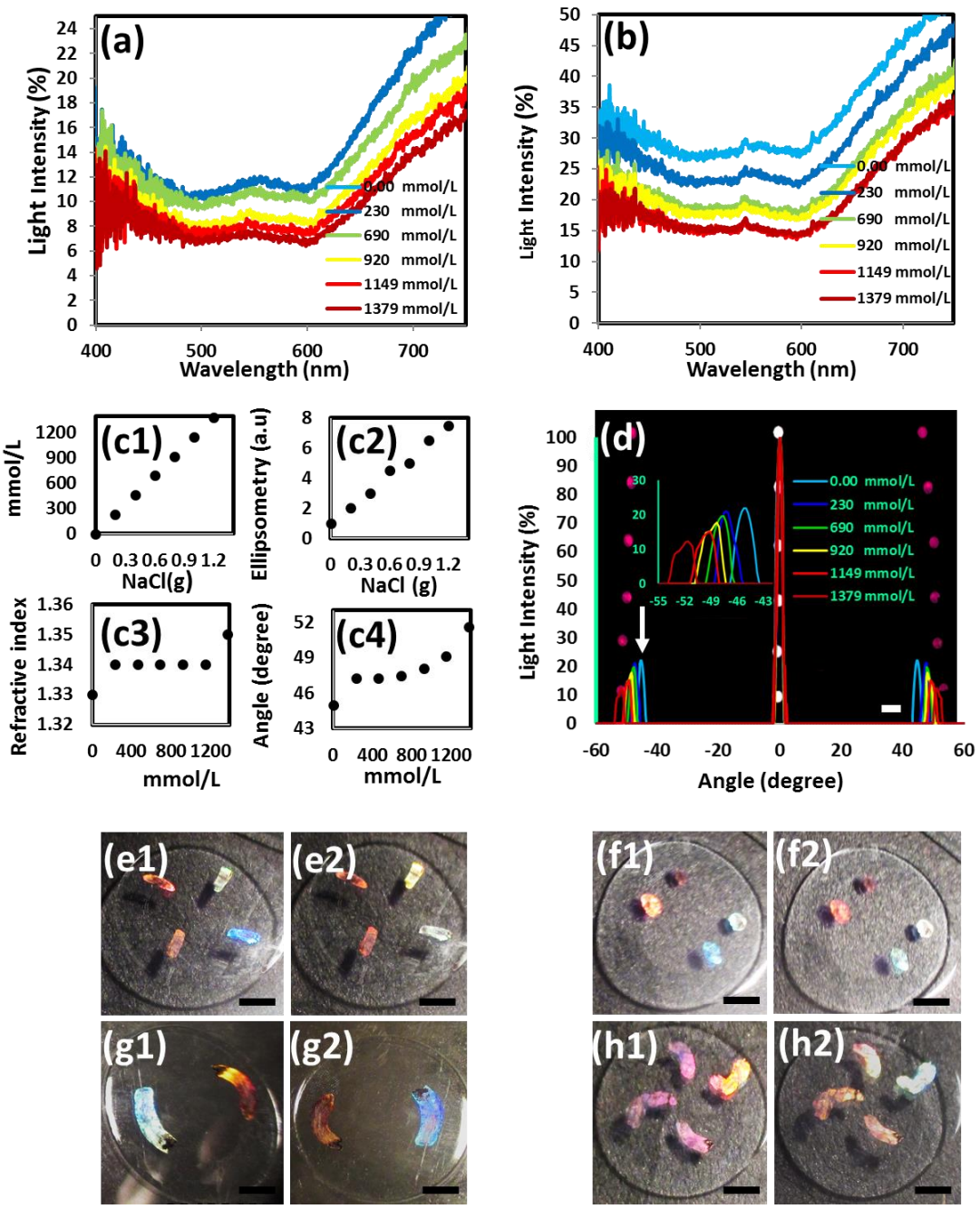

Figure 5.7: Light transmission spectra as a function of Na^+ ion concentrations(a) Dye coated lens and (b) nanograting on contact lens. (c1-c4) Ellipsometry, refractive index, and grating diffractive angle measurements of Na^+ ion concentrations (Table S5.3). (d) Diffraction measurements on the nanopatterned contact lens at different Na^+ ion concentrations. Scale bar=5 cm. (e-h) Different designs (rings/patches) of holographic nanostructures fabricated on contact lenses. Each image demonstrates the diffraction colours observed at various angles. (scale bar=5 mm)

We also fabricated various holographic patterns (nanostructures) on contact lenses to show the flexibility and uniformity of the laser-based fabrication method (Figure 5.7e1-h2). The holographic structures on contact lenses displayed rainbow diffraction effects upon illumination with broadband white light. These nanostructures can be designed in various shapes (rings/patches) and can be used for sensing and also to enhance the appearance of the contact lenses, for example for cosmetic purposes. Furthermore, the nanopatterns may change their visible colors in response to changes in the curvature of the eyes, hence allowing the clinicians to monitor ocular pressure in the diagnosis of glaucoma.

5.8-Conclusions

With the low-cost and direct holographic DLIP method optical nanostructures were produced on commercial contact lenses. Depositing a synthetic black dye on the contact lens allowed the formation of surface nanogratings on the hydrogel matrix using a pulsed Nd:YAG laser. These optical nanostructures were fabricated at the edge of the contact lens to prevent any sight obstruction or interference of human vision. The formation of 2D nanostructures on lens surface increased the diffraction intensity by more than 10% as compared to 1D nanostructures. The versatility of holographic laser ablation method was demonstrated by creating four different 2D nanopatterns with different designs on the contact lens surface without significantly changing the hydrophilicity properties. Additionally, direct sensing of Na^+ ions was conducted by measuring the transmission and diffraction properties. Ocular conditions such as edema, Graves' eye disease, and glaucoma can be potentially monitored from the change of eye curvature which will have direct influence on the shape and spacing of nanostructure fabricated on the lens surface. Other ocular diseases can also be predicted in

early stages when the contact lens matrix is functionalized and integrated with the nanostructures to recognize concentration changes of analytes and proteins in human tears.

Associated content

Supporting information

Preparation of the lenses; black ink gratings at different thicknesses in transmission and diffraction modes; material properties of the contact lenses; NaCl in DI water at different concentrations and ellipsometry equivalent reading of refractive index values (Appendix, Table S5.2).

Chapter 6: CURVE PHOTONIC STRUCTURES FOR SENSNIG

This chapter is based on a Submitted Journal Paper

AlQattan B. [(1)], Benton D. [(2)], Yetisen A. K. [(3),] Butt H. [(1)]: Curve Photonic Structure for Sensing.(2019)

[(1)] Nanotechnology Laboratory, School of Engineering, University of Birmingham, Birmingham B15 2TT, UK.

[(2)] Aston Institute of Photonics Technologies, Aston University, Birmingham, B4 7ET, UK

[(3)]Harvard-MIT Division of Health Sciences and Technology, Massachusetts Institute of Technology, Cambridge, MA 02139, USA

Author contributions: Bader AlQattan is the main author of the work and he conceived the idea of producing a Fresnel lens and curved nanostructure. He designed the experiments, executed all necessary optical characterization, carried out data analysis, and wrote the manuscript. The rest of the co-authors Dr David Benton, Dr Ali K. Yetisen, and the principal supervisor, Dr Haider Butt reviewed and edited the manuscript.

6.1-Abstract

A holographic ablation based on direct laser interference was used to produce non-linear nanostructures. The black ink dye was used to form circular and curved nanopatterns. An optical investigation of the nanostructure was developed on glass before it was deposited on a commercial adhesive tape. The non-linear nanostructures could be used in sensing and imaging for buildings' construction, aircrafts, and human interface devices. (Curve Photonic Structure for Sensing).

6.2-Introduction

Tension indicators are greatly needed for monitoring and recording health conditions in civil engineering, airspace and human interface applications. There are many complex systems, extremely large and non-planar surfaces which require vigorous alert systems to prevent any catastrophic damage from happening [178]. For example, stalactite straws growing beneath concrete are able to damage a building's structure. Humidity, low air circulation, CO_2concentration, pH level and other chemical reactions lead to speeding up the growth of these straws, which could degrade the concrete texture [179]. In the USA there are more than 600,000 bridges which make it hard for continuous inspections due to the growing maintenance cost. One in four bridges could be considered structurally inadequate for use, which would raise a public safety concern. MicroStrain miniature sensors use nodes in a bridge structure for wireless discrete placement to measure structure problems such as vibration, load, strain, corrosion, displacement and tilt. They are able to measure bending strains of +/- 400 με [180] Similarly, non-destructive testing (NDT) techniques which use a robot to inspect bridge cables,

require a high-voltage X-ray tube and gamma rays for detecting wire cable damage at every 0.3 m [105, 106]. Some airplane structures are made from carbon fibre as a light material, but unpredictable discrete events can cause structural delamination. In addition, most modern airplanes are made of a composite material structure which can have complex failures, such as resin cracking, fibre breakout and disjointing. These failure mechanisms are hard to detect and require frequent manual inspections; so this leads to inflation of the airlines' operating costs. [181, 182]. Fibre Bragg grating (FBG) has been used in airplanes and other engineering applications to measure tension load by light wavelength as a reliable response technique. Gluing FBG under the composite skin and stiffener has contributed to health monitoring in most large aircrafts. However, it could interoperate a failure occurrence close to the localised area, and it has weak deformation capability and a small measurement range (< 2%) 1 mm/m resolution [108, 183, 184]. Some transducer strain sensors are able to measure large deformation (mm scales) and instability on unconventional surfaces [104, 106, 109]. There are other types of flexible, low power consumption and lightweight strain sensors. They are designed to have high stretchability and employ piezoresistive strain sensing. Nevertheless they require many steps of chemical procedures [178, 185, 186].

Feasible and highly responsive strain sensors could be made by optical nanostructures because they enable the control of the light direction [110, 187]. However, metal nanopatterning structurers and semiconductor film for strain sensors have been used, but they showed limitations in flexibility and dynamic systems [178, 188]. A non-linear nanostructure could provide a strong non-linear response[110, 189]. An integrated nanostructure on a commercial adhesive tape would produce a low cost and flexible strain sensor to integrate on any surface. However, integrating nanoscale features into tape represents a fundamental challenge. Some nanofabrication methods are able to form optical structures, but they are considered costly and time consuming [21, 131, 190]. Methods like contact facile stamping, micro moulding, E-

beam, and ultrashort laser pulse lithography could be used to fabricate nanostructures on tape [12, 22, 34]. However, these fabrication methods require complex set-ups, high-energy supplies, multiple steps, expensive equipment and long fabrication times [116, 131, 164]. In addition, there are many laser interference systems that are able to produce nanostructures [45]; however, they would damage the target substrate (tape) because of the high pulse beam energy [191] .

Optical nanostructures can rapidly be produced at low cost by a holographic laser ablation method. Deposited black dye is able to produce ablative interference fringes by direct laser interference patterning (DLIP). Holographic DLIP of the Denisyuk reflection mode can make a Fresnal zone plate (Fzp) and a distorted nano structure or curved grating (CG) from black dye on the top of tape without damaging it [4, 124]. Additional samples are created by changing the samples' tilted angle range between 5^0 and 35^0 at different incident positions on a concave mirror, to get different pulse waves' reflections. Moreover, 2D nanostructures were fabricated to study the light diffraction effects with monochromatic light and wettability of 1D and 2D nanostructures. The nanostructure on the tape measured the stretching for sensing.

6.3-Materials and methods

6.3.1-Preparation of the recording media of the sensing tape

In the first stage, a black dye (Staedtler Lumocolor) was deposited on a slide glass. Diluted ink solutions (1:8, v/v in ethanol) were spin coated on 1 mm thick glass slides at 200 rpm for 35 s. The dyes used were permanent and had a long-term durability based on the manufacturer's information and from previous experiments. In the final stage, back dye was deposited on a stronger adhesive tape (Gorilla- crystal clear) on a slide glass. The thickness of the dye on the

glass and the tape has been considered based on established work through the transmission mode optical spectra of different spin-coated thicknesses on glass substrates (Appendix Figure 5S12) [61].

6.3.2-Fabrication of diffraction gratings on glass on adhesive tape

Holographic direct laser interference patterning was used in a Denisyuk reflection mode. A nanosecond pulsed laser (λ = 1064 nm, 180 mJ, 3.5 ns selected in Chapter 3) was used to ablate the black dye deposited on the glass surface and the same on the stretchable tape. The interference between the incident and reflected laser beams ablated localized regions on the dye medium. The exposure angle of all dye films was 0°-35° from the surface of the concave mirror, which was used to produce the object beam in the holography set-up. The concave mirror had a 12.7-mm diameter; the thickness of the mirror was 3.1 mm at the edge and 3 mm at the deepest point in the centre.

6.3.3-Spectroscopic measurements of the ink gratings

The diffraction of light from 1D and 2D gratings was analyzed by normally illuminating the periodic samples with blue (λ = 450 nm), green (λ = 532 nm), and red (λ = 635 nm) laser beams and recording the transmitted light on a flat screen placed perpendicularly 17 cm away from the sample. The testing was performed on black patterned nanogratings. A motorized rotating stage was used for broadband spectroscopic analysis of the diffraction through the nanostructure gratings. The rotation stage had 1° steps from ranging from -90° to +90°.

6.3.4-Angle-resolved measurements of the gratings

A halogen light source (HL-2000, Ocean Optics) with a goniometer set-up was used to achieve angle-resolved measurements of diffraction efficiency on the ink nanogratings. Analysis of the diffracted wavelengths was carried out by placing the sample 17 cm away from the optical probe. A motorized rotating stage was used for the broadband spectroscopic analysis of the rainbow diffraction, which was produced by the nanostructure gratings. The rotation stage had a precision of 0.5° step from the left side 0° to -90° and the right side 0° to +90°.

6.4-Results and discussion

6.4.1-Holographic fabrication of Fresnel zone plate and distorted nanostructures

At first, the glasses were coated with the black dye which acted as a recording medium to get accurate and reliable measurements. The dye was selected because it can interact with a laser beam to make a well-defined nanostructure [48]. According to the manufacturer, the black dye had a long-term durability of five years. In some recognized experiments, there was no change in the nanostructure quality after more than three years of use. The black dye had a 915-nm thickness based on the subsequent experiments from the established work (Appendix Figure 5S12) [61, 130, 145]. Figure 6.1(a) illustrates the set-up diagram of the Denisyuk ablation mode to make the holographic structure on the recording medium. Initially, the laser beam was directed by a dielectric mirror to eliminate any possible waves from the laser beam, then it was guided to a plain mirror for two different sets of mirrors. The laser beam was directed to the first set by the other plain mirrors towards the black dye to pass the recording medium and was

reflected from the centre of a concave mirror. The reflected beam waves from the centre point of the concave mirror were aimed to focal point (f_c) at 50 mm (Eq. 6.1). However, the incident and returning laser beams were interfered with by the black dye before they reached the focal point to ablate the localized regions on the medium. Due to the concave mirror having a surface change of 100 µm, the reflection beams were modulated into a quadruple amplitude wave, which ablated different circular periodicities at the exposed region on the dye [192]. However, the amplitude wave which was reflected from the deepest centre zone (the centre of the mirror) did not change because it returned to the same original direction without any interface beam wave. As a result, the ablation produced a Fresnel zone plate (Fzp) structure (Figure 6.1(b1-3)) [49].

In the second laser beam exposure process the laser beam was directed to the edge or the side of the concave mirror, so part of the incident laser beam was reflected from one edge of the concave surface. The quadruple reflected laser profile ablates part of the localized region on the black dye medium, to form a distorted structure or curved grating (CG) in a set of semi-circles (Figure 6.1(c1-3)). Both structures are gratings resulting from the laser interference produced from various parts of the concave mirrors which produce non-linear structures [112, 149, 192, 193].

$$f_c = \frac{1}{2} r_c \qquad \text{(Eq. 6.1)}$$

Where r_c is the radius of the concave mirror.

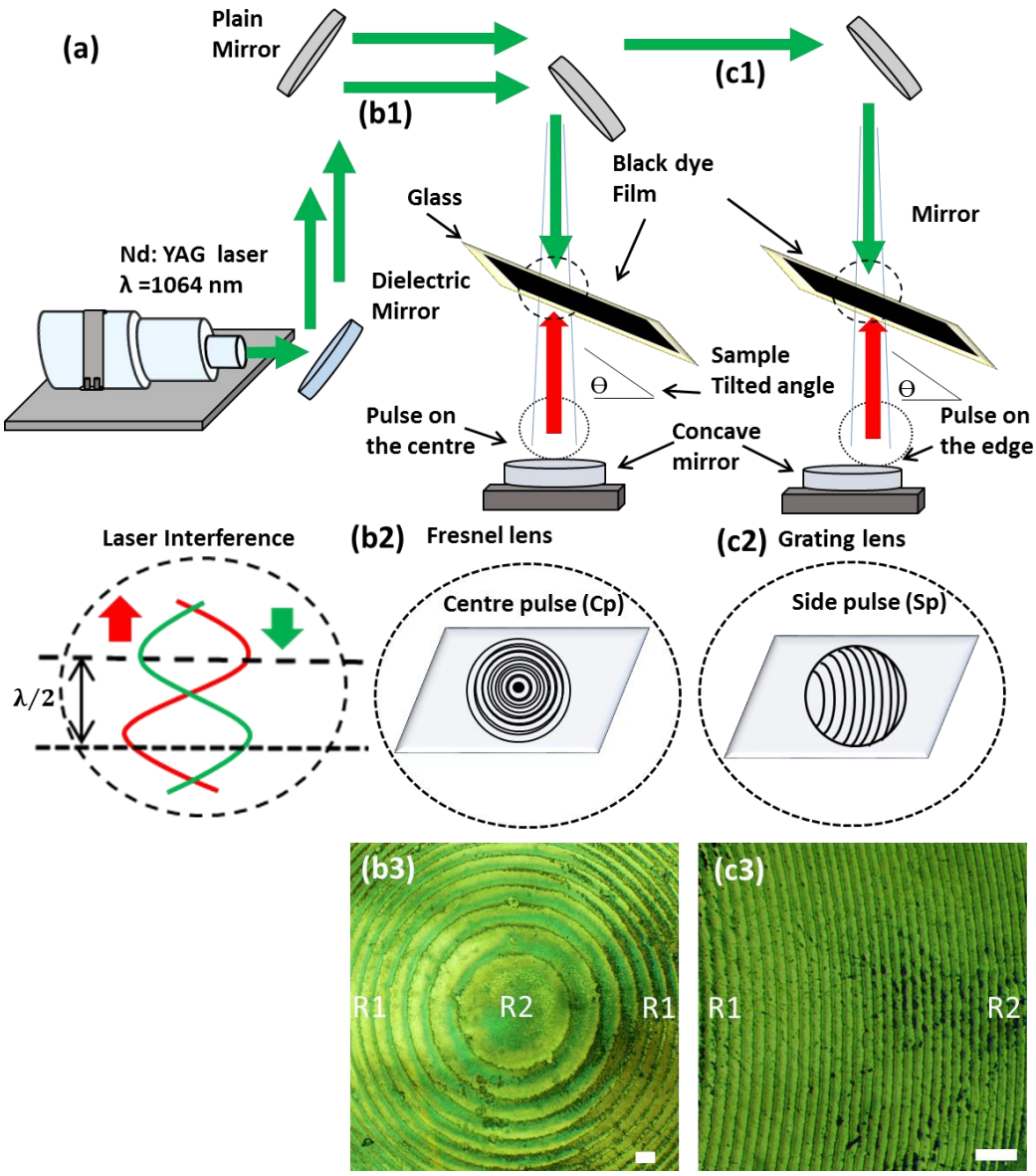

Figure 6.1: Fabrication of Fresnel lens and distorted nonpatterns of nanosecond DLIP in holographic Denisyuk reflection mode: (a) Nd:YAG laser beam (1064 nm, 3.5 ns) was guided by a dielectric mirror and passed to a set of mirrors through black dye on a glass slide reflected back from (b1), the centre of the concave mirror (centre pulse (Cp)); (b2) Fresnel zone plate representation; (b3) optical image of the fabricated Fresnel lens plate. The second set of mirrors: (c1) exposure from the side of the concave mirror (side pulse (Sp)); (c2) displacement structure representation; and (c3) optical displacement structure. (scale bar = 100 µm)

The interference of the laser ablation process resulted from two beams. The interference developed from the maximum energy of the incident electric laser wave E_I and reflected electric laser wave E_R:

$$E_I = E_I \sin(\omega t + \alpha_I) \quad \text{(Eq. 6.2)}$$

$$E_R = E_R \sin(\omega t + \alpha_R) \quad \text{(Eq. 6.3)}$$

$$E^2 = {E_I}^2 + {E_R}^2 + 2E_I E_R \cos(\alpha_R - \alpha_I) \quad \text{(Eq. 6.4)}$$

where λ , x, ω, and t represent the laser wavelength, axis plane, angular velocity and time respectively. In addition, *k* is the magnitude of the grating vector or the propagation number and can be calculated by $k = 2\pi/\lambda$. The separation of space and phase is defined by α (x. , ε) = - (kx+ ε). The phase difference is represented as a sign by δ = $(\alpha_R - \alpha_I) = 2\pi/\lambda(x_1 - x_2)$ [148].

The holographic DLIP has produced the Fzp and (CG) structures by arranging the samples' angle at 0^0 during the interference. The result of the phase grating made both the structures have different spacings. Optical microscope images were used to measure the average large structure (R1) and the average smallest periodicity structure (R2) in every sample (spacing in central and side regions labelled in Figure 6.1(b3-c3)). The centre pulse (Cp) made the symmetric Fzp structures and it had no structure at the midpoint which was considered as R1 with zero periodicity. While it showed the structure spacing of R2= 12.1μm Figure 6.2(c1)). On the other hand, the side pulse (Sp) structure showed the spacing of R1= 9 μm centrally, changing to the smallest spacing of R2= 5.6 μm in the outer regions (Figure 6.2(s1)). Changing the samples' exposure angle (Θ) on the holographic DLIP allows decreasing of the structure spacing (Λ) [51]. Additional samples are made at the same two incident points of Cp and Sp locations on the concave mirror, with various tilt angles 5^0-35^0. The shape of the Fzp changed after changing the tilted angle to 5^0. It was then not a full circle as the Sp structure. Increasing the tilted angle also decreased the structure periodicities (Figure 6.2(c2)). While the same exposure angle of the Sp decreased the curve structure and the spacing to R1= 3.44 μm and R2= 3.39 μm (Figure 6.2(s2)). In addition, the resultant difference of the structural spacing of (R1 and R2) for both laser pulses (Cp and Sp) became very close at around 25^0 (Figure 6.2(c3)

- 6.2(s3)). The full experimental microscope images of the Cp and Sp patterning structures are provided in (Appendix Figure 6S13-14). The Eq. 4.5 was used to estimate the theoretical mean values of the structural spacing with the exception of 0^0 angle exposure. The Cp structures' mean values were closer to the theoretical values than the Sp structures' because the concave mirror surface changed gradually from the centre to the edge. While the Sp nanostructures started from a side region of the uneven surface to produce smaller spacing than the Cp structure. Both laser reflection positions of Cp and Sp started to match periodicity with the theoretical spacing values at 20^0 because both reflected from an almost similar size of reflection area on the mirror (Figure 6.2(d4)). The experimental and theoretical structures' spacings are provided in (Table 6.1). Transmitted measurements were conducted on all structures to study the space light interactions (Figure 6.2(c4-s4)).

As a result, the holographic DLIP generated different structures' spacing. The grating periodicity can be managed by controlling the sample exposure angles and beam reflection area from the concave mirror. Transmission measurement decreased as the structure periodicity became smaller. The produced patterning structure considered as non-linear structures.

Table 6.1: Periodicity measurement black dyes based on the changing exposure angle; C: pulse on the centre; S: side pulse; R1: smallest regen grating; R2: largest regen grating; Theo: theoretical spacing.

Tilt ang .(°)	C-R1 (µm)	C-R2 (µm)	S-R1 (µm)	S-R2 (µm)	Theo. (µm)
0	0	12.1	9.0	5.6	-
5	7.1	4.9	3.57	3.2	6.1
10	3.52	2.95	2.55	2.2	3.06
15	2.1	1.76	1.74	1.63	2.06
20	1.65	1.5	1.32	1.23	1.56
25	1.23	1.16	1.17	1.12	1.26
30	1.05	1.0	0.96	1.00	1.06
35	0.92	0.9	0.90	0.88	0.923

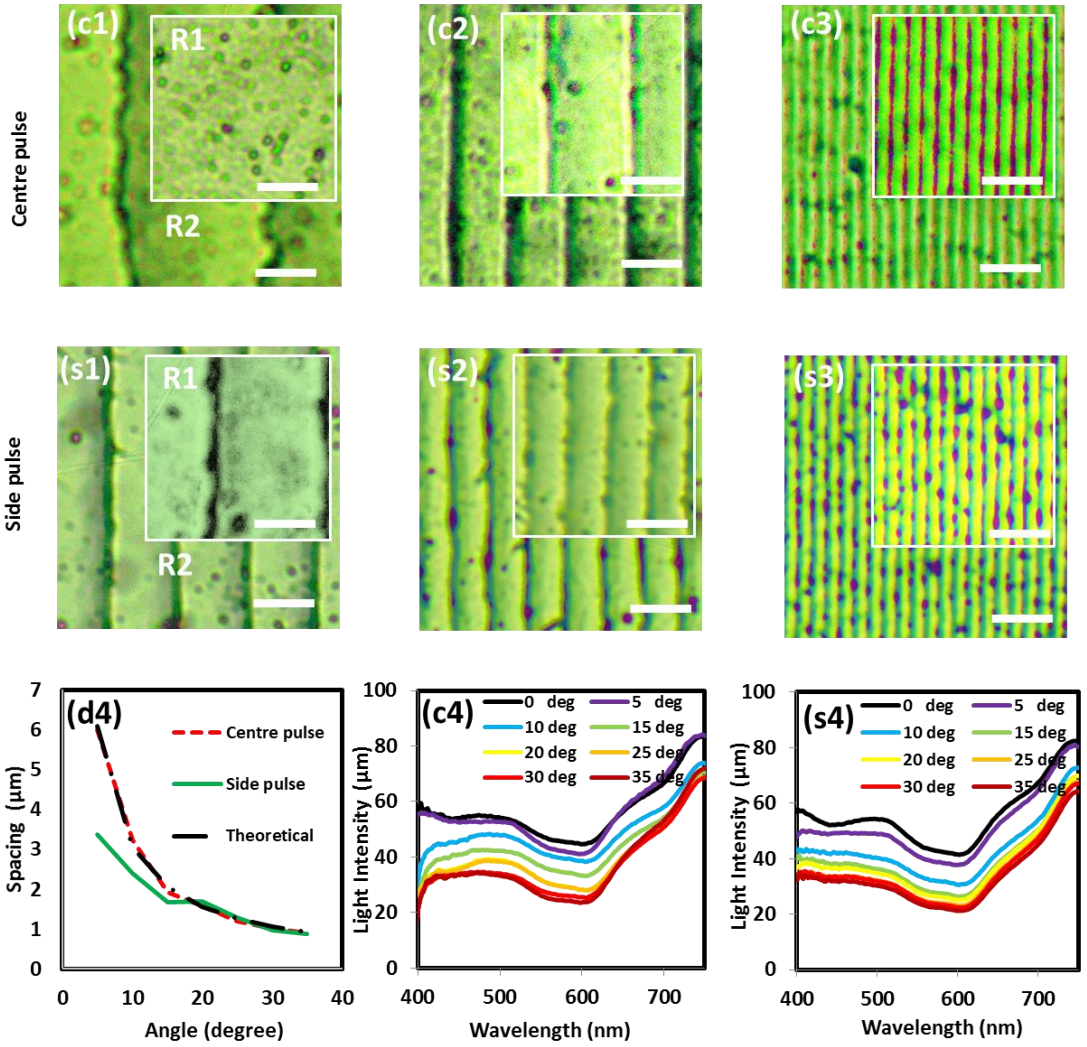

Figure 6.2: Optical microscopy images showing surface grating nanostructures fabricated by holographic DLIP reflection from the centre and the side of a concave mirror. The effect of changing the laser amplitude due to the reflection and samples' tilted angle on the structures' spacing (the smallest regen R1 - the largest regen R2 periodicities): (c1) $\mathbf{0^0}$ (0 µm-12.1 µm); (s1) $\mathbf{0^0}$ (5.6 µm-9 µm); (c2) $\mathbf{5^0}$ (4.9 µm-7.1µm); (s2) $\mathbf{5^0}$ (3.39 µm-3.44 µm); (c3) $\mathbf{25^0}$ (1.16 µm-1.23 µm); (s3) $\mathbf{25^0}$ (1.12 µm-1.17 µm). Tilted angle effect on structures' spacing of (d4) Cp, Sp and theoretical; (c4) transmission on Cp structures ;(s4) transmission on Sp structure; scale bar = 5 µm.

6.4.2-Optical characterization of the structure

Analysis with experimental laser illumination from three monochromatic light sources blue, green and red wavelengths (450 nm, 532 nm and 635 nm) was conducted on the patterned structures. The red laser beam illumination (635 nm) on the nanopatterning was used as the

main diffraction analysis because it has a large wavelength to generate large diffraction angles [52, 149, 187]. The spacing produced at various tile exposure angles (5^0 to 35^0) influenced the diffraction angles to increase for both Cp and Sp pattern structures [61, 110, 187]. Although the diffraction was asymmetric with one side diffraction intensity being higher in the first order than the other one in all the structures (Figure 6.3(c1-s1)). The positive orders were less intense because the diffraction was affected by the direction of the curved structures, producing highly intense focal points (f_o) on one side and defocused low intensity spots on the other side [189]. In addition, the light intensity reduced as the diffraction angle increased. As the structure spacing reduced, the diffraction intensity decreased (Figure 6.2(c4-s4)) [112, 189, 193]. The intensity of the Cp structures was higher than the Sp, especially in the larger spacings. Moreover, there were more diffraction points at the Cp structure than at the Sp structure. On the other hand, the diffraction angle of the Sp structure was higher than for the Cp structure. The difference in the intensity and the diffraction angle also resulted from the size of the structure spacing (Table 6.1). The full experimental diffraction graphs of the Cp and Sp patterning structures are provided in (Appendix Figure 6S15-16). The diffraction angle and the focal points could also be estimated based on the structure size (Eqs 4.6-6.5) and the theoretical and experimental diffraction point is presented in (Table 6.2).

$$f_o = \frac{r^2}{2mW} \qquad \text{(Eq. 6.5)}$$

Where the m, α, $f_{o,}$ r and W are the order number, diffraction angle, focal points' radius of the grating aperture and defocused power [112, 194].

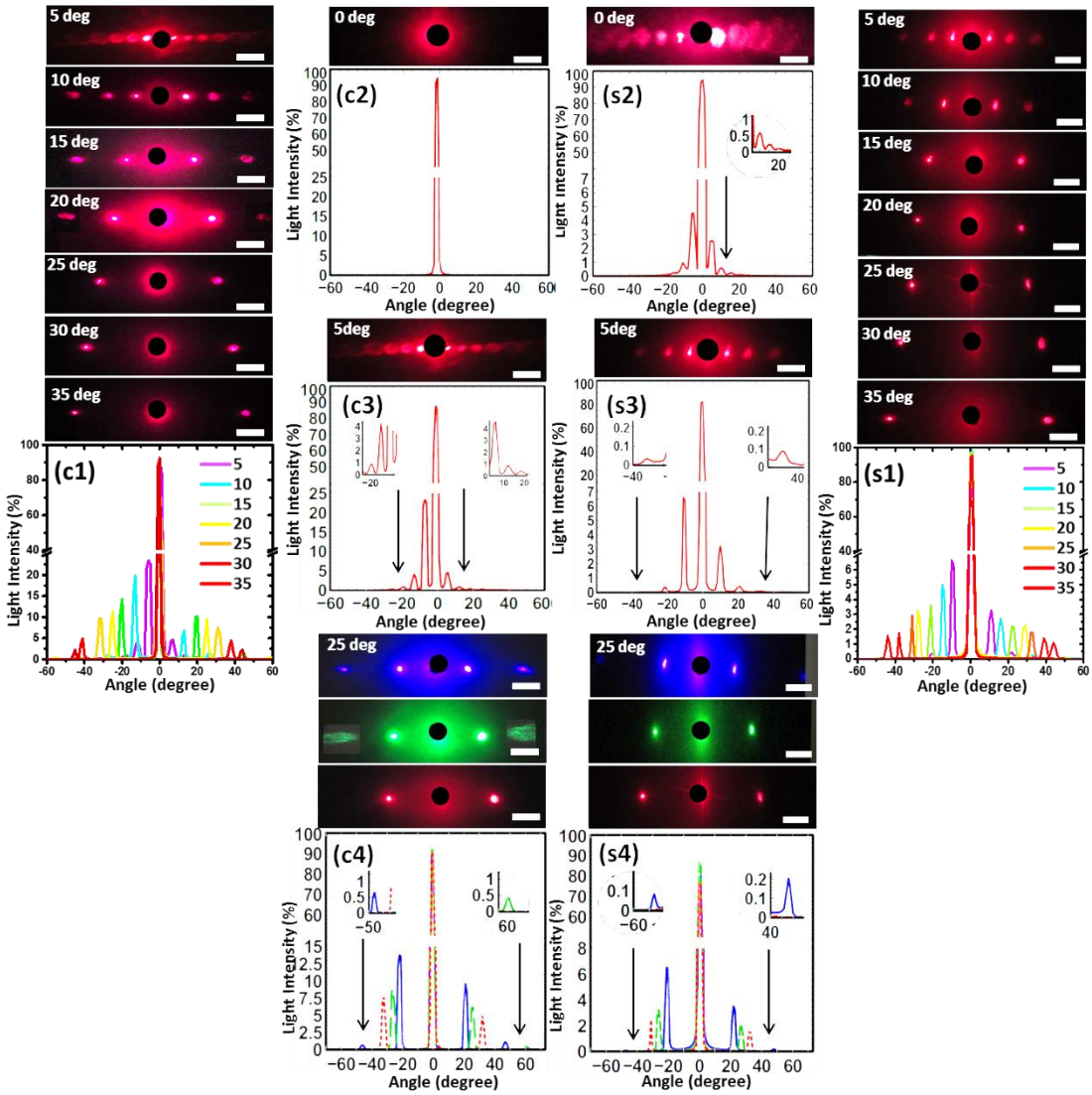

Figure 6.3: Experimental diffraction from nanostructures of varying periodicities produced at tilted angle of $\mathbf{5^0 - 35^0}$, via central pulse (c1); and side pulse (s1). Diffraction from $\mathbf{0^0}$ samples with (c2) symmetric Fzp circles and (s2) asymmetric curve structures. Red laser illumination on a $\mathbf{5^0}$ (c3) centre structure; (s3) side structure. Diffraction results for 450 nm, 532nm, and 635 nm wavelengths with $\mathbf{25^0}$ tilt angle sample (c4) centre pulse; (s4) side pulse; scale bar = 5 cm.

In addition, the diffraction of the Cp and Sp at 0^0 had different behaviours. The Cp structures made one diffraction point based on a full symmetric circle structure (Figure 6.3(c2)). Although it has many differently sized circles which can generate different focused orders (f_z), all of them are focused on the centre based on the radius size and the illumination wavelength (Eq. 8) [195, 196]. Similarly, the Sp structures are able to focus on the centre (Figure 6.3(s2)). Although, it has many diffraction points, none of them can be as focused as the one on the

centre (based on many experiments). The extra diffraction points could also be approximated by Eq. 4.6. When the exposure angle changed to 5^0, both the patterning structures focused in the first order (Figure 6.3(c3-s3)). Even though the zero order seemed to have higher intensity than the first order, it would shift. Further analysis is considered on 25^0 Cp and Sp structures by the three laser wavelengths. The diffraction angle of the low wavelength was less than for the higher wavelength[51]. However, the short wavelength illumination (450 nm) has a higher intensity than the 532 nm and 635 nm for both pulse structures (Figure 6.3(c4-s4)).

$$f_z = \frac{r^2}{m\lambda} \qquad \text{(Eq. 6.6)}$$

The spacing and the shape of the Cp and Sp structures influenced the diffraction angles and intensity to make one side focus and the other defocus; although the diffraction intensity of the Sp structures was higher than the Cp structures. In addition, if the exposure angle was at 0^0, the highest diffraction point was always in the centre. While the size of the wavelength of the lasers' illumination was able to affect the diffraction angle and intensity.

Table 6.2: Diffraction angle measurement on glass black dyes, based on the changing angle of beam exposure ($\mathbf{5^0 - 35^0}$) of the samples, and comparison between experimental and theoretical results at centre pulses and side pulses.

Tilted angle (°)	C-Diff. angle(°)	C-Theo.diff.angle(°)	S-Diff. Angle(°)	S-Theo. diff.Angle(°)
0	0	0	2	3
5	6	6	10	10.8
10	13	11	15	15
15	19	19	21	22
20	25	24	28	29
25	31	32	32	33
30	38	38	38	40
35	44	44	44	45

6.4.3- Focusing analysis

Further analyses demonstrate the benefits of curved structures. The 25^0 tilted samples of the Cp and Sp structures were selected as a string with very close agreement between the diffraction and the structures' spacing. Using a white screen arranged at the first distance of 18 cm from both the samples and maintaining an image distance at 20 cm, the screen's distance was decreased by 3 cm in six steps. The last step's distance was 1 cm, as the closest possible point to the sample. Although the images of the first order diffraction spots seemed to move closer to 0 order, all spots moved along one diffraction angle, which was 31^0 for the Cp and 32^0 for the Sp structure (Figure 6.4(a-b)). The spot size of the diffraction points was decreased as they moved closer to the illumination source. The light intensity of the spots were the lowest at 18 cm in the both samples and increased as they moved closer to the laser illumination source. However, the Cp and Sp structures gave the highest intensity at 3 cm distance at the focused point, then decreased to 2 cm from the samples. The Sp structure's intensity seemed to be higher than the Cp structure between 2 cm and 3cm because of the small difference in the spacing (Figure 6.4(c)).

Another structure was used to add important analyses of focused diffraction intensity (non-linear structure) [110, 149, 189]. The 5^0structure of the Cp has been used as one with the highest diffraction points compared to the other structures. The same analysis of moving the screen was used. The intensity of 0 order was low at 18 cm screen distance and for several steps. Then the first order (-1) reached the maximum intensity at 12 cm distance; then it decreased near the illumination source (Figure 6.4(d-e)). A comparison between the negative and positive diffraction intensity points was added to show the full change of diffraction intensity at every point at different distances (Figure 6.4(f-g)).

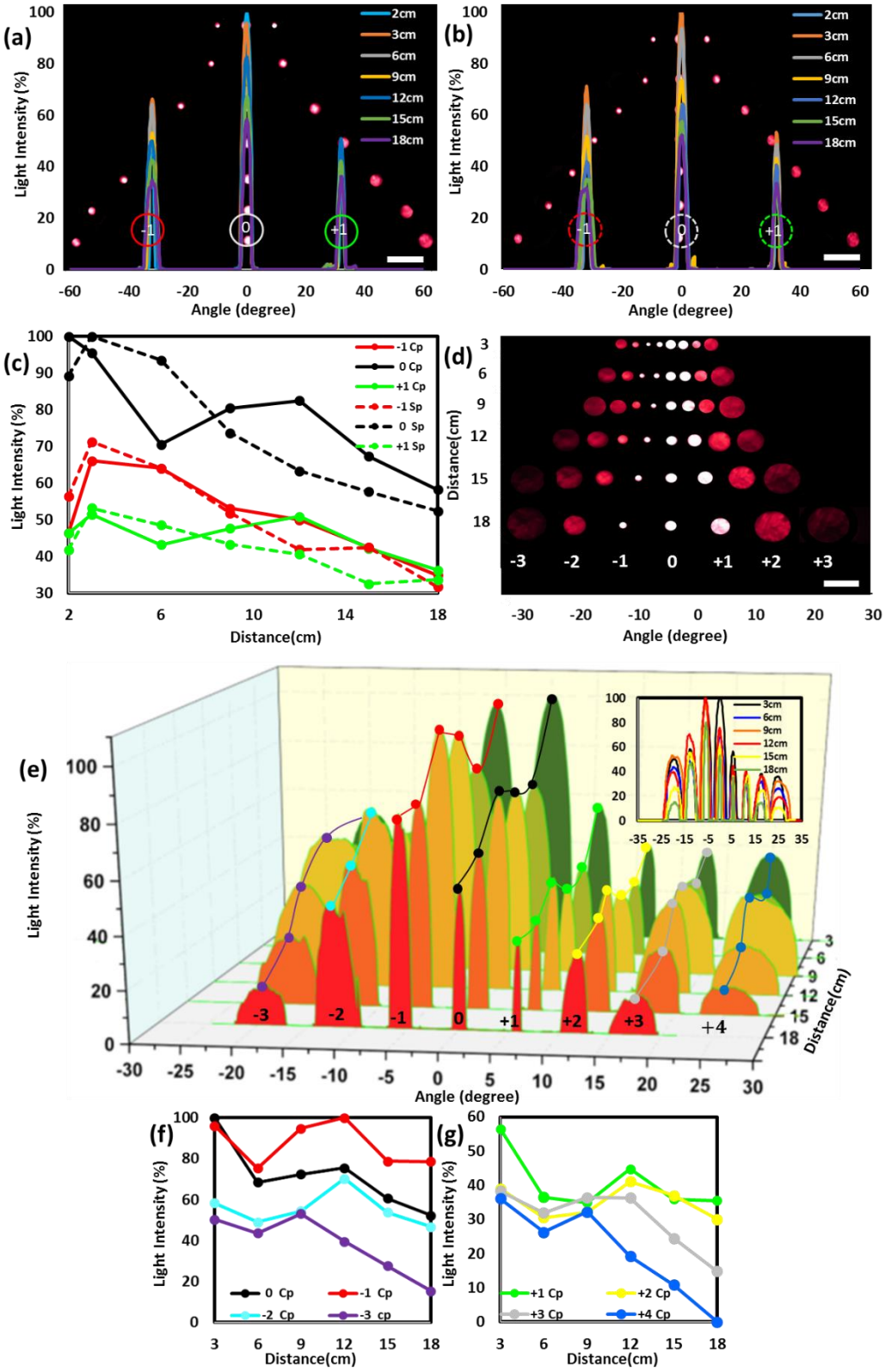

Figure 6.4: Changing distance of the measured diffraction patterns from $\mathbf{25^0}$tilted angle samples (a-b) central pulse structure and side pulse structure; (c) two pulse structure comparison. Changing screen distance for a centre pulse $\mathbf{5^0}$ sample ; (d) image of diffraction at different distances. Red laser illumination for $\mathbf{5^0}$ tilted angle sample (e) graph for changing distance and resultant diffraction intensity; (f) left side of diffraction points; and (g) right side diffraction points; scale bar = 5 cm.

The Cp and Sp pulse structures at 25^0 showed equal and low diffraction intensities in the first order at 18 cm distance, then reached maximum diffraction intensity around 2-3 cm at the focused points. The Sp structure had lower intensity than the Cp structure; then it is increased due to the focus point and spacing. On the other hand, the 5^0 structure showed maximum intensity in the first order at 12 cm to the focus point, before it returned to the main source position at the centre of 0 order. As a result, the distorted nanostructure was influenced by the size of the structure, to create the maximum intensity at the focus point; which can be used as a strong signal to detect any change of movement or surface shift.

6.4.4-Spectrum rainbow diffraction measurement

A goniometer set-up was used to measure the angle-resolved diffraction efficiency. The set-up was able to measure the rainbow diffraction wavelengths from the nanostructures, as it moved on the motorized rotated stage (Figure 6.5(a)). The grating rainbow diffraction covered the wavelengths between 400-800 nm. The samples were placed about 17 cm from the spectro meter detector. The length measurements were based on placing a screen at 35 cm away from the diffraction samples. The white light showed different responses when transmitted through both the Cp and Sp pulse structures. The Fzp structure allowed all the wavelengths to emerge together towards one focus point; because the structure had a composition of several sized full circles and acted as a lens [110]. However, the CG showed some diffracted wavelengths because the structure has multiple semi-circle structures and acts as a grating. The Cp structures started to diffract different orders on both sides between 5° to 15°; then diffraction became one order on both sides between 20° to 35° (Figure 6.5(b)). The rainbow diffraction was measured for all structures from 0° to 35° tilts of Sp patterning (Figure 6.5(c)).

The curved nanostructures have more visible wavelength intensity on the left side than the right side, due to the curve direction making it focused on one side. The goniometer set-up was used to analyse the 25° sample produced via Cp and Sp. The wavelength diffraction profiles are the same on both sides (Figure 6.5(d)). The right-side rainbow length was 7.4 cm and the left side was 13.4 cm. On the other hand, the length of the left and right sides of the Sp were 5 cm and 10 cm respectively (Figure 6.5(e)). This showed a good focus of the wavelength on one side (right); although the intensity of the Sp was less than the Cp patterning. This is because the focus point of the Sp patterning was shorter than the Cp patterning due to a difference of structure size.

The Fzp, Gd, Cp and Sp structures diffracted all wavelengths. The distribution of the rainbow patterning increased as the structures' size decreased. The Cp and Sp structures have strong wavelength intensity at the right-hand sides because they were the focused sides. The Cp structure has a high wavelength intensity because the focus point was a longer distance than the Sp patterning. More length of rainbow patterning could help to deliver more information, but it would then be closer to the source of light and at a high angle.

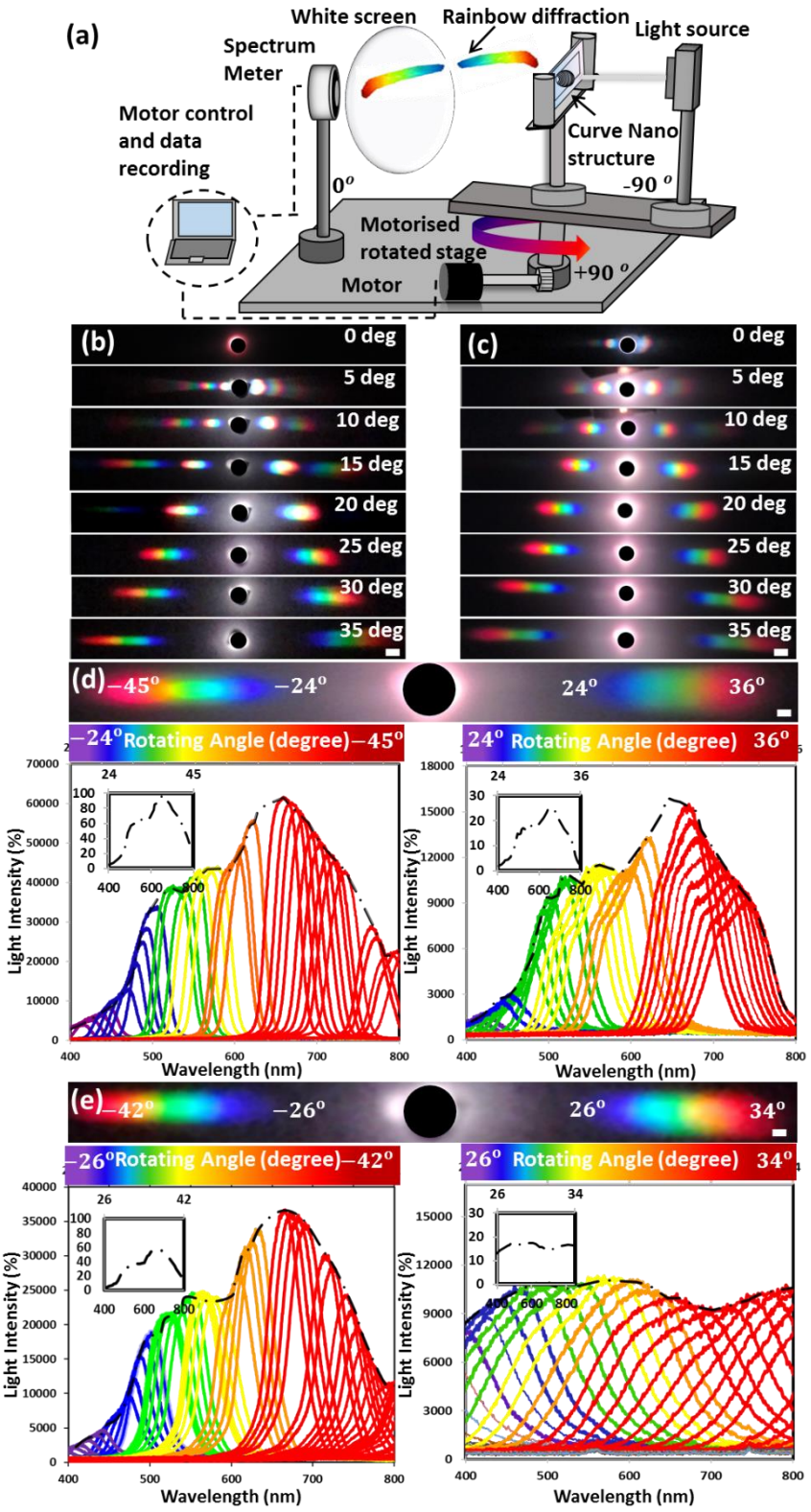

Figure 6.5: Angle-resolved measurements of fabricated patterning structure by holographic DLIP: (a) the spectroscopy system to analyse a white light diffracted beam through a sample on a motorized stage to measure the rainbow pattern. The rainbow structure diffraction pattern for (b) centre pulse samples produced at 0° to 35°; (c) side pulse samples at 0° to 35°. Lift and right rainbow diffraction of 25° structure: (d) centre pulse patterning, and (e) side pulse patterning; scale bar = 1 cm.

6.5- Applications of the curved nanopatterning structure

6.5.1- 1D/2D curved nanopatterning structure

The second stage of the experiment involved curved structures on a number of applications. Instead of using a glass slide a low-cost commercial tape was selected to deposit the nanostructure upon. It was chosen based on many advantages, such as having a good adhesive layer, strength, flexibility, being waterproof, fully transparent and having stretch-ability. The thickness of the tape was 100 µm. The black dye was deposited on the tape with the same thickness. A holographic DLIP laser was used to generate 1D nanopatterning at a 35° exposure angle (900 nm x 880 nm) (Figure 6.7(a)). The 2D structure was designed by a sample rotation of 90° to make the same spacing in the x and y axis (900 nm x 900 nm and 880 nm x 880nm) (Figure 6.7(b)) [51, 52]. Transmission mode was used to measure the material surface thickness on the tape before and after the nanostructure. The halogen light was used for transmission analysis with reference to a plain tape. The plain tape showed high transmission reaching about 98%, but the transmission decreased to 18% with black dye coating.

The transmission increased on the 1D and 2D nanostructures. The 2D curved structure showed a higher wavelength transmission than the 1D due to more material removal and increased transparent structure gaps (Figure 6.7(c)). The hydrophobicity measurement was conducted to measure the change in the tape's surface properties (contact angle) in response to 1D and 2D nanostructures respectively (Figure 6.7(d-f)). In addition, the three wavelength illumination were used to show the diffraction from the 2D structure. In addition, the three wavelength illuminations were used to show the wavelength interaction on the 2D structure. They showed an increase in diffraction angle on both axes as the wavelength increased (Figure 6.7(g-i)).

Moreover, 2D patterning generated two rainbow diffractions patterns on both axes (Figure 6.6(j)). In addition, the RGB room light measurement on a 1D 35° tilt angle structure showed a visible wavelength change from blue to red as the structure was exposed to the light source normally. The curved nanostructures altered 0.3^{o} to 14.2^{o} to show a visible change which could be used as an indication of wavelength change (Figure 6.7(k)). Furthermore, the black dye nanostructure was tested in DI water at different pH concentrations to show stability with pH (Figure 6.6).

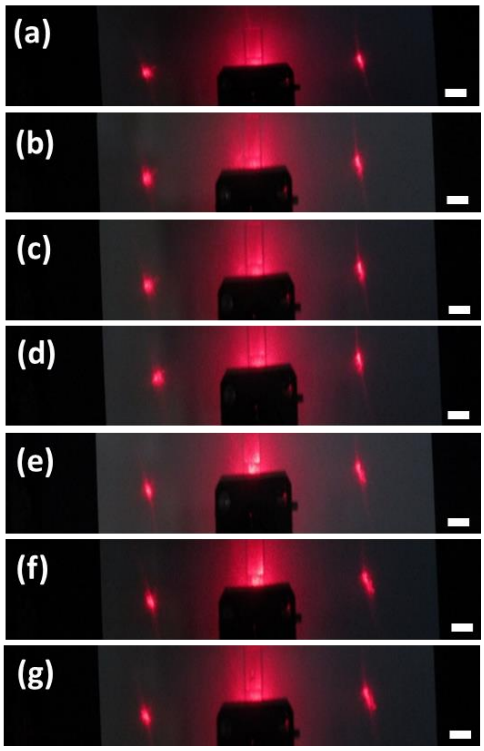

Figure 6.6: Holographic 1D (0.9 µm) nanopatterning structure via measurements diffractive angle of pH concentrations (a)5.0, (b)5.5, (c)6.0, (d) 6.9, (e) 7.4, (f)7.8, (g)8.2.(scale bar=5 cm)

The plain tape, 1D and 2D structures showed a change of transmission and contact angle. Moreover, the 2D structure showed the diffraction angle and rainbow patterning with an extra spot at the y-axis. The 2D structure could help to detect the elongation change from the two axes. The visible wavelength of the 1D structure based on the changing sample tilting was able to add more information. The black dye structure was stable with the pH change.

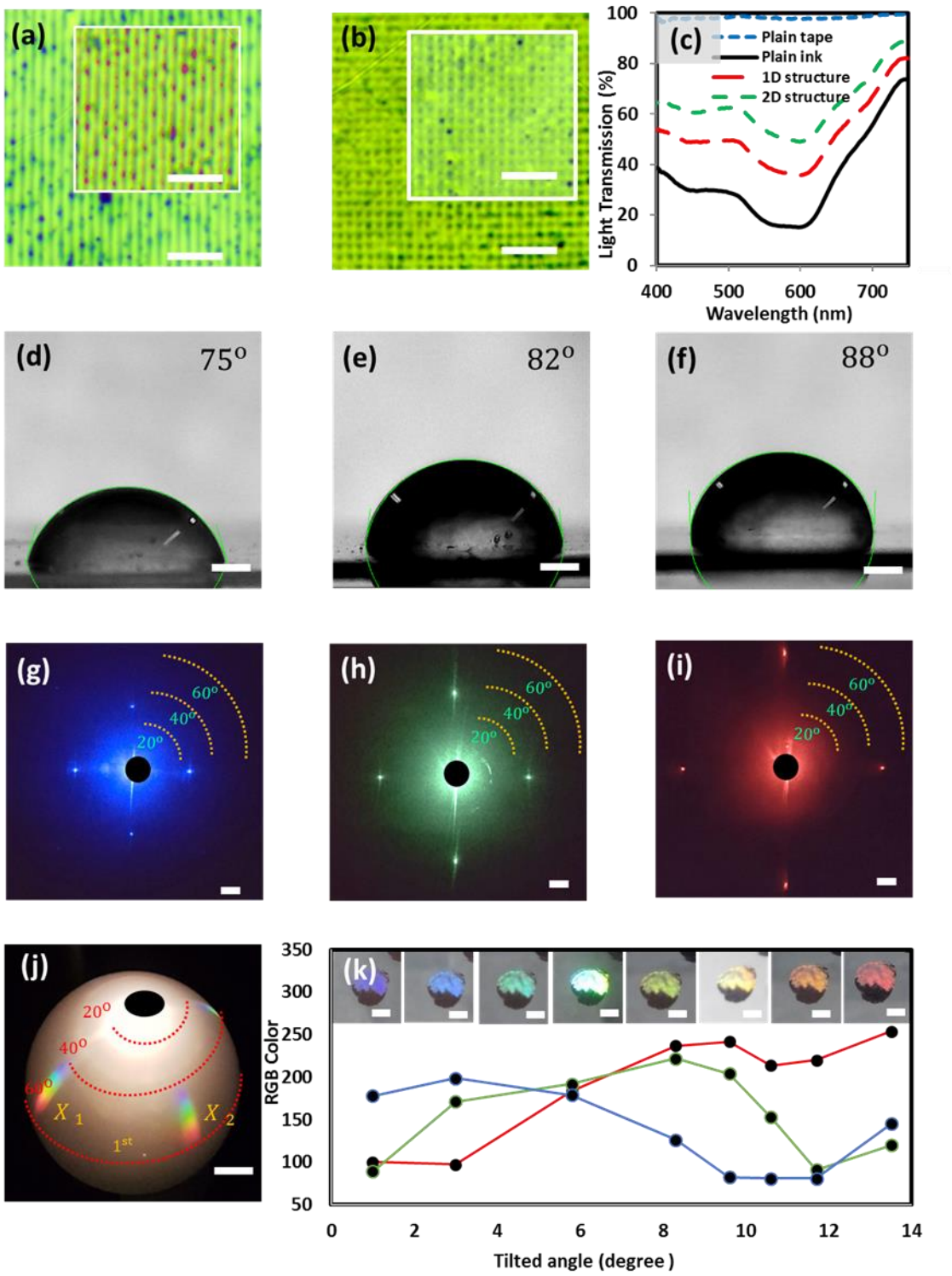

Figure 6.7: Fabrication of 1D and 2D curved nanopatterns using holographic DLIP. The larger and smaller structure periodicity were (a) 1D (0.88 µm-0.90 µm); (b) 2D (0.90 µm-0.88 µm x 0.88 µm x 0.9 µm); (c) transmission analysis; scale bar = 5µm. Contact angle measurements of (d) plain tape; (e) 1D structure; (f) 2D structure; scale bar = 1 mm; laser illumination of (g) 450 nm; (h) 532 nm; (i) 635 nm). Rainbow diffraction of (j) 2D pattern sample; visible colour analysis of (k) a 1D pattern sample using room light. (scale bar = 1 cm)

6.5.2- Elongation sensing, imaging and holographic logo

The 1D Sp structure made at 35^o on adhesive tape was used on a strain measurement set-up (Figure 6.8(a)). The illumination was started with a diffracting angle of 44°. The tape would be stretched to analyse the intensity and the diffraction angle variation. The main testing would measure the diffraction angle on the focused point side. The strain test was conducted on the tape of 4 cm length and 1.5 cm width to measure the Young's modulus of the tape. The tape has ductile behaviour (Figure 6.8(b)), with an elastic limit of 1.3 N/cm^2 and Young's modulus of 36.7 N/cm^2. Then the tape started to yield in the plastic zone at the Young's modulus 13.3 N/cm^2 and 4.6 cm (Figure 6.8(c)). The elongation was conducted with the set-up by elongating the tape of 0.6 cm more than 300 stretches to detect 5 με of each elongation alteration. Seven points were selected to expose the diffraction change positions (Figure 6.8(d)). The intensity increased as the stretching increased, because the gap spacing increased to allow more light to focus at a longer distance. The change of diffraction position could measure the change of the elongation. In addition, it could provide control of the focal length based on an extension of the tape.

6.5.3-Imaging and holographic logo

Further application can be used from curved nanopatterning. Using a lens behind the Fzp, CG, and 5° of the Cp structure were used for imaging as the largest structures. The structures would modify efficiently the focal length of the lens (Eq. 6.7) to make multiple images based on the structure size (Eq. 6.8) [112, 118].

$$f_{lens}=[1-n](\frac{1}{r_i}-\frac{1}{r_o})\frac{(1-n)d}{r_i r_o n}) \quad \text{(Eq. 6.7)}$$

$$f_{img}=\frac{f_{lens}\, r^2}{r^2+2f_{lens}\, mW} \quad \text{(Eq. 6.8)}$$

Where n, r_i, r_o, d represent the lens refractive index, inner radius, outer radius and lens thickness. The Fzp and Gd have shown single images on the zero order (Figure 6.8(e-f)). While the 5° of the Cp structure showed more than one image. Although, it was supposed to show the focus point on the left of the first order (-1), it showed the main image at zero order and the first order. This is because the screen was at 15 cm which is out of focus for the first order. The screen was kept in one position to expose the same parameters for all images. In addition, the 5° of the Cp structure was exposed to three illumination lasers (Figure 6.8(h-j)). Moreover, holographic DLIP with continuous pulses at a sample tilted angle of 35° was used to produce a nanostructured BHAM pattern on the tape. Holographic logo can be visualised from normal room light and used as a flexible holographic structure. It can be transferred to other surfaces and it can also be employed for security uses (Figure 6.8(k-m)). Additional 2D holographic curved nanostructures were produced with different sizes of the x and y axes. The curved nanostructures have a large structure side for imaging and a small spacing side for sensing (Appendix Figure 6S.17).

Using the holographic DLIP to generate a curved nanostructure on an adhesive tape could transfer it to the flexible strain sensing to attach to different types of surfaces. The curved structure can increase the intensity as the stretching increases, to emphasis a stronger alert signal during structural damage. The size of the spacing of the curved nanostructure and the length of the tape are the main controllers to increase or decrease the response of the elongation change. The Fzp, Gd, and 5° of the Cp structure are able to provide imaging for the target surface. In addition, the light wavelength could affect the focus distance of the point to provide better details to the target surface.

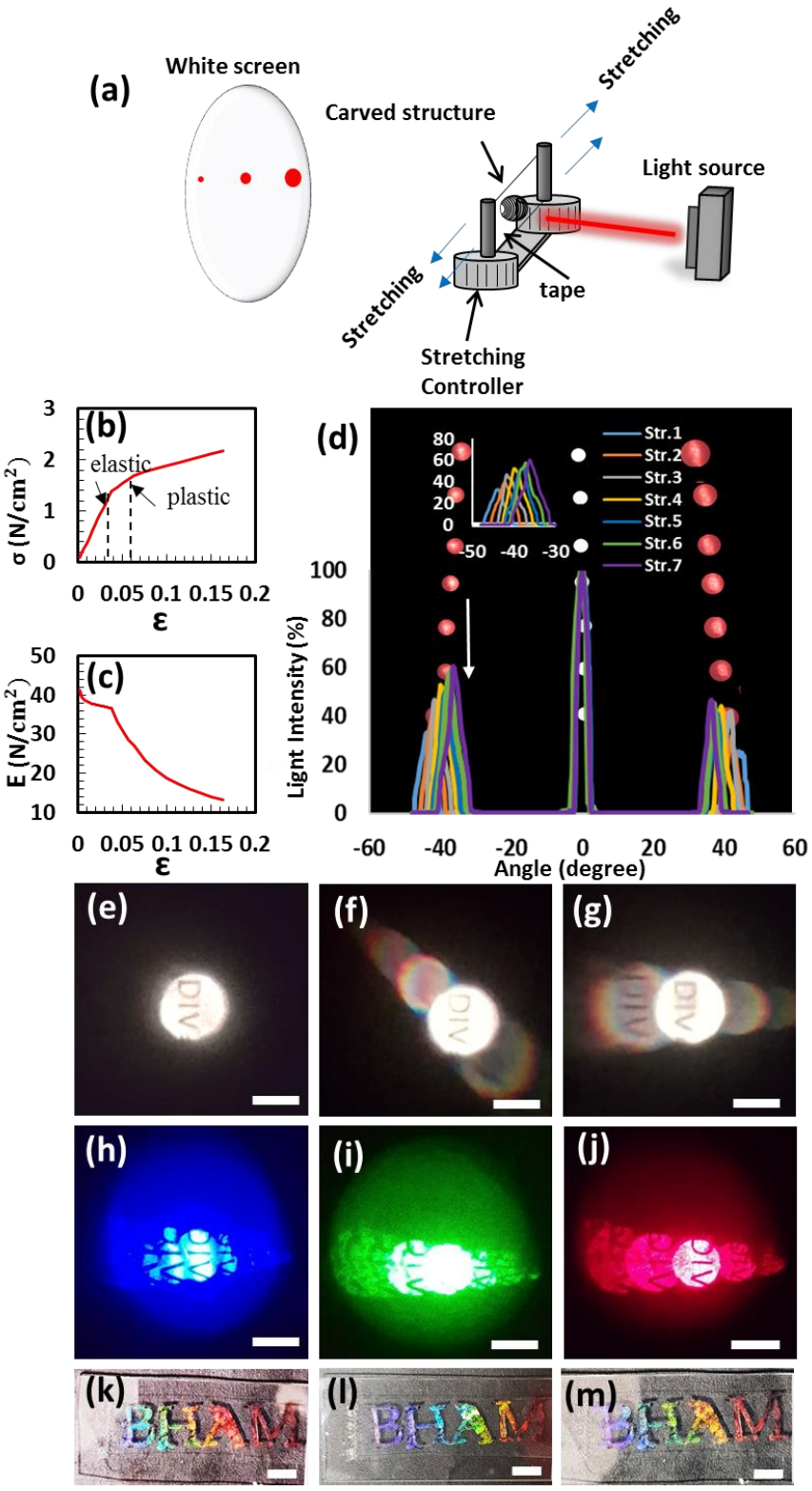

Figure 6.8: Curved nanostructure on a tape for elongation measurement and applications (a) stretching set-up; mechanical measurements of tape, (b) elastic and plastic deformation, (c) Young's modulus; curved nanopatterning on tape, (d) stretching diffraction measurement; imaging by white source nanostructure, (e) Fresnel lens, (f) grating displacement, (g) centre pulse at $\mathbf{5^0}$; imaging with monochromatic light through $\mathbf{5^0}$centre pulse structure:(h) 450nm, (i) 532nm, (j) 635nm); holographic curved nano surface grating of (k-m) BHAM logo; scale bar = 1 cm.

Moreover, the curved nanostructures could provide a visible sensors under simple room light. The holographic BHAM curved nanostructure not only could be used for a transferable visible commercial logo, but also could provide a security hidden light key. Additional 2D holographic curved nanostructures were produced with different sizes of the x and y axes. The curved nanostructures have a large structure side for imaging and a small spacing side for sensing (Appendix Figure 6S.17).

6.6-Conclusion

Depositing a synthetic black dye on stretchable tape allowed the formation of nanogratings on a surface by a pulsed Nd:YAG laser. The holographic DLIP produced Fzp and Gd and it was able to produce different curved structures spacings by changing the sample exposure angle. The spacing of the structures would modify the focal length distance. Moreover, the short wavelength is able to focus at a longer distance. Controlling the curved structure spacing could help to control the intensity, diffraction and visual image. In addition, adding a lens behind the Fzp or large curved structure could help to deliver live images of the targeted structure. The 35° Sp nanostructure on the tape was use for measuring the elongation change for strain sensing. The 2D curved structures could help to measure the surface changes in two axes. A visible colour change of the curved structure could add more information. The black dye nanostructure on the tape was stable in different pH concentrations. The curved structure was able to amplify the light intensity, as the stretching increased to indicate any significant change in geometry. The structures' spacing and the length of the tape are the main parameters to increase or delay the light signal from any material damage and shifting. For these reasons a low-cost curved structure on the tape enabled the sensing of any possible dynamic elongation and provided images for the target surface, to avoid any catastrophic incidents.

Chapter 7: SUMMARY AND FUTURE WORK

7.1-Introduction

The researches objectives were achieved by using holographic DLIP in the Denisyuk reflection mode to fabricate nanostructures. The holographic DLIP is able to produce fast low-cost 1D/2D nanopatterns and thus to address major deficiencies of lithographic methods for a range of applications. Studying the holographic DLIP system and trying to improve the control of the spacing and shapes of the nanopatterning structures was very valuable research. The investigation and analysis of nanostructures could help to make some improvements for optical applications. Nanotechnology research needs to drive important possible solutions for normal and challenging problems to human health, safety and daily needs. A number of industries require simultaneous technology improvements with highly precise measurement facilities at a low cost, to improve their products' quality. Therefore, in order to deliver all these outputs, this thesis experimentally investigated the nanopatterning structures for optical applications. The outcome of using holographic DLIP strategy in our research was two types of optical sensors. In addition some of the optical applications were introduced as personal security signatures, holographic logos, filters, Fresnel lens and surface imaging structure. Furthermore, other future projects are proposed.

7.2-Summary

Periodic nanostructures and photonic structure materials are needed in nanotechnology for numerous optical applications. Their use provides an innovative and significant path to solve some important and intricate problems in humans' everyday live. This thesis delivers the procedure of holographic direct laser interference patterning (DLIP) as a nanofabrication process that can reduce cost, time and is flexible for nano-applications. Holographic DLIP is a single laser beam reflected by a mirror to allow the swift creation of high-resolution multiple laser beams on a target substrate. The consequence of using holographic DLIP strategy in our research can be presented as the following contribution points:

1-Integrating a meniscus lens with a laser in front of a holographic Denisyuk reflection mode system was used to control nanostructure spacing by three parameters: adjustment of a sample exposure angle, the distances between the laser-source sample and mirror-sample distance.

2-Managing the three parameters yielded different nano geometry dimensions of 1D/2D holographic nanostructures.

3-Controlling the nanostructure shapes and periodicities has affected the optical properties.

4-Substrate thickness is imperative because it can influence and increase the efficiency of the diffraction intensity.

5-The holographic Denisyuk reflection mode presented a good approach of fabricating, optimizing and manufacturing a speedy and low-cost nanostructure on thin films.

6-Low-cost ink dyes of four colours based (black, red, blue, and brown) on 915 nm thickness were used in our research which have diverse optical (transmission) properties.

7-They were comparatively thick films associated with the metals' thickness which created them to produce proficient optical properties.

8-The ink dyes were exposed to the holographic DLIP system to generate the same nanopatterning spacing (840 nm) to study the laser relations with surface colour.

9-The thick amplitude grating of the four ink colours created divergent absorption wavelength profiles and different responses with illumination and rainbow diffraction because they have dissimilar refractive indexes.

10-The black ink has the highest absorption among the four dyes; while the brown has the deepest absorption.

11-The blue and red ink nanostructures have the capability to be used as low-cost wavelength-dependent photonic structures; which can be used for displays, fibre optics, and biosensors' applications.

12-The blue and black nanostructures were applied to determine an advanced personal security signature and a holographic logo of the ‘University of Birmingham’.

13-The benefits of the black-based dye’s optical properties for human health applications such as ocular ailments, can decrease healthcare costs.

14-Tears could be applicable as significant indicative information concerning ocular diseases, so commercial silicone-hydrogel contact lenses could be used to identify ocular diseases by incorporating a nanopatterning structure on low-cost commercial contact lens.

15-The deposition of a synthetic black ink dye on the surface of the contact lens permitted the holographic DLIP to format nanopatterning structures.

16-The nanostructures were designated on the contact lens’ edge to avoid any obstacles for human vision.

17-The nanopatterning structures were verified in various environmental forms (dry lens, wet with DI water and wet with artificial tear solution) to show a quick optical response.

18-2D nanostructures were made-up on the contact lens’ surface to enhance the diffraction intensity by more than 10%.

19-Different designs of nanostructures were produced, to prove the hydrophilicity stability of human tears to preserve the contact lens’ softness on the human eyes.

20-The nanostructure has revealed a strong sensing response for changing Na^{+} ions' (±47 mmol L^{-1}) in a human tear to detect the severity of dry eye difficulties at an early stage.

21-The black-based dye's optical properties could be used as tension indicators to monitor and record health circumstances in civil engineering, airspace and human interface applications.

21-The holographic DLIP laser interference reflection initiated the Fresnel lens and curved nanostructures from synthetic black dye on the surface of a low-cost type of commercial adhesive.

22-The nanostructure of the black dye was steady with different pH concentrations and contact angles and could be used for complex systems.

23-The curved nanostructures are non-linear structures and capable of generating light focal points as a strong signal, to offer a reliable, effective response.

24-The size of the wavelength of the lasers' illumination emphasises the focus point.

25-The curved nanostructures on the adhesive tape have shown a robust indication that it is essential to measure surface elongation of 20 με during testing measurement.

26-The 2D curved structures would provide two axes for identifying surface elongation.

27-Attributing a lens behind the Fzp and large curved structures would provide live imaging for the target surface.

28-Tilting the 1D structure within the range of 0.3° to 14.2° could provide visible wavelength changes under broadband light and were used for manageable holographic symbol design.

7.3-Future work

The monitoring of physical changes in the eye needs further investigation and research. Using a holographic nanostructure on commercial contact lenses can be used to report physical changes. Some ocular diseases are associated with intraocular pressure (IOP) due to the build-up of fluids and the geometry of the cornea. Irregular changes in human eyes during illness need to be observed. These symptoms of major ocular diseases, such as glaucoma, keratoconus, diabetic macular edema, and Graves' disease could be monitored to prevent irreversible damage to human eyes. Using the nanostructure on a contact lens could help to report a direct diagnosis of an eye curvature. The early research and experimental results have showed that the nanostructure's spacing on the contact lens decreased during the increase of the curvature (Figure 7.1(a-b)). The diffraction change of the curvature could be used for continuous heath monitoring.

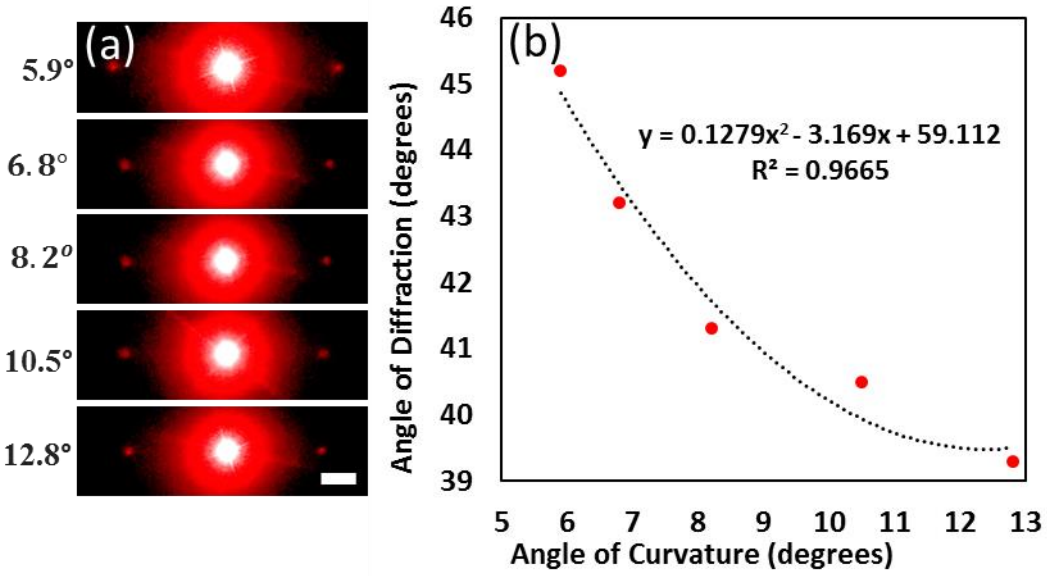

Figure 7.1: Fabricated 1D surface grating nanostructures on contact lens by holographic DLIP to measure curvature change. Red laser illumination (a) curve change; (b) diffraction angle; scale bar = 5cm

In addition, the holographic DLIP has been used to create two types of nanostructure on a contact lens (amplitude and curved structure). The two structures require further research.

A holographic nanostructure made on a rice sheet is shown in Figure 7.2. The holographic nanostructure could be used for food decoration or optical sensing, which requires further research.

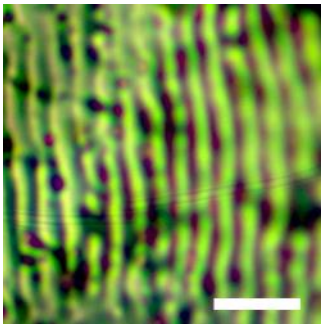

Figure 7.2: Holographic nanostructure on rice sheet. (scale bar = 5μm)

References:

1. Joannopoulos, J.D., Steven G. Joshua N. Meade, Robert D, *Photonic crystals: molding the flow of light,.* Princeton Univ Pr, 2008.
2. Patel, D., R.P. Singh, and R.K. Thareja, *Craters and nanostructures with laser ablation of metal/metal alloy in air and liquid.* Applied Surface Science, 2014. **288**: p. 550-557.
3. Q Zhao, A.Y., CJ Anthony, WR. Fowler, SH Yun and H Butt, *Printable ink holograms.* Applied Physics Letters, 2015. **107**(4): p. 041115.
4. Q Zhao, A.Y., A Sabouri, SH Yun, H Butt, *Printable Nanophotonic Devices via Holographic Laser Ablation.* ACS nano, 2015. **9**(9): p. 9062-9069.
5. Shen Y., Zhou J., Liu T., Tao Y., Jiang R., Liu, M., Xiao G., Zhu J., Zhou Z.-K.,Wang X., *Plasmonic gold mushroom arrays with refractive index sensing figures of merit approaching the theoretical limit.* Nature communications, 2013. **4**.
6. Hou, J., M. Li, and Y. Song, *Patterned colloidal photonic crystals.* Angewandte Chemie International Edition, 2018. **57**(10): p. 2544-2553.
7. Barnes, William L., T. W. Preist, S. C. Kitson, and J. R. Sambles, *Physical origin of photonic energy gaps in the propagation of surface plasmons on gratings.* Physical Review B, 1996. **54**(9): p. 6227.
8. Strong, J., *The Johns Hopkins university and diffraction gratings.* JOSA, 1960. **50**(12): p. 1148-1152.
9. Rittenhouse, D., *Explanation of an optical deception.* Transactions of the American Philosophical Society, 1786. **2**: p. 37-42.
10. Röntgen, W.C., *Über eine neue Art von Strahlen*. 2013: Springer-Verlag.
11. Harrison, G.R. and G.W. Stroke, *Interferometric control of grating ruling with continuous carriage advance.* JOSA, 1955. **45**(2): p. 112-121.
12. Palmer, C.A. and E.G. Loewen, *Diffraction grating handbook*. 2005: Newport Corporation New York.
13. Chou, S.Y., *Nanoimprint lithography and lithographically induced self-assembly.* Mrs Bulletin, 2001. **26**(7): p. 512-517.
14. Mack, C.A., J. Sheats, and B. Smith, *Optical lithography modeling*. 1998: Marcel Dekker, New York.
15. Cromer, C.L., Lucatorto, T.B., O'Brian, T.R. and Walhout, M., *Improved dose metrology in optical lithography.* 1996. **39**(4): p. 75-79.
16. Geppert, L., *Semiconductor lithography for the next millennium.* Ieee Spectrum, 1996. **33**(4): p. 33-38.
17. Gilbert, G., Hamrick, M., Weinstein, Y.S., Pappas, S.P. and Donadio, A., *Quantum sensor miniaturization prospectus*. in *Quantum Information and Computation VII*. 2009. International Society for Optics and Photonics.
18. Mao, F., Davis, A., Tong, Q.C., Luong, M.H., Nguyen, C.T., Ledoux-Rak, I. and Lai, N.D., *Direct Laser Writing of Gold Nanostructures: Application to Data Storage and Color Nanoprinting.* Plasmonics, 2018: p. 1-7.
19. Gao, B., Wang, X., Li, T., Feng, Z., Wang, C. and Gu, Z., *Gecko-Inspired Paper Artificial Skin for Intimate Skin Contact and Multisensing.* Advanced Materials Technologies, 2018: p. 1800392.
20. Hu, J., Lou, Y., Wu, F. and Chen, A., *Design and fabrication of ultrathin lighting responsive security device based on moiré imaging phenomenon.* Optics Communications, 2018. **424**: p. 80-85.
21. Elsherif, M., Hassan, M.U., Yetisen, A.K. and Butt, H., *Wearable Contact Lens Biosensors for Continuous Glucose Monitoring using Smartphones.* ACS nano, 2018. *12*(6), pp.5452-5462.

22. Youn, Y., Ishitsuka, Y., Jin, C. and Selvin, P.R.,, *Thermal nanoimprint lithography for drift correction in super-resolution fluorescence microscopy.* Optics express, 2018. **26**(2): p. 1670-1680.
23. Lee, Y.-C. and S.-H. Tu, *Improving the light-emitting efficiency of GaN LEDs using nanoimprint lithography*, in *Recent Advances in Nanofabrication Techniques and Applications*. 2011, InTech.
24. Plank, H., *3D Nano-Printing via Focused Electron Beams: Principles and Applications.*
25. Pease, R., *Electron beam lithography.* Contemporary Physics, 1981. **22**(3): p. 265-290.
26. Liu, K., Avouris, P., Bucchignano, J., Martel, R., Sun, S. and Michl, J., *Simple fabrication scheme for sub-10 nm electrode gaps using electron-beam lithography.* Applied Physics Letters, 2002. **80**(5): p. 865-867.
27. Utke, I., P. Hoffmann, and J. Melngailis, *Gas-assisted focused electron beam and ion beam processing and fabrication.* Journal of Vacuum Science & Technology B: Microelectronics and Nanometer Structures Processing, Measurement, and Phenomena, 2008. **26**(4): p. 1197-1276.
28. Zgirski, M., et al., *Ion beam shaping and downsizing of nanostructures.* Nanotechnology, 2008. **19**(5): p. 055301.
29. Pimpin, A. and W.J.E.J. Srituravanich, *Review on micro-and nanolithography techniques and their applications.* 2012. **16**(1): p. 37-56.
30. Liu, G., Chen, L., Liu, J., Qiu, M., Xie, Z., Chang, J., Zhang, Y., Li, P., Lei, D.Y. and Zheng, Z., *Scanning Nanowelding Lithography for Rewritable One-Step Patterning of Sub-50 nm High-Aspect-Ratio Metal Nanostructures.* Advanced Materials, 2018: p. 1801772.
31. S Marino, S.P., M Gabás, R Romero and J R Ramos-Barrado, *Laser nano-and micro-structuring of silicon using a laser-induced plasma for beam conditioning.* Nanotechnology, 2015. **26**(5): p. 055303.
32. Yetisen, A.K., Butt, H., Volpatti, L.R., Pavlichenko, I., Humar, M., Kwok, S.J., Koo, H., Kim, K.S., Naydenova, I., Khademhosseini, A. and Hahn, S.K., *Photonic hydrogel sensors.* Biotechnology advances, 2016. **34**(3): p. 250-271.
33. Lockhart, J.N., A.B. Hmelo, and E. Harth, *Electron beam lithography of poly (glycidol) nanogels for immobilization of a three-enzyme cascade.* Polymer Chemistry, 2018.
34. Zhang, D., Zhu, Y., Liu, L., Ying, X., Hsiung, C.E., Sougrat, R., Li, K. and Han, Y., , *Atomic-resolution transmission electron microscopy of electron beam–sensitive crystalline materials.* Science, 2018: p. eaao0865.
35. Ugurlu, O., Haus, J., Gunawan, A.A., Thomas, M.G., Maheshwari, S., Tsapatsis, M. and Mkhoyan, K.A.,*Radiolysis to knock-on damage transition in zeolites under electron beam irradiation.* Physical Review B, 2011. **83**(11): p. 113408.
36. Egerton, R., *Mechanisms of radiation damage in beam-sensitive specimens, for TEM accelerating voltages between 10 and 300 kV.* Microscopy research and technique, 2012. **75**(11): p. 1550-1556.
37. Susi, T., Kotakoski, J., Arenal, R., Kurasch, S., Jiang, H., Skakalova, V., Stephan, O., Krasheninnikov, A.V., Kauppinen, E.I., Kaiser, U. and Meyer, J.C., *Atomistic description of electron beam damage in nitrogen-doped graphene and single-walled carbon nanotubes.* ACS nano, 2012. **6**(10): p. 8837-8846.
38. Fenzl, C., T. Hirsch, and O.S. Wolfbeis, *Photonic crystals for chemical sensing and biosensing.* Angewandte Chemie International Edition, 2014. **53**(13): p. 3318-3335.
39. Butt, H., Montelongo, Y., Butler, T., Rajesekharan, R., Dai, Q., Shiva-Reddy, S.G., Wilkinson, T.D. and Amaratunga, G.A., *Carbon nanotube based high resolution holograms.* Advanced Materials, 2012. **24**(44).
40. Hecht, J., *Understanding lasers: an entry-level guide*. Vol. 21. 2011: John Wiley & Sons.
41. Stuart, B.C., Feit, M.D., Rubenchik, A.M., Shore, B.W. and Perry, M.D., *Laser-induced damage in dielectrics with nanosecond to subpicosecond pulses.* Physical review letters, 1995. **74**(12): p. 2248.

42. Chichkov, B.N., Momma, C., Nolte, S., Von Alvensleben, F. and Tünnermann, A.,*Femtosecond, picosecond and nanosecond laser ablation of solids.* Applied Physics A, 1996. **63**(2): p. 109-115.
43. Elsied, A.M., Dieffenbach, P.C., Diwakar, P.K. and Hassanein, A., *Nanosecond laser-metal ablation at different ambient conditions.* Spectrochimica Acta Part B: Atomic Spectroscopy, 2018. **143**: p. 26-31.
44. Heath, D.J., Mackay, B.S., Grant-Jacob, J.A., Xie, Y., Oreffo, R.O., Eason, R.W. and Mills, B., *Closed-Loop Corrective Beam Shaping for Laser Processing of Curved Surfaces.* Journal of Micromechanics and Microengineering, 2018.
45. Alqurashi, T., Penchev, P., Yetisen, A.K., Sabouri, A., Ameen, R.M., Dimov, S. and Butt, H., , *Femtosecond laser directed fabrication of optical diffusers.* RSC Advances, 2017. **7**(29): p. 18019-18023.
46. Bieda, M., E. Beyer, and A.F. Lasagni, *Direct fabrication of hierarchical microstructures on metals by means of direct laser interference patterning.* Journal of Engineering Materials and Technology, 2010. **132**(3): p. 031015.
47. Metev, S.M. and V.P. Veiko, *Laser-assisted microtechnology*. Vol. 19. 2013: Springer Science & Business Media.
48. Zhao, Q., Yetisen, A.K., Anthony, C.J., Fowler, W.R., Yun, S.H. and Butt, H.,*Printable ink holograms.* Applied Physics Letters, 2015. **107**(4): p. 041115.
49. Zhao, Q., Yetisen, A.K., Sabouri, A., Yun, S.H. and Butt, H., *Printable nanophotonic devices via holographic laser ablation.* ACS nano, 2015. **9**(9): p. 9062-9069.
50. Ahmed, R., Yetisen, A.K., El Khoury, A. and Butt, H., *Printable ink lenses, diffusers, and 2D gratings.* Nanoscale, 2017. **9**(1): p. 266-276.
51. AlQattan, B., Butt, H., Sabouri, A., Yetisen, A.K., Ahmed, R. and Mahmoodi, N.,*Holographic direct pulsed laser writing of two-dimensional nanostructures.* Rsc Advances, 2016. **6**(112): p. 111269.
52. AlQattan, B., A.K. Yetisen, and H. Butt, *Direct Laser Writing of Nanophotonic Structures on Contact Lenses.* ACS nano, 2018. 12(6), pp.5130-5140.
53. Menon, R., et al., *Maskless lithography.* 2005. **8**(2): p. 26-33.
54. Pease, R.F. and S.Y.J.P.o.t.I. Chou, *Lithography and other patterning techniques for future electronics.* 2008. **96**(2): p. 248-270.
55. Gates, B.D., Xu, Q., Stewart, M., Ryan, D., Willson, C.G. and Whitesides, G.M., *New approaches to nanofabrication: molding, printing, and other techniques.* 2005. **105**(4): p. 1171-1196.
56. Madou, M.J., *Fundamentals of microfabrication: the science of miniaturization*. 2002: CRC press.
57. Altissimo, M.J.B., *E-beam lithography for micro-/nanofabrication.* 2010. **4**(2): p. 026503.
58. Zhang, Y., C. Liu, and D. Whalley. *Direct-write techniques for maskless production of microelectronics: A review of current state-of-the-art technologies*. in *2009 International Conference on Electronic Packaging Technology & High Density Packaging*. 2009. IEEE.
59. Elsied, A.M., Dieffenbach, P.C., Diwakar, P.K. and Hassanein, A., *Nanosecond laser-metal ablation at different ambient conditions.* 2018. **143**: p. 26-31.
60. Petrov, T., Pecheva, E., Walmsley, A.D. and Dimov, S., *Femtosecond laser ablation of dentin and enamel for fast and more precise dental cavity preparation.* 2018. **90**: p. 433-438.
61. AlQattan, B., Benton, D., Yetisen, A.K. and Butt, H., *Laser Nanopatterning of Colored Ink Thin Films for Photonic Devices.* ACS Applied Materials & Interfaces, 2017. *9*(45), pp.39641-39649.
62. Hecht, E., *Optics Third Edition||*. Addison-Wesley, 1998.
63. Hecht, E. and A. Zajac, *Optics. Addison-Wellesley.* Reading, MA, 1974.
64. Born, M. and E. Wolf, *Principles of optics: electromagnetic theory of propagation, interference and diffraction of light*. 2013: Elsevier.
65. Ignatov, A. and A. Merzlikin, *Excitation of plasmonic waves in metal–dielectric structures by a laser beam using holography principles.* Optics Communications, 2018. **410**: p. 83-87.

66. Moghaddam, G.K., Margerison, H., Suzuki, J., Blyth, J. and Lowe, C.R., 2018. *A transparent glucose-sensitive double polymerised holographic sensor.* Sensors and Actuators B: Chemical, 2018. **267**: p. 1-4.
67. Bonod, N. and J. Neauport, *Diffraction gratings: from principles to applications in high-intensity lasers.* Advances in Optics and Photonics, 2016. **8**(1): p. 156-199.
68. Chen, Q. and D.R. Cumming, *High transmission and low color cross-talk plasmonic color filters using triangular-lattice hole arrays in aluminum films.* Optics express, 2010. **18**(13): p. 14056-14062.
69. Vukusic, P. and J.R. Sambles, *Photonic structures in biology.* Nature, 2003. **424**(6950): p. 852-855.
70. Gao, Y., Huang, C., Hao, C., Sun, S., Zhang, L., Zhang, C., Duan, Z., Wang, K., Jin, Z., Zhang, N. and Kildishev, A.V., *Lead Halide Perovskite Nanostructures for Dynamic Color Display.* ACS nano, 2018. **12**(9): p. 8847-8854.
71. Barrows, F.P. and M.H. Bartl, *Photonic structures in biology: A possible blueprint for nanotechnology.* Nanomaterials and Nanotechnology, 2014. **4**(Godište 2014): p. 4-1.
72. Butt, H., Yetisen, A.K., Mistry, D., Khan, S.A., Hassan, M.U. and Yun, S.H., *Morpho Butterfly-Inspired Nanostructures.* Advanced Optical Materials, 2016.
73. Born, M. and E. Wolf, *Principles of optics: electromagnetic theory of propagation, interference and diffraction of light*. 2000: CUP Archive.
74. Yu, N., Genevet, P., Kats, M.A., Aieta, F., Tetienne, J.P., Capasso, F. and Gaburro, Z., *Light propagation with phase discontinuities: generalized laws of reflection and refraction.* science, 2011: p. 1210713.
75. Zhang, L., Mei, S., Huang, K. and Qiu, C.W.,*Advances in full control of electromagnetic waves with metasurfaces.* Advanced Optical Materials, 2016. **4**(6): p. 818-833.
76. Zhang, L., Wu, R.Y., Bai, G.D., Wu, H.T., Ma, Q., Chen, X.Q. and Cui, T.J., *Multifunctional Metasurfaces: Transmission-Reflection-Integrated Multifunctional Coding Metasurface for Full-Space Controls of Electromagnetic Waves (Adv. Funct. Mater. 33/2018).* Advanced Functional Materials, 2018. **28**(33): p. 1870232.
77. Huang, Y., Li, W., Qin, M., Zhou, H., Zhang, X., Li, F. and Song, Y., *Printable functional chips based on nanoparticle assembly.* Small, 2017. **13**(4): p. 1503339.
78. Ahn, T., Oh, S., Hu, X., Lee, J.W., Park, C.W., Yang, H.M., Kim, C. and Kim, J.D., *Controlled Self-Assembly for High-Resolution Magnetic Printing.* Small, 2014. **10**(6): p. 1081-1085.
79. Nie, Z. and E. Kumacheva, *Patterning surfaces with functional polymers.* Nature materials, 2008. **7**(4): p. 277.
80. Zope, K.R., D. Cormier, and S.A. Williams, *Reactive Silver Oxalate Ink Composition with Enhanced Curing Conditions for Flexible Substrates.* ACS applied materials & interfaces, 2018. **10**(4): p. 3830-3837.
81. Liu, H.Y., Wang, C.T., Hsu, C.Y. and Lin, T.H., , *Pinning effect on the photonic bandgaps of blue-phase liquid crystal.* Applied optics, 2011. **50**(11): p. 1606-1609.
82. Zheng, Z.G., Yuan, C.L., Hu, W., Bisoyi, H.K., Tang, M.J., Liu, Z., Sun, P.Z., Yang, W.Q., Wang, X.Q., Shen, D. and Li, Y., *Light-patterned crystallographic direction of a self-organized 3d soft photonic crystal.* Advanced Materials, 2017. **29**(42): p. 1703165.
83. De Sio, L., Lloyd, P.F., Tabiryan, N.V. and Bunning, T.J., *Hidden Gratings in Holographic Liquid Crystal Polymer-Dispersed Liquid Crystal Films.* ACS applied materials & interfaces, 2018. **10**(15): p. 13107-13112.
84. Højlund-Nielsen, E., Clausen, J., Mäkela, T., Thamdrup, L.H., Zalkovskij, M., Nielsen, T., Li Pira, N., Ahopelto, J., Mortensen, N.A. and Kristensen, A., *Plasmonic colors: toward mass production of metasurfaces.* Advanced Materials Technologies, 2016. **1**(7): p. 1600054.
85. Shaltout, A.M., Kim, J., Boltasseva, A., Shalaev, V.M. and Kildishev, A.V., *Ultrathin and multicolour optical cavities with embedded metasurfaces.* Nature communications, 2018. **9**(1): p. 2673.

86. West, P., *Principles of Holography.* Optica Acta: International Journal of Optics, 1970. **17**(2): p. 154-155.
87. Magnusson, R. and T. Gaylord, *Diffraction efficiencies of thin phase gratings with arbitrary grating shape.* JOSA, 1978. **68**(6): p. 806-809.
88. Meerholz, K., Volodin, B.L., Kippelen, B. and Peyghambarian, N., *A photorefractive polymer with high optical gain and diffraction efficiency near 100%.* Nature, 1994. **371**(6497): p. 497.
89. Lu, W.G., Xiao, R., Liu, J., Wang, L., Zhong, H. and Wang, Y., *Large-area rainbow holographic diffraction gratings on a curved surface using transferred photopolymer films.* Optics letters, 2018. **43**(4): p. 675-678.
90. Montemezzani, G. and M. Zgonik, *Light diffraction at mixed phase and absorption gratings in anisotropic media for arbitrary geometries.* Physical Review E, 1997. **55**(1): p. 1035.
91. Bao, F., Geraghty, B., Wang, Q. and Elsheikh, A., *Consideration of corneal biomechanics in the diagnosis and management of keratoconus: is it important?* 2016. **3**(1): p. 18.
92. Tomić, M., Vrabec, R., Poljičanin, T., Ljubić, S. and Duvnjak, L., *Diabetic macular edema: Traditional and novel treatment.* 2017. **56**(1.): p. 124-131.
93. Azzam, S.H., Kang, S., Salvi, M. and Ezra, D.G.,*Tocilizumab for thyroid eye disease.* 2018(3).
94. Micheal, S., et al., *Variants in the PRPF8 Gene are Associated with Glaucoma.* 2018. **55**(5): p. 4504-4510.
95. Solomon, C.G.J.N.E.J.M., *Primary Sjögren's Syndrome.* 2018. **378**: p. 931-9.
96. Zaidi, H.J.M., *Using Nanoparticle Drug Delivery Mechanisms to Improve Eye Moisture Over Extended Periods of Contact Lens Wear.* 2018. **1**(1).
97. Blum, R.D. and W. Kokonaski, *Stabilized electro-active contact lens*. 2006, Google Patents.
98. Yao, H., Marcheselli, C., Afanasiev, A., Lähdesmäki, I. and Parviz, B.A., *A soft hydrogel contact lens with an encapsulated sensor for tear glucose monitoring*. in *Micro Electro Mechanical Systems (MEMS), 2012 IEEE 25th International Conference on*. 2012. IEEE.
99. Brygoła, R., Sęk, S., Sokołowski, M., Kowalczyk-Hernández, M. and Pniewski, J., *Limits in measurements of contact lens surface profile using atomic force microscopy.* Colloids and Surfaces B: Biointerfaces, 2018. **165**: p. 229-234.
100. Guryča, V., Hobzová, R., Přádný, M., Širc, J. and Michálek, J., *Surface morphology of contact lenses probed with microscopy techniques.* Contact Lens and Anterior Eye, 2007. **30**(4): p. 215-222.
101. Efron, N., *Contact Lens Practice E-Book*. 2016: Elsevier Health Sciences.
102. Drelich, J., Chibowski, E., Meng, D.D. and Terpilowski, K., *Hydrophilic and superhydrophilic surfaces and materials.* Soft Matter, 2011. **7**(21): p. 9804-9828.
103. Campbell, D., S.M. Carnell, and R.J. Eden, *Applicability of contact angle techniques used in the analysis of contact lenses, part 1: comparative methodologies.* Eye & contact lens, 2013. **39**(3): p. 254-262.
104. Torfs, T., Sterken, T., Brebels, S., Santana, J., van den Hoven, R., Spiering, V., Bertsch, N., Trapani, D. and Zonta, D., *Low power wireless sensor network for building monitoring.* IEEE Sensors Journal, 2013. **13**(3): p. 909-915.
105. Nordblom, T. and J. Galbreath, *Wireless Sensor Networks for Improved Long-Term Bridge Performance.* Microstrain white paper, 2012.
106. Yun, H.B., Kim, S.H., Wu, L. and Lee, J.J., *Development of inspection robots for bridge cables.* The Scientific World Journal, 2013(967508): p. 17.
107. Mihailov, S.J., *Fiber Bragg grating sensors for harsh environments.* Sensors, 2012. **12**(2): p. 1898-1918.
108. Trilaksono, A., Watanabe, N., Hoshi, H., Kondo, A., Iwahori, Y. and Takeda, S., *Damage monitoring in composite stiffened skin using fiber Bragg grating under tensile and three-point loading.* J Mech Eng Autom, 2013. **3**: p. 227-237.

109. Huang, Y., Ding, Y., Bian, J., Su, Y., Zhou, J., Duan, Y. and Yin, Z., *Hyper-stretchable self-powered sensors based on electrohydrodynamically printed, self-similar piezoelectric nano/microfibers.* Nano Energy, 2017. **40**: p. 432-439.
110. Xu, L., Rahmani, M., Kamali, K.Z., Lamprianidis, A., Ghirardini, L., Sautter, J., Camacho-Morales, R., Chen, H., Parry, M., Staude, I. and Zhang, G., *Boosting third-harmonic generation by a mirror-enhanced anapole resonator.* Light: Science and Applications, 2018. **7**: p. 1-8.
111. Sati, P., A. Sharma, and V. Tripathi, *Self focusing of a quadruple Gaussian laser beam in a plasma.* Physics of Plasmas, 2012. **19**(9): p. 092117.
112. Blanchard, P.M. and A.H. Greenaway, *Simultaneous multiplane imaging with a distorted diffraction grating.* Applied optics, 1999. **38**(32): p. 6692-6699.
113. Zhang, F., Zhang, D., Xiong, J., Wang, H., Niu, K., Jin, B. and Wang, Y., *From Fresnel Diffraction Model to Fine-grained Human Respiration Sensing with Commodity Wi-Fi Devices.* Proceedings of the ACM on Interactive, Mobile, Wearable and Ubiquitous Technologies, 2018. **2**(1): p. 53.
114. Furlan, W.D., G. Saavedra, and J.A. Monsoriu, *White-light imaging with fractal zone plates.* Optics Letters, 2007. **32**(15): p. 2109-2111.
115. Keskinbora, K., Sanli, U.T., Baluktsian, M., Grévent, C., Weigand, M. and Schütz, G., *High-throughput synthesis of modified Fresnel zone plate arrays via ion beam lithography.* Beilstein journal of nanotechnology, 2018. **9**(1): p. 2049-2056.
116. Alqurashi, T., Montelongo, Y., Penchev, P., Yetisen, A.K., Dimov, S. and Butt, H., *Correction: Femtosecond laser ablation of transparent microphotonic devices and computer-generated holograms.* Nanoscale, 2017. **9**(39): p. 15159-15159.
117. Ren, H., Y.-H. Fan, and S.-T. Wu, *Tunable Fresnel lens using nanoscale polymer-dispersed liquid crystals.* Applied Physics Letters, 2003. **83**(8): p. 1515-1517.
118. Blanchard, P. and A. Greenaway, *Broadband simultaneous multiplane imaging.* Optics communications, 2000. **183**(1-4): p. 29-36.
119. Gupta, N., *Self-action effects of quadruple-Gaussian laser beam in media possessing cubic–quintic nonlinearity.* Journal of Electromagnetic Waves and Applications, 2018. **32**(18): p. 2350-2366.
120. Aydin Sabouri, C.J.A., Philip D Prewett, James Bowen and Haider Butt, *Effects of current on early stages of focused ion beam nano-machining.* Materials Research Express, 2015. **2**(5): p. 055005.
121. Lasagni, A.F., Acevedo, D.F., Barbero, C.A. and Mücklich, F., *One-Step Production of Organized Surface Architectures on Polymeric Materials by Direct Laser Interference Patterning.* Advanced Engineering Materials, 2007. **9**(1-2): p. 99-103.
122. Xia, D., Ku, Z., Lee, S.C. and Brueck, S.R.J., *Nanostructures and functional materials fabricated by interferometric lithography.* Advanced materials, 2011. **23**(2): p. 147-179.
123. Karnakis, D.M., *High power single-shot laser ablation of silicon with nanosecond 355nm.* Applied Surface Science, 2006. **252**(22): p. 7823-7825.
124. Fernando da Cruz Vasconcellos, et al., *Printable surface holograms via laser ablation.* ACS Photonics, 2014. **1**(6): p. 489-495.
125. Müller-Meskamp, L., Schubert, S., Roch, T., Eckhardt, S., Lasagni, A.F. and Leo, K.,*Transparent Conductive Metal Thin-Film Electrodes Structured by Direct Laser Interference Patterning.* Advanced Engineering Materials, 2015. **17**(8): p. 1215-1219.
126. Butt, H., Dai, Q., Rajasekharan, R., Wilkinson, T.D. and Amaratunga, G.A.,*Enhanced reflection from arrays of silicon based inverted nanocones.* Applied Physics Letters, 2011. **99**(13): p. 133105.
127. Ahmed, R., Rifat, A.A., Yetisen, A.K., Dai, Q., Yun, S.H. and Butt, H., *Multiwall carbon nanotube microcavity arrays.* Journal of Applied Physics, 2016. **119**(11): p. 113105.
128. Butt, H., Yetisen, A.K., Ahmed, R., Yun, S.H. and Dai, Q., *Carbon nanotube biconvex microcavities.* Applied Physics Letters, 2015. **106**(12): p. 121108.

129. Ahmed, R., Rifat, A.A., Yetisen, A.K., Salem, M.S., Yun, S.H. and Butt, H., *Optical microring resonator based corrosion sensing.* Rsc Advances, 2016. **6**(61): p. 56127-56133.
130. Palmer, C.A., E.G. Loewen, and R. Thermo, *Diffraction grating handbook*. 2005: Newport Corporation Springfield, Ohio, USA.
131. Sabouri, A., et al., *Ahmed, R., Rifat, A.A., Yetisen, A.K., Salem, M.S., Yun, S.H. and Butt, H.,* Materials Research Express, 2015. **2**(5): p. 055005.
132. Kong, X.T., Khan, A.A., Kidambi, P.R., Deng, S., Yetisen, A.K., Dlubak, B., Hiralal, P., Montelongo, Y., Bowen, J., Xavier, S. and Jiang, K., *Graphene-based ultrathin flat lenses.* ACS Photonics, 2015. **2**(2): p. 200-207.
133. Alqurashi, T., Penchev, P., Yetisen, A.K., Sabouri, A., Ameen, R.M., Dimov, S. and Butt, H.,*Femtosecond laser directed fabrication of optical diffusers.* RSC Advances, 2017. **7**(29): p. 18019-18023.
134. Alqurashi, T., Sabouri, A., Yetisen, A.K. and Butt, H.,*Nanosecond pulsed laser texturing of optical diffusers.* AIP Advances, 2017. **7**(2): p. 025313.
135. Zhu, X., Yan, W., Levy, U., Mortensen, N.A. and Kristensen, A., *Resonant laser printing of structural colors on high-index dielectric metasurfaces.* Science Advances, 2017. **3**(5): p. e1602487.
136. Xiong, K., Emilsson, G., Maziz, A., Yang, X., Shao, L., Jager, E.W. and Dahlin, A.B., *Plasmonic metasurfaces with conjugated polymers for flexible electronic paper in color.* 2016. **28**(45): p. 9956-9960.
137. Medintz, I.L., Uyeda, H.T., Goldman, E.R. and Mattoussi, H., *Quantum dot bioconjugates for imaging, labelling and sensing.* Nature materials, 2005. **4**(6): p. 435.
138. Zhang, X.Y., Hu, A., Zhang, T., Lei, W., Xue, X.J., Zhou, Y. and Duley, W.W.,*Self-assembly of large-scale and ultrathin silver nanoplate films with tunable plasmon resonance properties.* ACS nano, 2011. **5**(11): p. 9082-9092.
139. Zheng, Z.G., Yuan, C.L., Hu, W., Bisoyi, H.K., Tang, M.J., Liu, Z., Sun, P.Z., Yang, W.Q., Wang, X.Q., Shen, D. and Li, Y., *Light-Patterned Crystallographic Direction of a Self-Organized 3D Soft Photonic Crystal.* Advanced Materials, 2017.
140. Sun, P.Z., Liu, Z., Wang, W., Ma, L.L., Shen, D., Hu, W., Lu, Y., Chen, L. and Zheng, Z.G.,*Light-reconfigured waveband-selective diffraction device enabled by micro-patterning of a photoresponsive self-organized helical superstructure.* Journal of Materials Chemistry C, 2016. **4**(39): p. 9325-9330.
141. Zhu, X., Vannahme, C., Højlund-Nielsen, E., Mortensen, N.A. and Kristensen, A., *Plasmonic colour laser printing.* Nature nanotechnology, 2016. **11**(4): p. 325-329.
142. Carstensen, M.S., Zhu, X., Iyore, O.E., Mortensen, N.A., Levy, U. and Kristensen, A., *Holographic Resonant Laser Printing of flat optics using template plasmonic metasurfaces.* arXiv preprint arXiv:1708.05571, 2017.
143. Xia, D., Ku, Z., Lee, S.C. and Brueck, S.R.J., *Nanostructures and functional materials fabricated by interferometric lithography.* Advanced materials, 2011. **23**(2): p. 147-179.
144. Karnakis, D., *High power single-shot laser ablation of silicon with nanosecond 355 nm.* Applied Surface Science, 2006. **252**(22): p. 7823-7825.
145. Vasconcellos, F.D.C., Yetisen, A.K., Montelongo, Y., Butt, H., Grigore, A., Davidson, C.A., Blyth, J., Monteiro, M.J., Wilkinson, T.D. and Lowe, C.R.,*Printable surface holograms via laser ablation.* ACS Photonics, 2014. **1**(6): p. 489-495.
146. Magnusson, R. and T. Gaylord, *Diffraction efficiencies of thin absorption and transmittance gratings.* Optics Communications, 1979. **28**(1): p. 1-3.
147. Magnusson, R. and T. Gaylord, *Analysis of multiwave diffraction of thick gratings.* JOSA, 1977. **67**(9): p. 1165-1170.
148. Hecht, E. and A. Zajac, *Optics Addison-Wesley.* Reading, Mass, 1974. **19872**: p. 350-351.

149. Naseri, T. and R. Sadighi-Bonabi, *Efficient electromagnetically induced phase grating via quantum interference in a four-level N-type atomic system.* JOSA B, 2014. **31**(10): p. 2430-2437.
150. Gao, H., Ouyang, M., Wang, Y., Shen, Y., Zhou, J. and Liu, D., *Analysis on diffraction properties of the transmission phase grating.* Optik-International Journal for Light and Electron Optics, 2007. **118**(9): p. 452-456.
151. Magnusson, R. and T. Gaylord, *Diffraction regimes of transmission gratings.* JOSA, 1978. **68**(6): p. 809-814.
152. Blanche, P.A., Bablumian, A., Voorakaranam, R., Christenson, C., Lin, W., Gu, T., Flores, D., Wang, P., Hsieh, W.Y., Kathaperumal, M. and Rachwal, B., *Holographic three-dimensional telepresence using large-area photorefractive polymer.* Nature, 2010. **468**(7320): p. 80.
153. Do, D.V., Nguyen, Q.D., Boyer, D., Schmidt-Erfurth, U., Brown, D.M., Vitti, R., Berliner, A.J., Gao, B., Zeitz, O., Ruckert, R. and Schmelter, T., *One-year outcomes of the da Vinci Study of VEGF Trap-Eye in eyes with diabetic macular edema.* Ophthalmology, 2012. **119**(8): p. 1658-1665.
154. Weetman, A.P., *Graves' disease.* New England Journal of Medicine, 2000. **343**(17): p. 1236-1248.
155. Boelaert, K., Torlinska, B., Holder, R.L. and Franklyn, J.A., *Older subjects with hyperthyroidism present with a paucity of symptoms and signs: a large cross-sectional study.* The Journal of Clinical Endocrinology & Metabolism, 2010. **95**(6): p. 2715-2726.
156. Quigley, H.A. and A.T. Broman, *The number of people with glaucoma worldwide in 2010 and 2020.* British journal of ophthalmology, 2006. **90**(3): p. 262-267.
157. Lee, S.J., C.K. Lee, and W.-S. Kim, *Long-term therapeutic efficacy of phacoemulsification with intraocular lens implantation in patients with phacomorphic glaucoma.* Journal of Cataract & Refractive Surgery, 2010. **36**(5): p. 783-789.
158. Yetisen, A.K., Jiang, N., Tamayol, A., Ruiz-Esparza, G.U., Zhang, Y.S., *based microfluidic system for tear electrolyte analysis.* Lab on a Chip, 2017. **17**(6): p. 1137-1148.
159. Ouellette, A.L., Li, J.J., Cooper, D.E., Ricco, A.J. and Kovacs, G.T., *Evolving point-of-care diagnostics using up-converting phosphor bioanalytical systems*. 2009, ACS Publications.
160. Khuri, R.N., *Device for determination of tear constituents*. 1994, Google Patents.
161. Harvey, D., N.W. Hayes, and B. Tighe, *Fibre optics sensors in tear electrolyte analysis: Towards a novel point of care potassium sensor.* Contact Lens and Anterior Eye, 2012. **35**(3): p. 137-144.
162. Jiao, L., Fan, B., Xian, X., Wu, Z., Zhang, J. and Liu, Z., *Creation of nanostructures with poly (methyl methacrylate)-mediated nanotransfer printing.* Journal of the American Chemical Society, 2008. **130**(38): p. 12612-12613.
163. Kumar, A. and G.M. Whitesides, *Features of gold having micrometer to centimeter dimensions can be formed through a combination of stamping with an elastomeric stamp and an alkanethiol ''ink''followed by chemical etching.* Applied Physics Letters, 1993. **63**(14): p. 2002-2004.
164. Cavallini, M., M. Murgia, and F. Biscarini, *Patterning a conjugated molecular thin film at submicron scale by modified microtransfer molding.* Nano Letters, 2001. **1**(4): p. 193-195.
165. Khalid, M.W., Ahmed, R., Yetisen, A.K., AlQattan, B. and Butt, H., *Holographic Writing of Ink-Based Phase Conjugate Nanostructures via Laser Ablation.* Scientific Reports, 2017. **7**(1): p. 10603.
166. Lin, M.C. and T.F. Svitova, *Contact lenses wettability in vitro: effect of surface-active ingredients.* Optometry and vision science: official publication of the American Academy of Optometry, 2010. **87**(6): p. 440.
167. Uyama, Y., Inoue, H., Ito, K., Kishida, A. and Ikada, Y., *Comparison of different methods for contact angle measurement.* Journal of colloid and interface science, 1991. **141**(1): p. 275-279.

168. Morgan, P.B., Chamberlain, P., Moody, K. and Maldonado-Codina, C., *Ocular physiology and comfort in neophyte subjects fitted with daily disposable silicone hydrogel contact lenses.* Contact Lens and Anterior Eye, 2013. **36**(3): p. 118-125.
169. González-Méijome, J.M., et al., *Refractive index and equilibrium water content of conventional and silicone hydrogel contact lenses.* Ophthalmic and Physiological Optics, 2006. **26**(1): p. 57-64.
170. Varikooty, J., Keir, N., Richter, D., Jones, L.W., Woods, C. and Fonn, D.,*Comfort response of three silicone hydrogel daily disposable contact lenses.* Optometry & Vision Science, 2013. **90**(9): p. 945-953.
171. Cerdeira, A.M., M. Mazzotti, and B. Gander, *Miconazole nanosuspensions: influence of formulation variables on particle size reduction and physical stability.* International journal of pharmaceutics, 2010. **396**(1): p. 210-218.
172. Rahman, M.Q., Chuah, K.S., Macdonald, E.C.A., Trusler, J.P.M. and Ramaesh, K.,*The effect of pH, dilution, and temperature on the viscosity of ocular lubricants—shift in rheological parameters and potential clinical significance.* Eye, 2012. **26**(12): p. 1579.
173. Bilalov, E. and A. Avanesova, *Evaluation of prophylaxis of dry eye syndrome associated with soft contact lenses.* Medical and Health Science Journal, 2013. **14**(4): p. 186-190.
174. Craig, J.P., Simmons, P.A., Patel, S. and Tomlinson, A.,*Refractive index and osmolality of human tears.* Optometry & Vision Science, 1995. **72**(10): p. 718-724.
175. Campbell D, C.S., Eden RJ. , *Applicability of contact Angle techniques used in the analysis of contact lenses, Part I: .* Eye & Cont Lens, 2013. **39**(3): p. 254-262.
176. Read, M.L., Morgan, P.B., Kelly, J.M. and Maldonado-Codina, C., *Dynamic contact angle analysis of silicone hydrogel contact lenses.* Journal of biomaterials applications, 2011. **26**(1): p. 85-99.
177. Bright, A.M. and B.J. Tighe, *The composition and interfacial properties of tears, tear substitutes and tear models.* Journal of The British Contact Lens Association, 1993. **16**(2): p. 57-66.
178. Yin, F., Ye, D., Zhu, C., Qiu, L. and Huang, Y., *Stretchable, highly durable ternary nanocomposite strain sensor for structural health monitoring of flexible aircraft.* Sensors, 2017. **17**(11): p. 2677.
179. Smith, G.K., *Calcite straw stalactites growing from concrete structures.* Cave and Karst Science, 2016. **43**(1): p. 4-10.
180. Arms, S.W., Townsend, C.P., Galbreath, J.H., DiStasi, S.J., Liebschutz, D. and Phan, N., *Flight testing of wireless sensing networks for rotorcraft structural health and usage management systems*. in *Proceedings of 14th Australian International Aerospace Congress Google Scholar*. 2011.
181. Campbell, R.A., Pickett, B.M., Saponara, V.L. and Dierdorf, D., *Thermal characterization and flammability of structural epoxy adhesive and carbon/epoxy composite with environmental and chemical degradation.* Journal of Adhesion Science and Technology, 2012. **26**(7): p. 889-910.
182. Kaw, A.K., *Mechanics of composite materials*. 2005: CRC press.
183. Trilaksono, A., Watanabe, N., Hoshi, H., Takeda, S.I. and Iwahori, Y.,*MONITORING SECONDARY BENDING FAILURE UNDER TENSION LOAD USING FIBER BRAGG GRATING,*2012
184. Bocciolone, M., et al., *Design and testing of fibre Bragg grating force transducers for the measurement of pantograph–catenary contact force.* Proceedings of the Institution of Mechanical Engineers, Part F: Journal of Rail and Rapid Transit, 2018: p. 0954409718795762.
185. Amjadi, M., Pichitpajongkit, A., Lee, S., Ryu, S. and Park, I., *Highly stretchable and sensitive strain sensor based on silver nanowire–elastomer nanocomposite.* 2014. **8**(5): p. 5154-5163.
186. Amjadi, M., Kyung, K.U., Park, I. and Sitti, M., *Stretchable, skin-mountable, and wearable strain sensors and their potential applications: a review.* 2016. **26**(11): p. 1678-1698.

187. Rashid, I., Butt, H., Yetisen, A.K., Dlubak, B., Davies, J.E., Seneor, P., Vechhiola, A., Bouamrane, F. and Xavier, S., *Wavelength-Selective Diffraction from Silica Thin-Film Gratings.* ACS Photonics, 2017. **4**(10): p. 2402-2409.
188. Trilaksono, A., Watanabe, N., Hoshi, H., Kondo, A., Iwahori, Y. and Takeda, S.I., *Continuous Damage Monitoring of a Thin Composite Structural with Mismatched Stiffener in a Combined Joint Using Fiber Bragg Grating under Tension and Three-Point Loading.* Open Journal of Composite Materials, 2013. **3**(03): p. 63.
189. Yu, J., Zhou, C., Jia, W., Ma, J., Hu, A., Wu, J. and Wang, S., *Distorted Dammann grating.* Optics letters, 2013. **38**(4): p. 474-476.
190. Alqurashi, T., et al., *Laser inscription of pseudorandom structures for microphotonic diffuser applications.* Nanoscale, 2018. **10**(15): p. 7095-7107.
191. Müller-Meskamp, L., Schubert, S., Roch, T., Eckhardt, S., Lasagni, A.F. and Leo, K., *Transparent Conductive Metal Thin-Film Electrodes Structured by Direct Laser Interference Patterning.* Advanced Engineering Materials, 2015. **17**(8): p. 1215-1219.
192. Aggarwal, M., S. Vij, and N. Kant, *Propagation of circularly polarized quadruple Gaussian laser beam in magnetoplasma.* Optik-International Journal for Light and Electron Optics, 2015. **126**(24): p. 5710-5714.
193. Yang, Z. and Q. Zhan, *Single-Shot Smartphone-Based Quantitative Phase Imaging Using a Distorted Grating.* PloS one, 2016. **11**(7): p. e0159596.
194. , Blanchard, P.M., Fisher, D.J., Woods, S.C. and Greenaway, A.H., *Phase-diversity wave-front sensing with a distorted diffraction grating.* Applied optics, 2000. **39**(35): p. 6649-6655.
195. Deng, S., Yetisen, A.K., Jiang, K. and Butt, H., *Computational modelling of a graphene Fresnel lens on different substrates.* RSC Advances, 2014. **4**(57): p. 30050-30058.
196. Deng, S., Penchev, P., Liu, J., Wang, Y., Jiang, K., Dimov, S., Zhang, Z., Liu, Y., Leng, J. and Butt, H., *Laser directed writing of flat lenses on buckypaper.* Nanoscale, 2015. **7**(29): p. 12405-12410.

Appendix

2S- Literature review

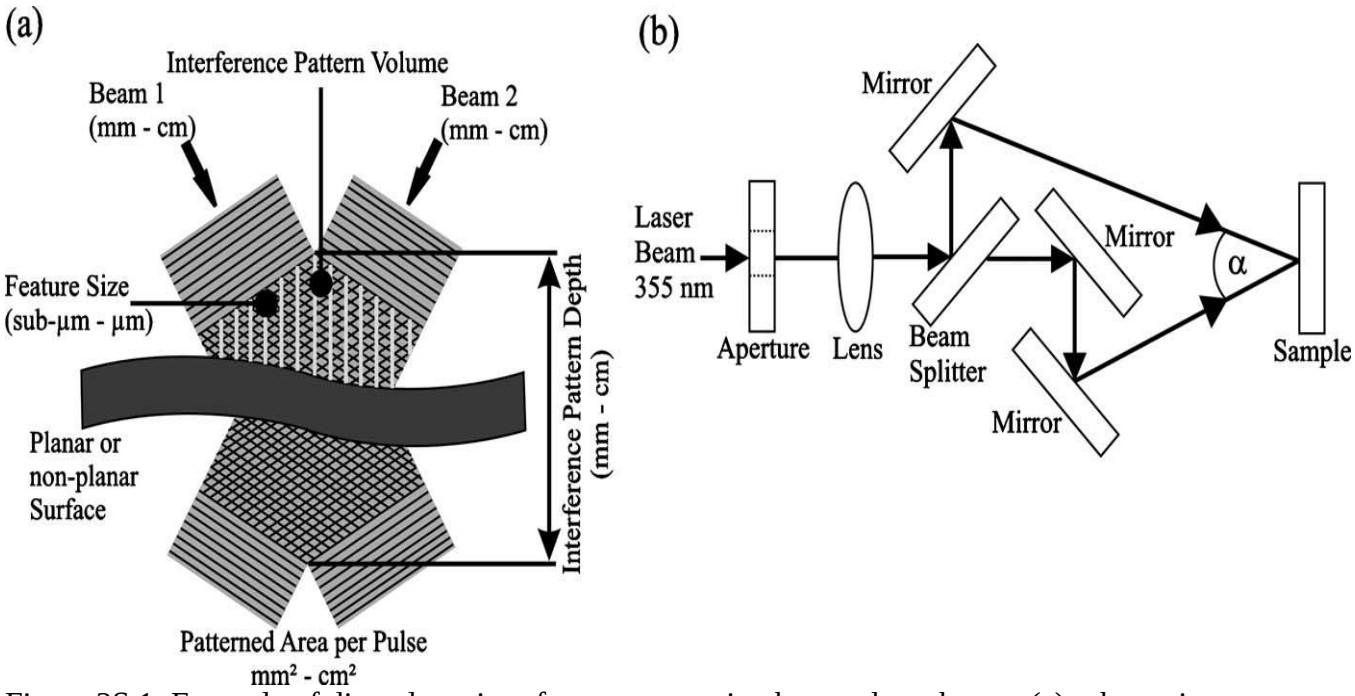

Figure 2S.1: Example of direct laser interference patterning by two laser beams (a) schematic diagram of interference principle, (b) experimental set up.

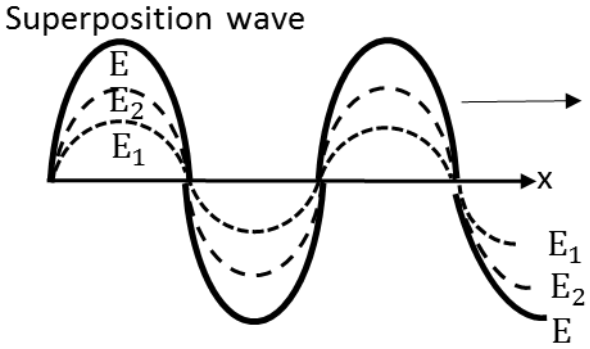

Figure 2S.2: Two harmonic Electric waves move in parallel to form superposition waves.

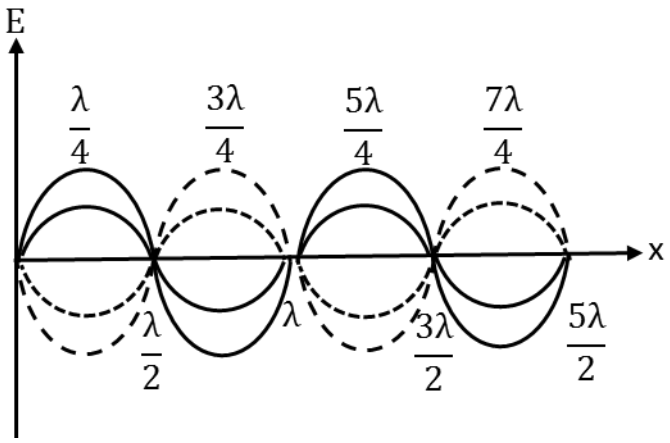

Figure 2S.3:Two harmonic Electric waves move in opposite each other to form superposition waves.

3S-HOLOGRAPHIC DIRECT PULSED LASER WRITING OF TWO DIMENSIONAL NANOSTRUCTURES

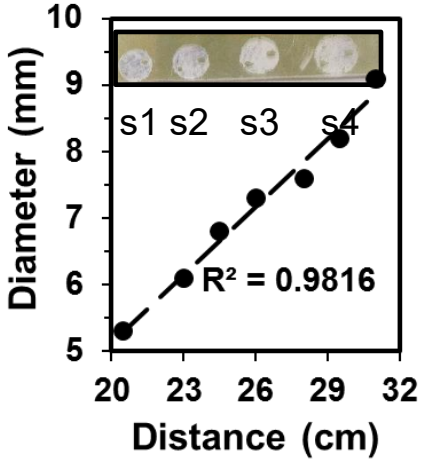

Figure 3S.4: Laser spot size as a function of (h) distance variations. Inset size (diameters): s1 = 7.3 mm, s2 = 7.6 mm, s3 = 8.2 mm, and s4 = 9.1 mm.

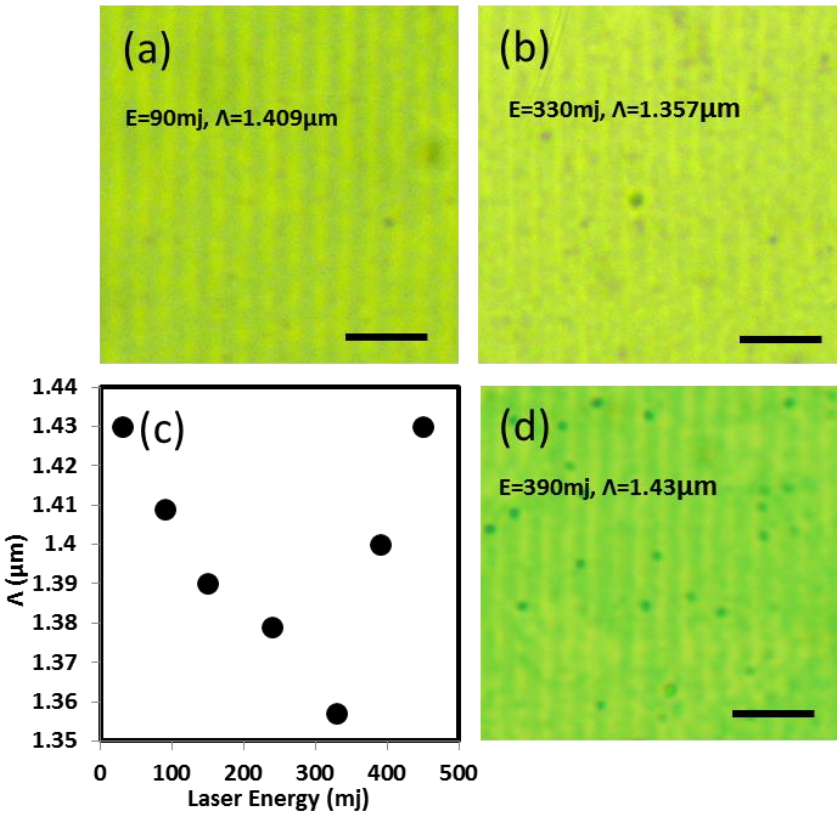

Figure 3S.5: Microscopy images of the Au 25nm thickness surface gratings fabricated by holographic DLIP. (a, b, d) Examples of changing the laser energy on the Au film. (c) The plot for the change of energy effect in the Au film. The graph shows that the effect of laser energy after 330mJ on Au film which increase the removal rate and affect the material quality.(scale bar =5 µm)

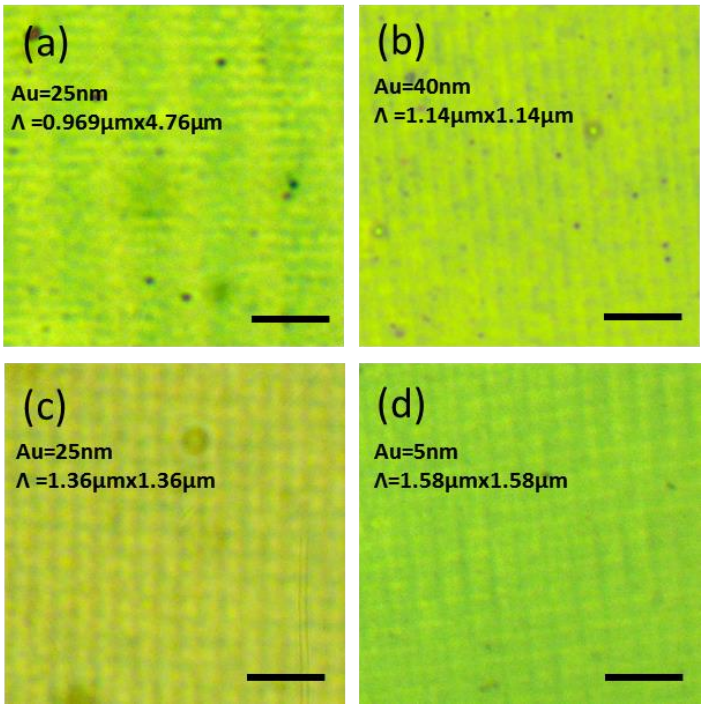

Figure 3S.6:Microscopy images of 2D arrays with different thicknesses fabricated by holographic DLIP. (a) Arrays of 25 nm thick rectangle (0.969 µm ×4.76 µm) and (b) Arrays of 40 nm thick square (1.14µm × 1.14 µm), (c) Arrays of Au 25 nm thick squares (1.36 µm × 1.36µm) and (d) Arrays of 5 nm thick square (1.58 µm × 1.528 nm). (scale bar = 10 µm).

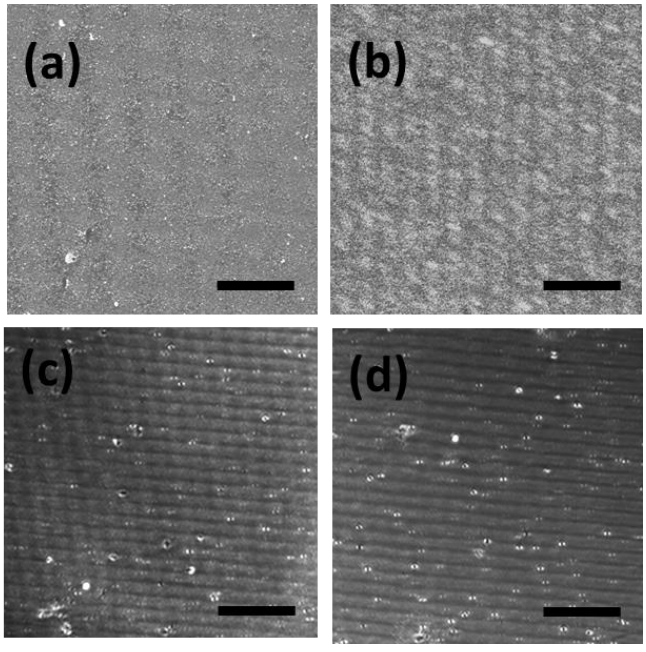

Figure 3S.7:SEM images for 25 nm thick Au surface grating with spacing of (a) 2.4 µm × 1.8 µm and (b) 2.4 µm. Alicona images for (c) 2.4 µm × 1.8 µm and (d) 1.8 µm periodic sample. The scale bars are (a)8µm, (b) 5µm, and (c-d) 12 µm, respectively.

Repeatability

Additional experiments were performed to show the repeatability of this fabrication technique. Figure 3S.9 below shows the gratings made with similar machining parameters on different samples which results in having identical structures. Several Au samples with thickness of 19 nm were ablated by a 150 mJ laser pulse, resulting in a 1.19 μm grating spacing each time (Figure 3S.9a-b). The same exercise was also repeated with samples of 25nm thickness, resulting in a grating of 1.37μm each time (Figure 3S.9-d).

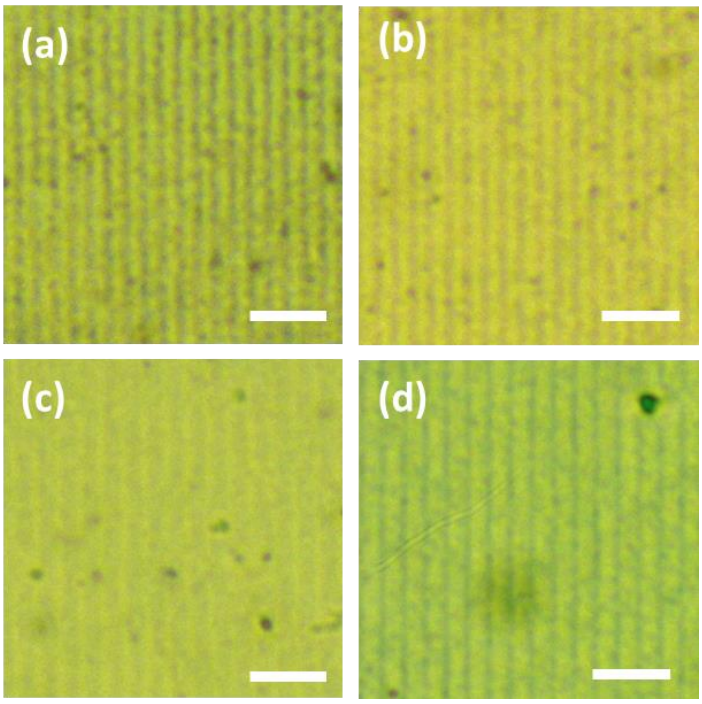

Figure 3S.8:Microscopy images of (a-b) 19 nm Au surface gratings fabricated by holographic DLIP with energy of 150 mJ. (c-d) 25 nm Au surface grating with energy of 330 mJ with spacing of 1.37 μm. (scale bar =5 μm)

We used the following parameter for producing the 1D gratings: 19 nm thickness, 150 mJ laser energy, 21 cm laser beam-sample distance (h), $\Theta=25^{o}$ angle, 0.79 cm mirror-sample distance (d) and 1Hz frequency (f) to achieve periodicity of Λ =1.19 μm. We made the two samples in figure 3S.9(a-b) on different days and we get the same periodicity. Similarly, figure 3S.9(c-d)

are made with: h = 21.5 cm, Θ = 20^o, d=1.8cm, f =1Hz to make grating spacing Λ=1.357μm in both samples.

4S-LASER NANOPATTERNING OF COLOURDED INK THIN FILMS FOR PHOTONIC DEVICES

SEM grating image of (e) black, (f) blue gratings. The light transmission graphs of each ink were integrated for normalization. (scale bar = 10 μm. SEM scale bar=1 μm)

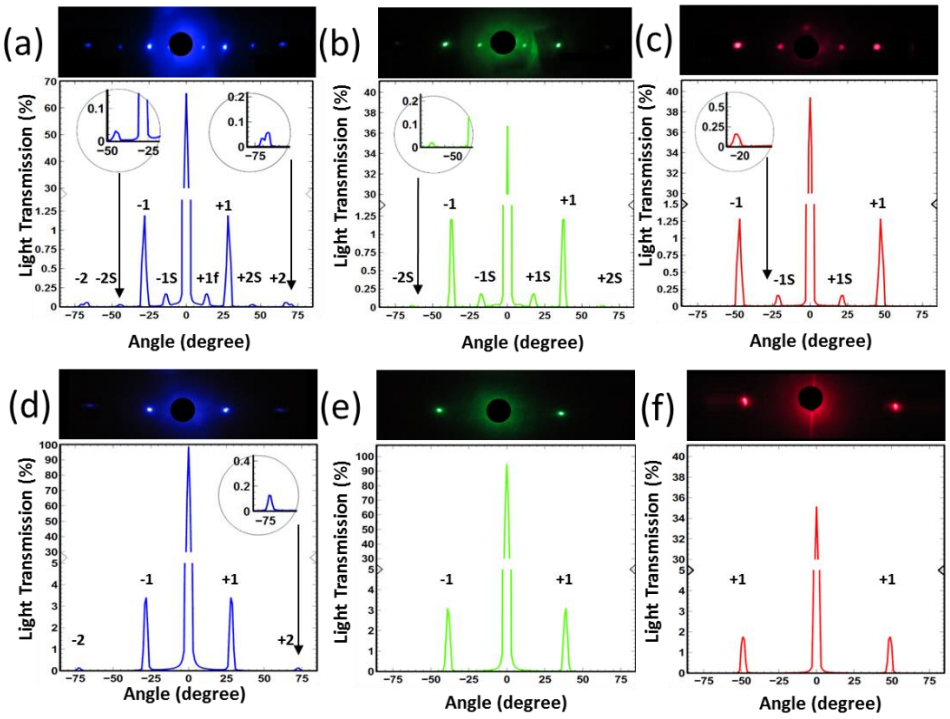

Figure 4S.9:Nanostructure diffraction from three monochromatic lights of (405 nm, 532 nm and 635 nm) on black ink grating (0.84 nm) (a-c) Nd:YAG laser beam wavelength 532 nm (d-f) Nd:YAG laser beam wavelength 1064 nm.

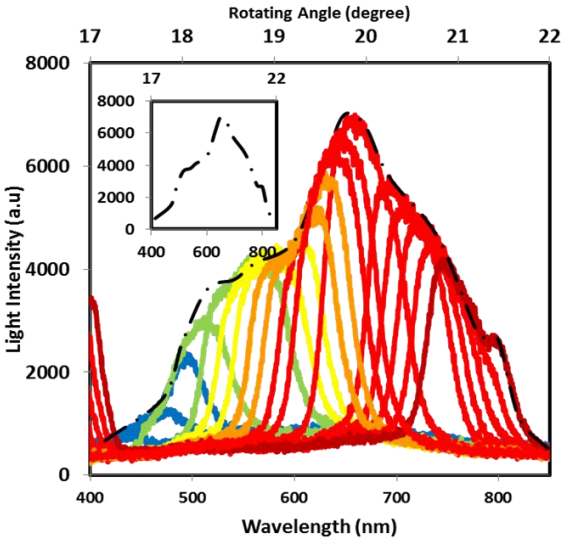

Figure 4S.10:Angle-resolved measurements of the diffraction gratings fabricated *via* holographic DLIP for the first order of the black dye-based inks.

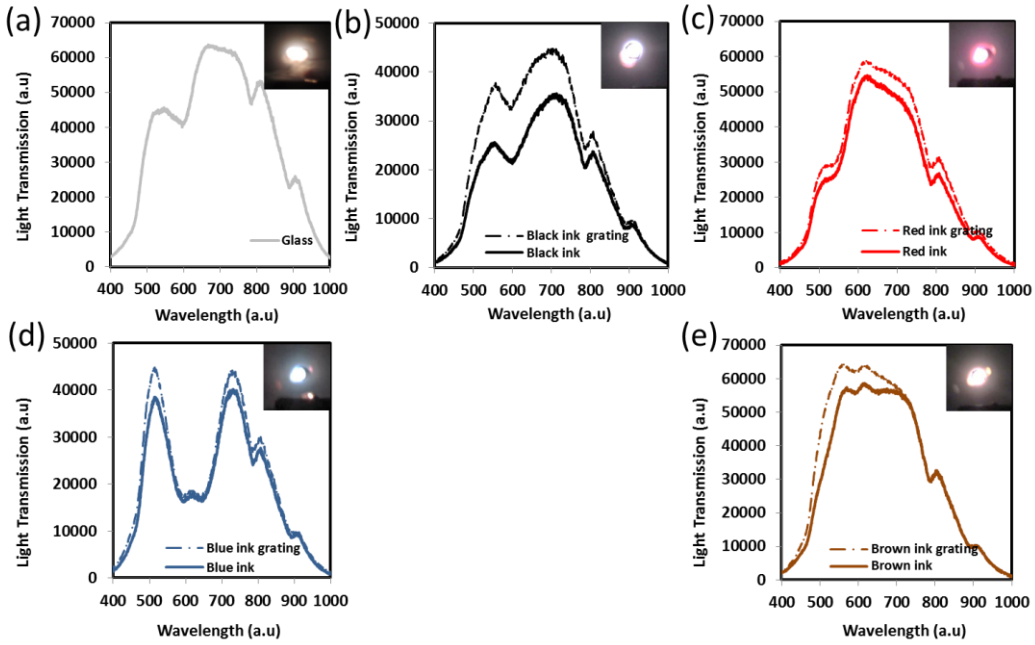

Figure 4S.11:Transmission through 0-order (a) glass, (b) black ink, (c) red ink, (d) blue ink and (e) brown dye-based inks.

5S-DIRECT LASER WRITING OF NANOPHOTONIC STRUCTURES ON CONTACT LNESES

Preparation of the lenses. The black ink was spincoated on 1 mm thick glasses at a speed of (200-1200 rpm). The transmission decreased with lower spincoating speed and higher layer thickness (Figure a). The diffraction intensity of first order increased with increasing thickness of the ink layer (Figure b). Similarly, we compared the transmission of black dye with its thickness on contact lenses to find an optimum thickness of near 915 nm (or 900 nm).

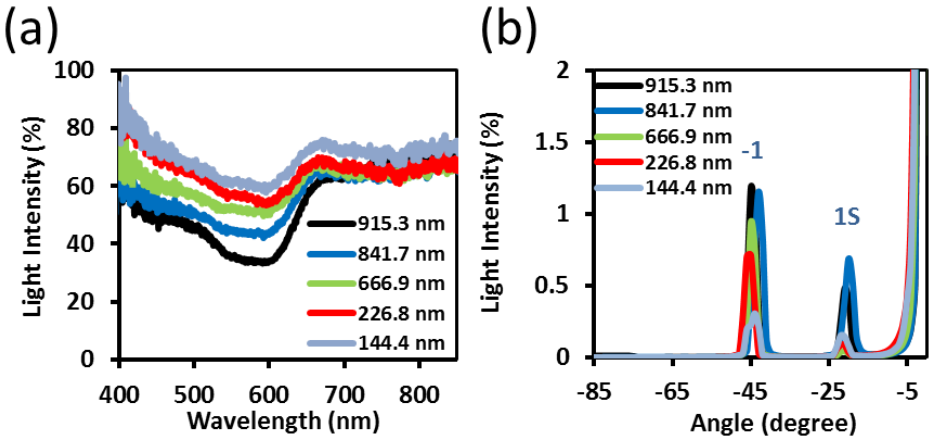

Figure 5S.12: Black ink gratings at different thicknesses in (a) transmission, (b) diffraction modes.

The 915 nm thickness was chosen as the best medium thickness for the subsequent experiments. Using laser interference in Denisyuk reflection mode, the material thickness must be reasonable to allow the laser waves to pass through any substrate to produce the ablative reflection waves. If the material does not transmit the laser waves, the medium would burn it or not respond. In addition, if the absorption reaches zero or 100% transmission, the target material would not interact with laser wave.

Table S5.1: Properties of the contact lenses.

Name	1-DAY ACUVUE TruEye
Material	narafilcon A
Manufacturer	Johnson & Johnson
Water content (%)	46%
FDA group	V
Centre thickness (mm)	0.075
Oxygen permeability ($x10^{-11}$)	100
Principal monomers	MPMDSM, DMA, HEMA, siloxane macromer, TEGDMA, PVP

Table S5.2:Dissolved NaCl in DI water at different concentrations and ellipsometry equivalent reading of refractive index values.

NaCl (g)	NaCl (mmol L^{-1})	Ellipsometry readout	Refractive index, n_o	Diffraction
0	0	1	1.33	45^o
0.2	230	2	1.34	47.3^o
0.4	460	3	1.34	47.3^o
0.6	690	4.5	1.34	47.5^o
0.8	920	5.0	1.34	48.1^o
1.0	1149	6.5	1.34	49.1^o
1.2	1379	7.5	1.35	51.6^o

6S- CURVE PHOTONIC STRUCTURES FOR SENSENIG

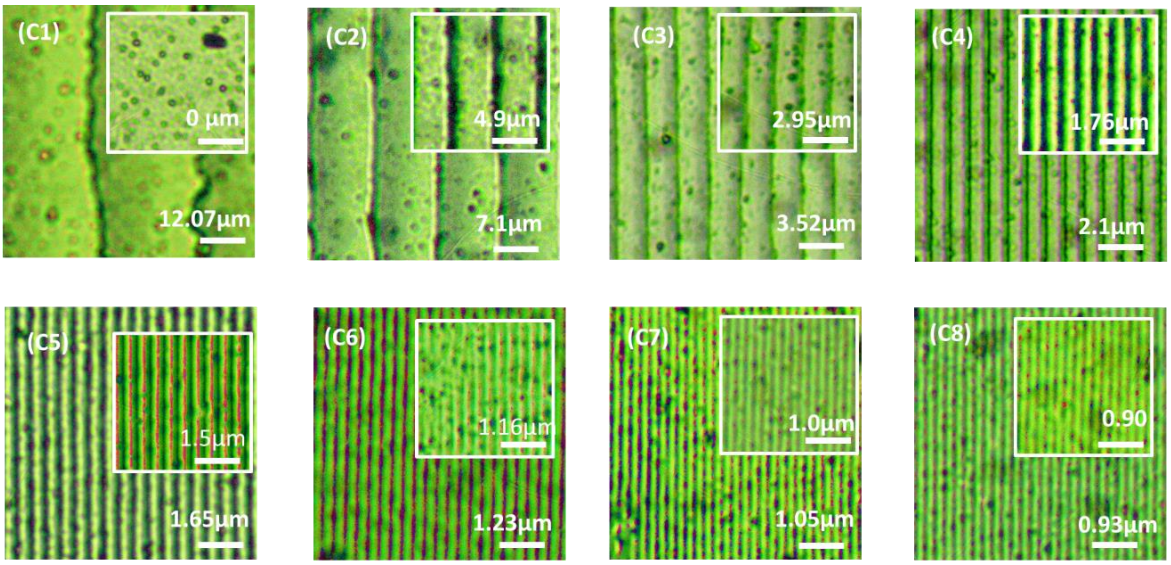

Figure 6S.13: Optical microscopy images showed surface grating nanostructures fabricated by holographic DLIP reflection from the centre of concave mirror. The of changing the laser amplitude due reflection and samples tilted angle on structures spacing (c1) 0^0 , (c2) 5^0, (c3) 10^0 ,(c4) 15^0 , (c5) 20^0, (c6) 25^0 , (c7) 30^0, (c8) 35^0 . (scale bar = 5 µm)

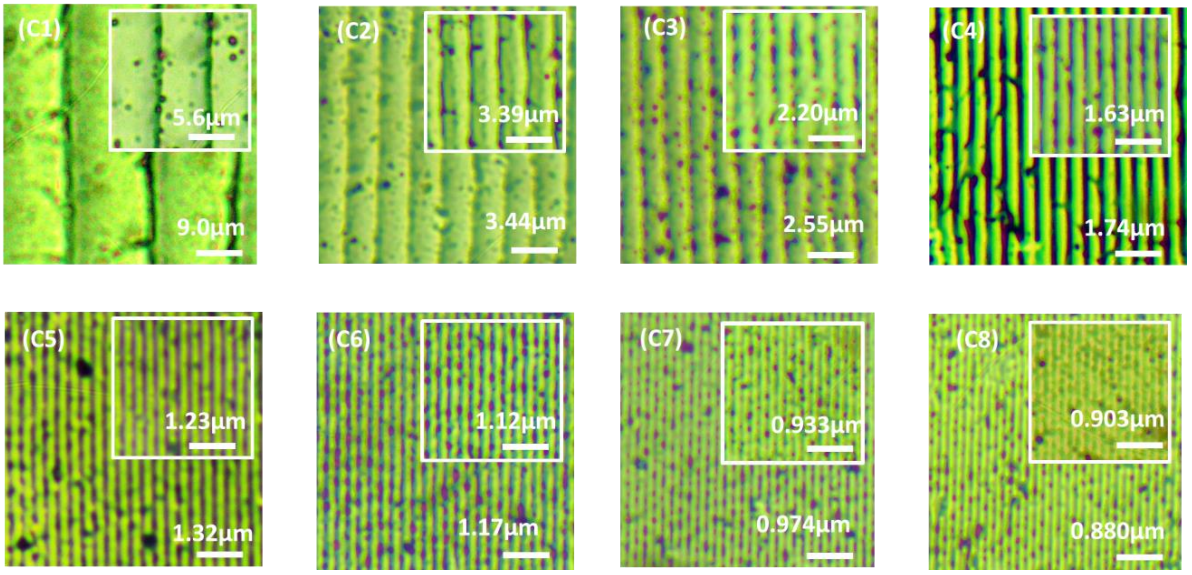

Figure 6S.14: Optical microscopy images showed surface grating nanostructures fabricated by holographic DLIP reflection from the side of concave mirror. The of changing the laser amplitude due reflection and samples tilted angle on structures spacing (s1) 0^0 , (s2) 5^0, (s3) 10^0 ,(s4) 15^0 , (s5) 20^0, (s6) 25^0 , (s7) 30^0, (s8) 35^0 . (scale bar = 5 µm)

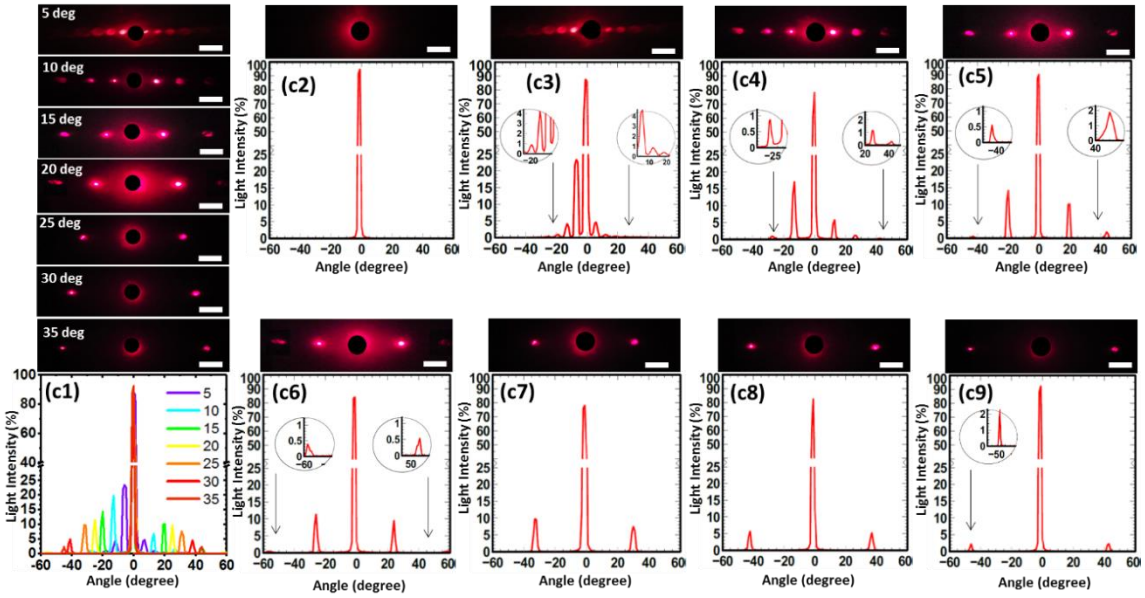

Figure 6S.15: Experimental diffraction at central pulse on concave mirror with samples tilted angle of (c1) $5^0 - 35^0$ (c2) Fresnel lens at 0^0, (c3) 5^0, (c4) 10^0 ,(c5) 15^0 , (c6) 20^0, (c7) 25^0 , (c8) 30^0, (c9) 35^0 .(scale bar=5 cm)

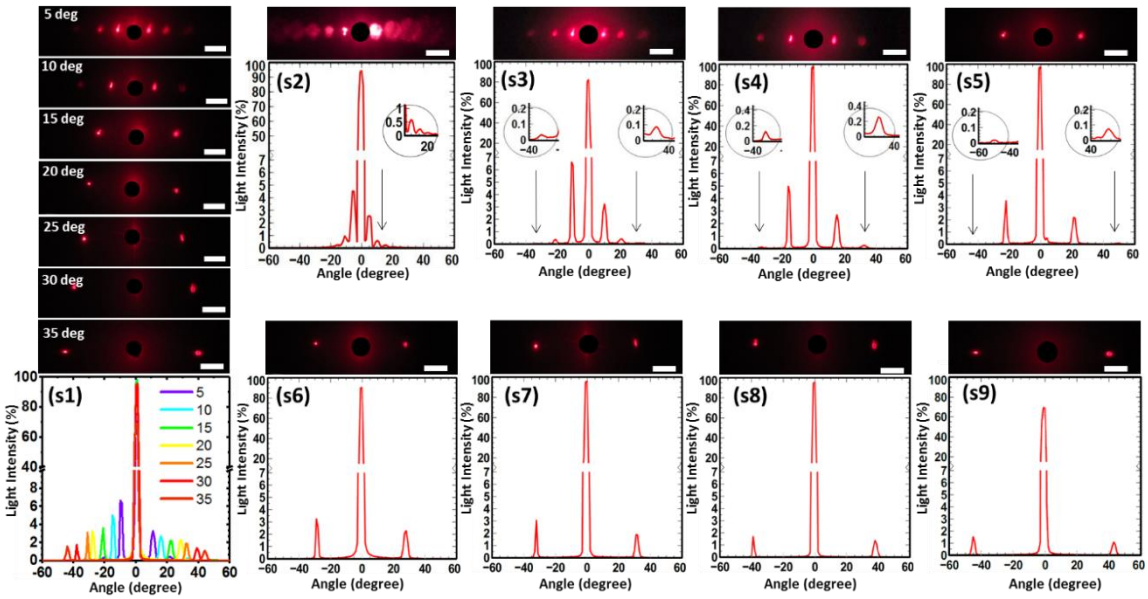

Figure 6S.16: Experimental diffraction off side pulse on concave mirror with samples tilted angle of (s1), $5^0 - 35^0$ (s2) Grating displacement lens at 0^0, (s3) 5^0, (s4) 10^0 ,(s5) 15^0 , (6s) 20^0, (s7) 25^0 , (s8) 30^0, (s9) 35^0 .(scale bar=5 cm)

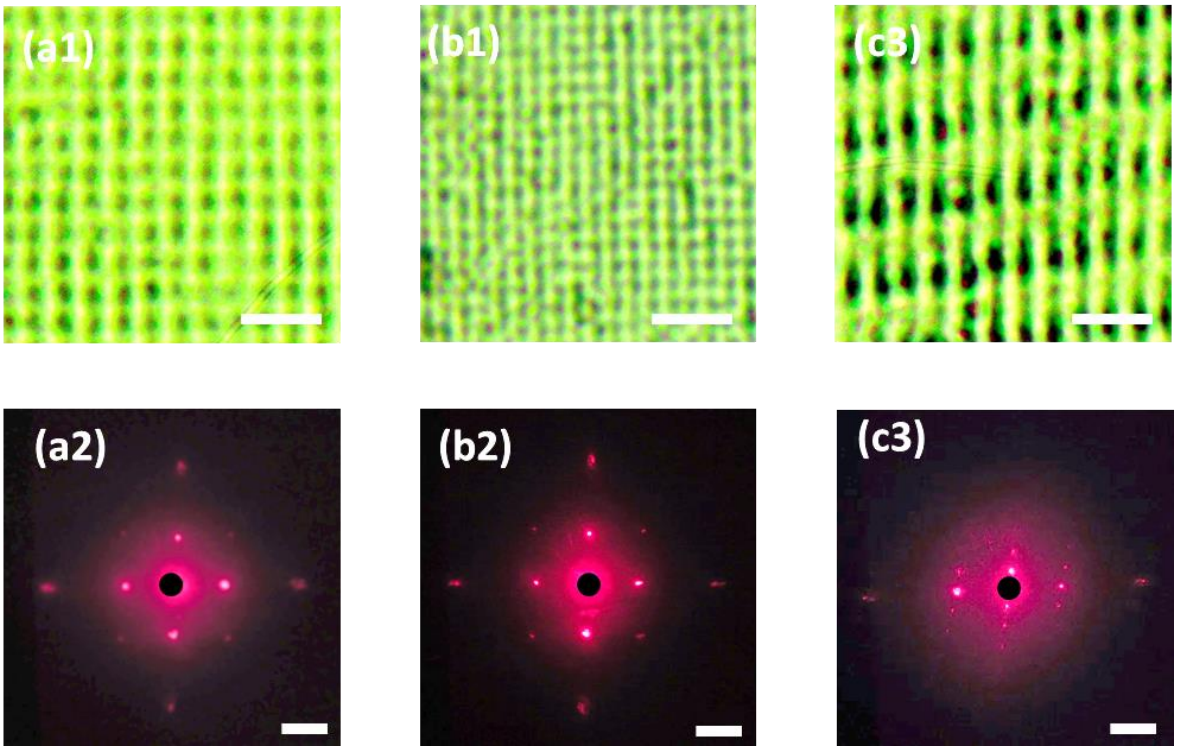

Figure 6S.17: 2D patterning structures produced by holographic DLIP reflection on the side of concave mirror and they are generated by three pulses. Optical microscopy images of 2D nanostructures with different geometries and the 635nm illumination diffraction (a1) 1.7 μm × 1.7 μm, , (1b) 1.2μm × 1.2 μm, , (c1) 1.84μm × 4.5 μm.(a2-c2) Diffraction of monochromatic light (635 nm) *via* 2D patterned arrays. (scale bar = 5 μm)